University of Alberta

Investigation of the Double-Trap Intrinsic Kinetic Equation for the Oxygen Reduction Reaction and its implementation into a Membrane Electrode Assembly model.

by

Michael Moore

A thesis submitted to the Faculty of Graduate Studies and Research
in partial fulfillment of the requirements for the degree of

Master of Science

Department of Mechanical Engineering

Fall 2012
Edmonton, Alberta

To my good friend Killian, sorely missed.

Abstract

A significant contributor to performance loss in polymer electrolyte fuel cells is the oxygen reduction reaction (ORR). A major challenge facing researchers is the development of a kinetic model that accurately accounts for ORR kinetics. Wang et al. proposed a kinetic model that assumes the ORR is comprised of four intermediate steps and two intermediate species. The model can predict the commonly observed doubling of the Tafel slope. The model had several limitations such as underpredicting Tafel slopes at low overpotentials. In this work, the model is extended to better account for oxygen depletion and the backward reactions. Parameter estimation is used to determine new kinetic parameters. The new kinetic model and parameters provide a good match to the experimental data used to obtain the kinetic parameters. Implementation of this model into a high-fidelity MEA model matches experimental data over numerous operating conditions and catalyst layer compositions.

Acknowledgements

I would like to first acknowledge my supervisor, Marc Secanell. He convinced me to come to the University of Alberta and that the internal combustion engine was not worth further research. He also provided a very interesting topic of research, great support, constant guidance and the occasional jug of beer.

I would also like to thank the financial assistance from our industry sponsors, the Automotive Fuel Cell Cooperation, and in particular Andreas Putz for giving us guidance and direction during this Masters. I would also like to thank them for their hospitality during our visits there and for sharing their ideas and knowledge.

I also thank my colleges in the Energy Systems Design Lab, for their help during this Masters, whether it was their ideas, knowledge or just idle chat about research and life in general during the more difficult times. I'd like to further thank all the friends I made in Edmonton, they made the to move from Ireland to Canada very easy and not a small amount of fun.

Finally, I'd like to thank my family who have given me constant support during my travels. In particular, I like to thank my parents for helping me get to this point, with all the help and advice that I could ever need.

Contents

List of Tables

List of Figures

Nomenclature

A_v	Platinum surface area utilized for the ORR per unit volume of CL ($cm^2 cm^{-3}$)
a_w	Water activity in ionomer
b	Tafel slope (mV/dec)
c^{ref}	Reference reactant concentration ($mol\, cm^{-3}$)
C_O	Oxidant concentration ($mol\, cm^{-3}$)
C_R	Reductant concentration ($mol\, cm^{-3}$)
c_g	Total gas concentration ($mol\, cm^{-3}$)
c_i	Concentration of species i ($mol\, cm^{-3}$)
$D_{i,j}^{eff}$	Effective diffusivity coefficient of species i in species j ($cm^2\ s^{-1}$)
$D_{i,j}$	Bulk diffusivity coefficient of species i in species j ($cm^2\ s^{-1}$)
E	Applied cell potential (V)
E^0	Theoretical cell voltage (V)
E_{eq}	Equilibrium cell voltage (V)
F	Faraday constant ($96,485\ \ C\, mol^{-1}$)
$H_{O_2,N}$	Henry's constant for O_2 in Nafion ($Pa\, cm^3\, mol^{-1}$)
i	Current produced during a reaction ($A\, cm^{-2}$)
i	Local volumetric current in the agglomerate ($A\, cm^{-3}$)

j^*	Reference prefactor
k	Rate constant
k^0	Rate constant at zero overpotential
m_{Pt}	Platinum areal loading per unit area in the catalyst layer ($mg\,cm^{-2}$)
n	Number electrons transferred during a reaction
N_i	Flux of species i
n_{drag}	Electro-osmotic drag coefficient
O_{ads}	O absorbed intermediate species
OH_{ads}	OH absorbed intermediate species
p	Cell pressure (atm)
$Pt\vert C$	Mass percentage of Platinum on the support Carbon black
R	Gas constant ($8.315\ \ J\,K^{-1}\,mol^{-1}$)
S_i	Source term for species i
T	Cell temperature (K)
V_{Pt}	Platinum volumetric loading per unit area in the catalyst layer ($mg\,cm^{-3}$)
x_i	Mole fraction of species i
z_i	Valency of species i ($C\,mol^{-1}$)

Greek Letters

α_c	Cathodic reaction transfer coefficient
β	Symmetry factor
ΔG_a^0	Free energy barrier of anodic reaction at zero overpotential (eV)
ΔG_c^0	Free energy barrier of cathodic reaction at zero overpotential (eV)
ΔG_a	Free energy barrier of anodic reaction (eV)
ΔG_c	Free energy barrier of cathodic reaction (eV)
η	Overpotential (V)
γ	Reactant reaction order
λ	Membrane water content
ν	Reaction rate (s^{-1})
ϕ_m	Electrolyte (membrane) phase potential (V)
ϕ_s	Solid phase (Electric) potential (V)
σ_i	Bulk conductivity of charged species i ($S\ cm^{-2}$)
σ_i^{eff}	Effective conductivity of charged species i ($S\ cm^{-2}$)
θ_i	Coverage of intermediate species i
ε_N	Volume fraction of ionomer in a layer
ε_S	Solid phase volume fraction in a layer
ε_V	Porosity or void volume fraction in a layer

Abbreviations

BPP	Bi-polar plate
CCL	Cathode Catalyst Layer
CCM	Catalyst coated membrane
CL	Catalyst Layer
CV	Cyclic voltammetry
DA	Dissociative adsorption reaction
DFT	Density functional theory
FCST	Fuel Cell Simulation Toolbox
GDL	Gas Diffusion Layer
hcd	High current density
HOR	Hydrogen Oxidation Reaction
lcd	Low current density
MEA	Membrane Electrode Assembly
MPL	MicroPorous Layer
ORR	Oxygen Reduction Reaction
PEM	Polymer Electrolyte Membrane
PFSI	Perfluorosulfonated Ionomer
RA	Reductive adsorption reaction
RD	Reductive desorption reaction
RDE	Rotating disk electrode
RDS	Rate determining step

RHE	Reference hydrogen electrode
RT	Reductive transition reaction

Chapter 1

Introduction

1.1 Background and Motivation

Polymer electrolyte membrane (PEM) fuel cells are a promising technology that is hoped will one day replace the internal combustion (IC) engine as the primary power system used in automobiles [1]. PEM fuel cells offer numerous advantages over the current incumbent power system, such as its environmentally friendly operation and the potential for a limitless supply fuel that is not dependent on a small number of countries, as is the case for fossil fuels. PEM fuel cells also offer a number of advantages over its chief rival in the race to replace the IC engine, the battery powered vehicle. These include longer driving ranges, faster start up times at cold temperatures and shorter 'recharging times'. Other prominent uses for fuel cells include stationary applications, where large scale fuel cells can provide back up power. Forklift trucks are increasingly switching from battery power to fuel cells, due to their fast 'recharging' ability. Fuel cells are also used to provide small scale portable power to devices such as laptop computers and phone chargers. To realize more widespread use, however, the PEM fuel cell must overcome a number of obstacles, chief among which is the high cost of production, currently making it uncompetitive, particularly in comparison to the IC engine. A major contributor to this cost is the platinum catalyst which is used to drive the reactions in the cell. Reducing the amount of platinum being used in the fuel cells is currently one of the main areas of research in PEM fuel cell development.

A key component of research in fuel cell development is numerical modeling. Numerical modeling allows researchers to couple several complex mathematical models that describe the interconnected processes occurring within a fuel cell. These models can be used to predict fuel cell performance under different operating conditions. They also allow for the optimization of the design of the system and can be used to investigate the fundamental phenomena taking place in the cell. Numerical modeling is particularly important in this field due to the difficulty in performing experimental research. Experimental research is limited by the inherit high cost in the manufacture of the cells and the time-consuming nature of the experiments, preventing 'playful' or unconstrained experimentation that can often lead to innovative designs or a deeper understanding of the working of the cell [2].

The spatial dimensions of the fuel cell is another important factor when performing experiments. The length-scales of each of the layers comprising a cell is typically on the order of tens of microns while the agglomerates that the catalyst layers are composed of are in the order of 100 nanometers. Such small length scales, along with other complexities such as the transient nature of the processes and the complex coupling between the individual processes, makes *in situ* measurements extremely difficult [3]. This leads to much uncertainty in determining the governing equations that fully describe the operation of a fuel cell. This is especially true for the cathode catalyst layer of the fuel cell where losses associated with the electrochemical reactions significantly lower the performance of a fuel cell.

In the cathode of a fuel cell, the electrochemical reaction that is occurring is the oxygen reduction reaction (ORR), where oxygen reacts in the presence of the platinum catalyst with hydrogen ions and electrons to form water, which is exhausted from the cell. This process is a complex, multi-step reaction, involving the formation of a number of intermediates. However, the process is often modeled using the Butler-Volmer equation, or a simplification of the equation called the Tafel equation, which was derived to account for simple, single step reactions. A number of simplifying assumptions need to be made in order to apply this simple model to a complex reaction such as the ORR and experimental data shows that the Butler-Volmer model cannot correctly capture the kinetic losses occurring in the ORR. Recently Wang et al. [4] developed a new kinetic model that assumes the ORR is comprised of four elementary intermediate steps and accounts for the production of two adsorbed intermediate species. The model is based on a number of kinetic parameters, in particular the free energies of activation of each of the steps and the free energy of adsorption of the intermediate species. This model has been shown to capture the trends seen in the experimental data more accurately than the Butler-Volmer equation and also provides a greater understanding of the ORR, in particular the effect of the intermediate species on the production of current in the cathode catalyst layer (CCL). However, assumptions in the derivation of the model by Wang et al. result in the effect of the local oxygen concentration not being correctly accounted for.

The aim of this thesis is to investigate the effect of using this new kinetic model in place of the standard kinetic model, the Tafel equation. The first goal is to modify the new kinetic model so that the local oxygen concentration at the reaction site is correctly accounted for. This model will be analyzed 'in isolation', i.e. the characteristics of kinetic model itself will be investigated without considering other physical phenomena present in a fuel cell. Key kinetic parameters upon which the model is based on will have to be found using parameter estimation strategies, as the values for these parameters that were provided in the original work by Wang et al. will no longer be valid due to the change in the model derivation. Further, the original model was found to capture the general trends observed in experimental data, however the performance was found to be consistently over-predicted. The novel kinetic model will be added to a full membrane electrode assembly (MEA) model that accounts for mass transport, charged particle transport and the uptake of water in the membrane. This full MEA model will be analyzed using parametric studies and results will be compared with those found using the Tafel equation and with experimental data.

1.2 Fuel Cell Background

1.2.1 Fuel Cell Structure

In this work, the fuel cell under consideration is the polymer electrolyte membrane (PEM) fuel cell. A fuel cell converts the chemical energy contained in the fuel into electrical energy, in a similar manner to that of a battery. This is achieved using electrochemical reactions, in contrast to the internal combustion engine where the combustion process produces heat rather than electrical energy. This results in a fuel cell not being limited to the Carnot cycle, and therefore a maximum energy efficiency. The PEM fuel cell uses hydrogen and oxygen as the fuel and exhausts water according to the following reaction:

$$1/2O_2 + H_2 \rightleftharpoons H_2O \tag{1.1}$$

In order to extract energy from this process, the reaction is split into two half cell electrochemical reactions. The first reaction occurs in the anode of the cell. In electrochemical terms, the anode is the half cell in which an oxidation reaction is occurring. During oxidation, electrons are produced from the reactant which flow out of the electrode. In a PEM fuel cell, the fuel being reacted is hydrogen, which will split into a pair of hydrogen ions (or protons) and a pair of electrons, i.e.:

$$H_2 \rightleftharpoons 2H^+ + 2e^- \tag{1.2}$$

Equation 1.2 is termed the hydrogen oxidation reaction (HOR).

The second half cell reaction occurs at the cathode electrode of the cell. The reaction in the cathode is the reduction reaction, in which electrons are consumed, resulting in a flow of electrons into the half cell. The fuel being reacted is oxygen, which combines with the incoming electrons and hydrogen ions from the anode reaction to form water i.e.:

$$1/2O_2 + 2H^+ + 2e^- \rightleftharpoons H_2O \tag{1.3}$$

Equation (1.3) is termed the oxygen reduction reaction (ORR). Note that the addition of equations 1.2 and 1.3 will produce the overall equation 1.1.

In order for the reactions to proceed, the cell must ensure that:

1. the reactants reach the reaction sites on both the anode and cathode side.
2. protons must be able to travel from the anode side to the cathode side and reach the reaction sites.
3. electrons must be able to travel from the anode side to the cathode side and reach the reaction sites.
4. the product (water) must be removed from the reaction sites so as not to impede mass transport of the reactants.

These requirements lead to the notion of the triple phase boundary, upon which the reaction occurs, where a particle of the platinum catalyst is in contact with: a) an open pore, which allows for the transport of the reactant to the site, b) the ionic conductor, which allows for the transport of protons and c) the solid phase, upon which the catalyst is mounted which allows for the transport of electrons. Hence, there should be three distinct phases required to ensure that the reactions can proceed. However, this would require that the 2nm particle of platinum be

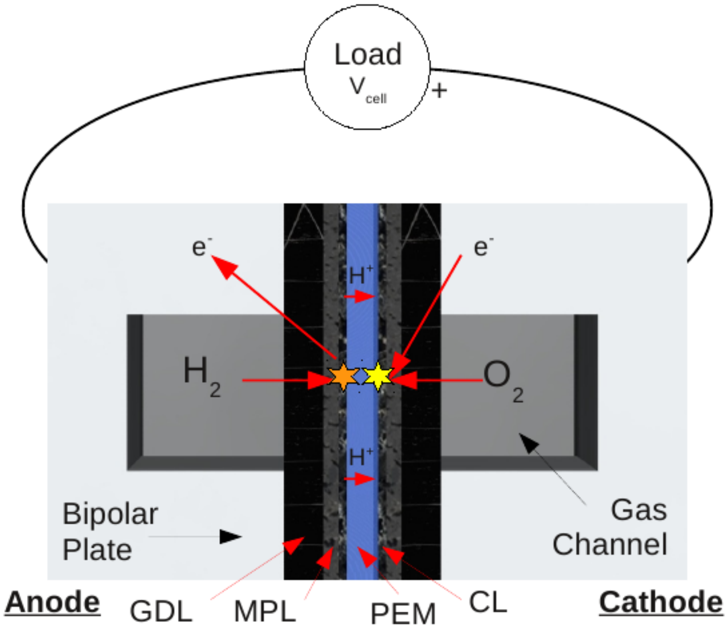

Figure 1.1: Layer structure of the PEM fuel cell.

mounted on the surface of a carbon particle and be in contact with the ionomer phase and void phase. As this would be unlikely, it is assumed at the ionomer completely covers the platinum particle, forcing the oxygen to dissolve into it and then diffuse towards to the reaction site.

The basic structure of a PEM fuel cell is shown in Figure 1.1. The cell is typically composed of individual layers, each playing an important role in the performance of the cell. The catalyst particles are located in the catalyst layer (CL) so this is where the reactions occur. The catalyst layer is typically fabricated by preparing an ink that contains catalyst particles supported on carbon particles, an ionic conductor, typically Nafion which is a perfluorosulfonated ionomer (PFSI) produced by DuPont, and a solvent. Through imaging of catalyst layers, it has been found that the carbon particles will aggregate together to form agglomerates that are wrapped in a film of Nafion. This agglomerate structure allows for the transport of electrons through the carbon support, the transport of protons through the Nafion, and transport of the reactants through the pores between the agglomerates and then, through the Nafion to the reaction site.

In a PEM fuel cell, the two half cell reactions are separated from one another using a polymer electrolyte membrane (hence the name polymer electrolyte membrane fuel cell, though it is sometimes termed the proton exchange membrane fuel cell). The membrane is impermeable to the reactants and to electrons, but allows for the transport of protons. When placed between the anode and cathode catalyst layers, it prevents the oxygen and hydrogen from crossing from one side to the other. It also allows protons from the anode reactions to travel to the cathode to complete the overall reaction. As electrons cannot pass through the membrane they must travel through an external circuit to the cathode side, where they can complete the reaction. This circuit contains a load that uses the energy produced in the fuel cell.

The micro-porous layer (MPL) is composed of a porous material that is electronically conductive. Its primary function is to aid the removal of water from the catalyst layers, therefore it is made so that the pores are hydrophobic. The final layer is the gas diffusion layer (GDL, sometimes called diffusion media), which is constructed from a carbon fiber cloth. Its primary function is to help the even diffusion of the reactants in the in-plane direction, so that the reaction sites directly opposite the current collector are not starved.

These layers, which are present on the anode and cathode side of the cell, on either side of the membrane, together form the membrane electrode assembly (MEA). The final component of the fuel cell is the bi-polar plate. The MEA is pressed between two bi-polar plates (BPP), forming the completed cell. Channels etched in the sides of the plate carry the reactants to each of the individual cells. The part of the plate actually in the contact with the MEA is typically referred to as the land or current collector. Electrons are transported from the anode, through the MPL and GDL to the conductive BPP through the load on the external circuit and back to the BPP on the cathode side where they can reach the cathode catalyst layer.

In this work, the layer of particular interest is the cathode catalyst layer (CCL). The catalyst layers are where the reactions are occurring, and the reaction in the cathode, the ORR, is not yet fully understood. It is also a major source of losses in the fuel cell, especially in comparison to the kinetic losses incurred in the anode. The HOR overpotential losses are typically of the order of 50mV, while the cathode losses are 500-600mV [5]. Due to these large losses, the ORR in CCL is therefore the subject of considerable research. A background on the theory used to analyze the reaction is presented in the next section.

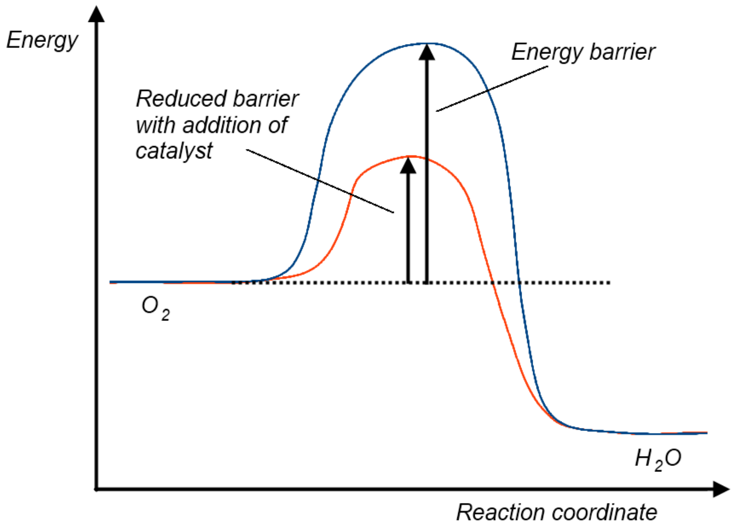

Figure 1.2: Figure showing the change in Gibbs free energy with reaction coordinate.

1.2.2 Electrochemical Reactions

The previous section introduced the two half-cell reactions that are occurring in the anode and cathode of the PEM fuel cell. In order for any electrochemical reaction at an electrode to proceed an energy barrier must be overcome, called the activation energy, as is shown in Figure 1.2. This activation energy determines how 'fast' the reaction proceeds, as shown by the Arrhenius equation:

$$k = Ae^{-E_a/RT} \tag{1.4}$$

The rate constant k is a measure of the speed of the reaction. It is based on a pre-exponential factor, A, that accounts for the quantity of the reactant available to participate, their lifetime and the probability of the reactant decaying to the product. The exponential term accounts for the probability of finding a species in the activated state (i.e. at the peak of the barrier shown in Figure 1.2) [6].

The height of the barrier will depend on the reaction, a large activation energy means that the reaction is slow. A reaction is complex if it requires a number of intermediate reactions, with intermediate species being formed. For example, the HOR may be comprised of the following steps [6]. First, the hydrogen molecule may attach to the surface of the electrode (it has been chemisorbed to the surface). The next reaction involves the absorbed hydrogen molecule splitting into two individual hydrogen ions attached to the surface, followed by the desorption of the attached ion from the surface with the electrons staying in the electrode. This process can be written as [6]:

$$\text{step 1:} \qquad H_2 + M \rightarrow M \cdot H_2 \tag{1.5}$$
$$\text{step 2:} \qquad M \cdot H_2 + M \rightarrow 2(M \cdot H) \tag{1.6}$$
$$\text{step 3:} \qquad M \cdot H \rightarrow (M + e^-) + H^+ \tag{1.7}$$

where M represents a metal electrode surface. Each of these intermediate reactions will have their own energy barriers to be overcome, each contributing to performance losses in the fuel cell. There are two intermediate species formed, $M \cdot H_2$ and $M \cdot H$, with three intermediate steps. The intermediate species will cover a part of the metal surface and prevent the reactant from reacting in that area. If one of the steps is slower than the others, for example equation (1.6), then more and more of the metal surface will be covered by the $M \cdot H_2$ species, as the overall reaction is forced to wait for the second step to fire and clean it off. Therefore, the 'coverage' of that species is very high compared to the other intermediate species and could impede other reactions. The coverage is defined as the number of adsorption sites on the platinum surface covered by the intermediate species, divided by the total number of absorption sites on the clean surface. The slow reaction is termed the rate determining step (RDS), as the overall reaction rate will be limited by the rate of its slowest intermediate reaction and the kinetic characteristics of the overall reaction will be determined by the characteristics of the RDS.

The activation energy E_a in equation (1.4) is the standard internal energy of activation which is normally expressed in terms of the Gibbs free energy. This is done by noting that the internal energy of a system is equal to the standard energy of enthalpy of activation plus a mechanical work term:

$$\Delta E = \Delta H - \Delta(PV) \tag{1.8}$$

where the work term is taken to be zero in a condensed phase reaction. This leads to $\Delta E = \Delta H$. The standard enthalpy of activation can be expressed in terms of the standard Gibbs free energy of activation and the standard entropy of activation:

$$\Delta H = \Delta G + T\Delta S \tag{1.9}$$

Substitution of equation (1.9) into equation (1.8) and then into equation (1.4) will lead to:

$$k = A' e^{-\Delta G/RT} \tag{1.10}$$

where the A' contains the contribution from the entropy term $e^{-\Delta S/R}$ which is a dimensionless constant, i.e.:

$$A' = Ae^{-\Delta S/R} \tag{1.11}$$

The Gibbs free energy is used as it can be expressed in terms of the potential applied to the fuel cell.

Applying a potential difference across the solid electrode/electrolyte interface will affect the energy barrier. If the potential is made more negative than the standard Nernst potential, the reduction reaction is favored leading to a net cathodic reaction. A more positive potential leads to favoring the oxidation reaction and results in a net anodic current. If the potential is more negative than the standard Nernst potential by an amount ΔE, then the energy of the electron being consumed is changed by $-F\Delta E$ or $-F(E - E^0)$, where F is Faraday's constant and E^0 is the standard Nernst potential. The standard Nernst potential is the potential at which no net reaction will occur at standard temperature and pressure, i.e. the reaction is at equilibrium. The energy barriers will be be modified by a fraction of this energy, which is termed the symmetry factor β. This factor will depend on the shape of the free energy barriers and may also be a function of the potential applied. Note that this fraction is also sometimes called the transfer coefficient (denoted α), which is the apparent symmetry factor of a multi-step reaction based on the assumption of a rate determining step [7].

A general reduction reaction can be written as $O + e^- \rightleftharpoons R$, where O denotes the oxidant being reduced and R is the product. This reaction can be favored by applying a potential that is lower than its standard Nernst potential. The resulting change in its activation energy barrier will be given by:

$$\Delta G_c = \Delta G_c^0 + \beta F(E - E^0) \tag{1.12}$$

where ΔG_c is the free energy barrier of the reduction reaction and ΔG_c^0 is the free energy at the standard Nernst potential. Note that because the applied voltage E is less than the standard Nernst potential E^0, the energy barrier will be lowered. Similarly the change in the oxidation energy barrier is given by:

$$\Delta G_a = \Delta G_a^0 - (1 - \beta)F(E - E^0) \tag{1.13}$$

Returning to equation (1.10), and substituting in equations (1.12) and (1.13), the potential dependent rate constants can be written as:

$$k_f = A_f' e^{-\Delta G_c^0/RT} e^{-\beta F(E-E^0)/RT} \tag{1.14}$$

where subscript f denotes the forward reaction. Similarly, the backward rate will be written as:

$$k_b = A_b' e^{-\Delta G_a^0/RT} e^{(1-\beta)F(E-E^0)/RT} \tag{1.15}$$

The rate of the reaction can then be defined in terms of the rate constant and the surface concentration of the reactants. The reaction rate per unit area of the electrode surface in the forward and backward directions are given by:

$$\nu_f = k_f C_O \tag{1.16}$$

$$\nu_b = k_b C_R \tag{1.17}$$

where C_O and C_R are the concentrations of the oxidant and reductant at the surface of the electrode. The net rate will be given by:

$$\nu_{net} = \nu_f - \nu_b = k_f C_O - k_b C_R = \frac{i}{nFA} \tag{1.18}$$

where i is the current produced in the reaction, n is the number of the electrons transferred (one in this case) and A is the surface area of the electrode. Substituting equations (1.14) and (1.15) into equation (1.18) will yield:

$$\nu_{net} = A_f' e^{-\Delta G_c^0/RT} e^{-\beta F(E-E^0)/RT} C_O - A_b' e^{-\Delta G_a^0/RT} e^{(1-\beta)F(E-E^0)/RT} C_R \tag{1.19}$$

For the case where the applied potential E is equal to E^0, there is no *net* reaction and C_O will equal C_R and the surface concentration will be equal to the bulk concentration, far from the surface of the electrode. The bulk concentration is denoted C_O^{ref} and C_R^{ref}.The forward and backward reaction rates will therefore be equal:

$$\nu_f = \nu_b = A_f' e^{-\Delta G_c^0/RT} C_O^{ref} = A_b' e^{-\Delta G_a^0/RT} C_R^{ref} = k^0 \tag{1.20}$$

where k^0 is the standard rate constant, i.e. the rate constant at the standard Nernst potential. This constant characterizes the reaction at the standard Nernst potential, which is used as a reference point. The current produced at potential E in the reaction can therefore be expressed in terms of this rate constant:

$$i = FAk^0 (C_O e^{-\beta F(E-E^0)/RT} - C_R e^{(1-\beta)F(E-E^0)/RT}) \tag{1.21}$$

Note that equation (1.21) defines the current as the departure from standard Nernst potential, where the concentration of the reactants and products are provided at standard temperature and pressure. If the reaction is not occurring at standard temperature and pressure, the Nernst equation gives the potential the system will equilibrate to:

$$E_{eq} = E^0 + \frac{RT}{nF} \ln \frac{C_O}{C_R} \tag{1.22}$$

This is the equilibrium potential E_{eq} (or simply Nernst potential) and as the system is at equilibrium, the current produced is zero, as the forward and backward rates are equal. The cathodic and anodic current produced will therefore be equal and are called the exchange current i_0. The exchange current density is given as:

$$i_0 = FAk^0 C_O^{ref} e^{-\beta F(E_{eq}-E^0)/RT} = FAk^0 C_R^{ref} e^{(1-\beta)F(E_{eq}-E^0)/RT} \tag{1.23}$$

Dividing equation (1.21) by equation (1.23), will lead to the commonly used current over-potential equation, also known as the Butler-Volmer equation:

$$i = i_0 \left(\frac{C_O}{C_0^{ref}} e^{-\beta F(E-E_{eq})/RT} - \frac{C_R}{C_R^{ref}} e^{(1-\beta)F(E-E_{eq})/RT} \right) \tag{1.24}$$

Note that the current is now defined relative to the equilibrium potential E_{eq}. The over-potential, $\eta = (E - E_{eq})$, can be considered the departure of the applied potential from the equilibrium potential. The resulting current produced can be considered as the departure from the exchange current.

For an elementary reaction one electron transfer reaction the Butler-Volmer equation can be used to model the current produced in the reaction. This is typically written as:

$$i = i_0 \left[\frac{C_R(0,t)}{C_R^*} \exp\left(\frac{-\beta F\eta}{RT}\right) - \frac{C_P(0,t)}{C_P^*} \exp\left(\frac{(1-\beta)F\eta}{RT}\right) \right] \tag{1.25}$$

where i_0 is the exchange current density, the current produced at the open circuit potential, $C_R(0,t)$ is the concentration of the reactant at the surface of the electrode, C_R^* is the concentration of the reactant at the surface of the electrode at which the exchange current density was measured (note the same applies to the subscript P which denotes the products in the reaction). The transfer coefficient, β, describes how the forward and backward reaction rates are affected by the change in electrode potential, and η is the over-potential which is the departure from the open circuit potential of the cell.

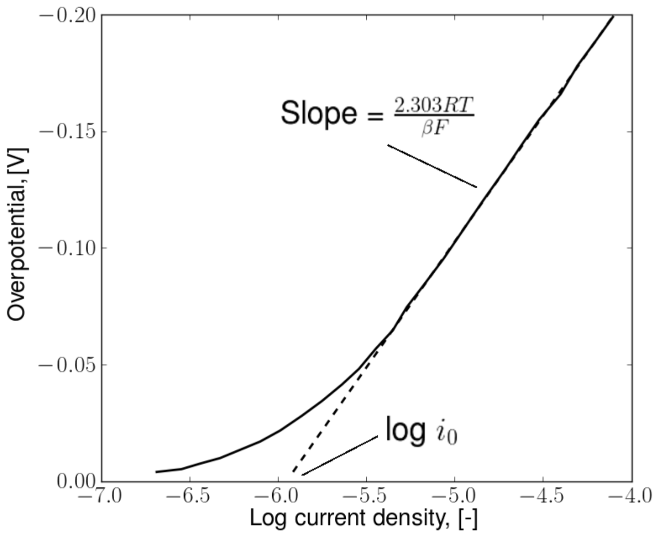

Figure 1.3: Figure plotting the Butler-Volmer equation (solid line) and the Tafel approximation (dashed line).

At very high over-potentials and for no mass transport effects, the second term, which is the contribution of the backward reaction, is negligible and can be dropped to give :

$$i = i_0 \text{exp}\left(\frac{-\beta F\eta}{RT}\right) \tag{1.26}$$

which can be written in the form of the Tafel equation, by extracting the over-potential term:

$$\eta = a + b\ log(i) \tag{1.27}$$

where b is the Tafel slope of the equation and is given by:

$$b = \frac{-2.303RT}{\beta F} \tag{1.28}$$

This is shown graphically in Figure 1.3.

The Butler-Volmer model was derived for elementary electrochemical reactions, with a single electron transfer. If more than one electron is involved in the reaction, as is the case for the ORR, then the Butler-Volmer equation can be used if it can be assumed that there is a single rate-determining step that slows down the other reactions and therefore characterizes the whole reaction. For the ORR, experimental data has shown that the Butler-Volmer model cannot describe the current produced in this reaction. There is a change in the Tafel slope at a cell potential of approximately 0.8V, meaning that the mechanism is too complex to assume a single rate determining step throughout the potential range. The change in Tafel slope is typically doubled leading to higher kinetic losses in the fuel cell that are unaccounted for by the Butler-Volmer kinetic model. These Tafel slopes have been widely investigated (see Section 1.3.1) and the two slopes are generally accepted as being 60 and 120mV/dec. The lower Tafel slope of 60mV/dec occurs at lower overpotentials η, which result in low current densities. This region is known as the lcd (low current density) region. The higher Tafel slope occurs at high overpotentials, that result in high current densities. Hence is known as the hcd region.

The losses incurred in any electrochemical reaction, such as the ORR, can be reduced with the introduction of a catalyst, which allows the intermediate species to adsorb, react and/or desorb from the catalyst surface more readily. Using a platinum group metal as a catalyst is shown to have the optimal bonding characteristics for hydrogen and oxygen (the metal has an intermediate bond strength, i.e. the bond strength is not so large that it is difficult for the molecule to desorb from the surface, but not too weak that the molecule does not adsorb to begin with).

The effect of including a catalyst can be reduced by the adsorption of intermediate species onto the reaction sites. Returning to the example of the hydrogen oxidation reaction shown in equations (1.5)-(1.7), there are two adsorbed intermediate species $M \cdot H_2$ and $M \cdot H$. These species adsorb onto the surface of the platinum catalyst and if the desorption steps are kinetically slow compared to the adsorption steps, then a build up of the intermediate species will occur. This can have the effect of blocking the platinum catalyst from the reactant or it can change the activation barrier of the reactions due to the different chemical composition of the surface. The effect of coverage on the activation barrier is described by adsorption isotherm [8, 9]. Common isotherms include the Langmuirian isotherm where the coverage has no effect on the adsorption energy and Temkin isotherm where there is a linear dependence. The application of these isotherms typically depends on the extent of the intermediate coverage, for low coverages, the Langmuirian isotherm is used, while at higher coverages the Temkin isotherm should be used.

The next section will present some of the prior research that investigates the kinetics of the ORR as well as research that focuses on the numerical simulation of the cathode catalyst layer.

1.3 Literature Review

This work is primarily concerned with the kinetics of the oxygen reduction reaction and its implementation in a cathode electrode model. In section 1.3.1, research on the fundamental understanding of the ORR is presented, including experimental work that shows the complexity of the reaction and quantum mechanical studies on the elementary reactions that the ORR is assumed to be based on. Cathode catalyst layer models are presented in section 1.3.2 with a focus on how the ORR is simulated.

1.3.1 Review of Research into the ORR

1.3.1.1 The double Tafel slope

The oxygen reduction reaction is considered one of the most important reactions in the field of electrocatalysis, particularly in the field of fuel cell research [10]. Despite decades of research, its overall mechanism is not yet well understood, nor is the individual elementary reactions that result in the double Tafel slope [11]. Evidence for the existence of the double Tafel slope has been found experimentally and studied extensively over several decades [11–25]. Early techniques for measuring the kinetics of the oxygen reduction reaction were based on relatively simple electrolytic cells. An experimenter can monitor one of the half-cell reactions (i.e. the ORR in this case) by using an ideal reference electrode which is unaffected by the production of current at the electrode of interest (the working electrode), so its potential remains constant [8]. The electrodes are placed in an acid or base to allow for ionic transport and the reactants are bubbled onto the electrodes. Using this arrangement, early experimenters, in particular Bockris [12, 13] and Damjanovic [14–16] were able to show the dual Tafel slope and measured the slopes to have a magnitude of approx. 50mV/dec and 100mV/dec. These experiments were carried out using liquid electrolytes that were either acidic or alkaline, with a particular interest on the effects of pH. This value for the magnitude of the upper slope was lower than expected as Langmuirian conditions predicted a higher Tafel slope on an oxide free surface. Paucirova [17] was able to measure upper Tafel slopes with a magnitude of 120mV/dec by accounting for transient effects of the concentration of the reactants with performing the experiments.

It was thought that the effects of slow oxygen diffusion were affecting the kinetics of the ORR, so rotating disk electrodes were used to eliminate the mass transport effects [18, 26, 27]. A rotating disk electrode (RDE) is a convective electrode system whose convective and diffusive characteristics are very well understood [8], allowing the experimenter to accurately account for more physical phenomena than the electrolytic cell. In particular, mass transport effects can be accounted for through the Koutecký-Levich equation. The basic construction of the RDE consists of a disk made of the electrode material of interest, mounted on a rod of insulating material. Rotating the rod, and therefore the disk, in the liquid electrolyte will induce convective transport of the solution, maintaining a constant concentration of the reactant at the electrode and removing the product. Using this method, Tafel slopes of 60mV/dec and 120mV were consistently found and are now widely accepted [5, 28–30].

More recently Parthasarathy et al. [31, 32], Holdcroft et al. [21, 22, 33] and Zhang et al. [34] used a solid-state electrolytic cell with a micro-electrode to study the double Tafel slope. In a solid-state micro electrode cell, instead of using an liquid electrolyte, a solid Nafion membrane is used, and the size of the electrode is substantially reduced in order to eliminate mass transport effects. Parthasarathy was primarily concerned with the determination of kinetic parameters, such as the reaction order with respect to oxygen and the transfer coefficient in Nafion. Tafel slopes of approximately 60mV/dec and 120mV/dec were found, in agreement with previous experimental data. Holdcroft and Zhang investigated the properties of new membrane materials, in particular those developed by Ballard Power Systems and Foster Miller Inc., using the Nafion ionomer membrane as a benchmark. In both cases, the benchmark membrane showed a lcd Tafel slope of approx 60mV/dec, in agreement with previous research. The hcd slope was found to be lower than the expected 120mV/dec, with Holdcroft reporting slopes at approx. 100mV/dec while Zhang reported slopes of 110mv/dec. These deviations were thought to be due to imperfections in the membrane with both authors stating that the exact cause was unclear.

More novel experiments include the temperature investigation of the ORR by Wakabayashi [24] who used a closed channel flow, double electrode system. In this system, the electrolyte is continuously pumped around a closed channel. The electrolyte first comes into contact with the working electrode and almost immediately upstream is the counter electrode, with a second counter electrode further upstream.

This arrangement reduces signal noise compared to the RDE arrangement, fresh solution can be applied without contamination and can be done at higher temperatures. The Tafel slopes were found to be agreement with those reported in the literature. Dhanda et al. [25] used a novel system to investigate the effect of the structure of the platinum crystal on the kinetics of the ORR while using a solid state electrolyte, and analyzed the results using electrochemical impedance spectroscopy (EIS). The system allowed for good control of mass transport by using a forced flow of oxygen through a gap in the membrane directly onto a well defined, single crystal platinum electrode. This technique therefore also allowed for the investigation of the ORR on platinum crystals of varying orientation. The authors found Tafel slopes of approx 65mV/dec and 140mV/dec. The variation in the slopes is not discussed. Using EIS, the experimental data is fitted to a simple mechanism that assumed O_{ads} and OH_{ads} as the intermediate species and rate constants and symmetry factors for assumed intermediate steps were found.

1.3.1.2 The Mechanism of the ORR

Many of the researchers investigating the oxygen reduction reaction are concerned with determining the elementary steps by which the ORR proceeds during normal fuel cell operation and their reaction rates. Using this information, the intermediate species that are produced can be predicted. Ideally, elementary steps and reaction rates would be obtained for a wide range of operating conditions (e.g. temperature and reactant concentrations) and catalyst layer composition (e.g. for all ionomers and catalyst types and structures). This has proven enormously difficult even for the narrow range of standard operating conditions that a fuel cell operates on and for a platinum catalyst and Nafion ionomer.

The first issue addressed was the overall mechanism for the ORR. It is believed that the ORR can follow two paths, the direct four-electron transfer mechanism or the series two-electron transfer mechanism, as shown in Figure 1.4.

Yeager [27] describes the paths as follows. The four electron transfer path is written as:

$$O_2 + 4H^+ + 4e^- \rightarrow 2H_2O \tag{1.29}$$

while the the two electron path is written as:

$$O_2 + 2H^+ + 2e^- \rightarrow H_2O_2 \tag{1.30}$$

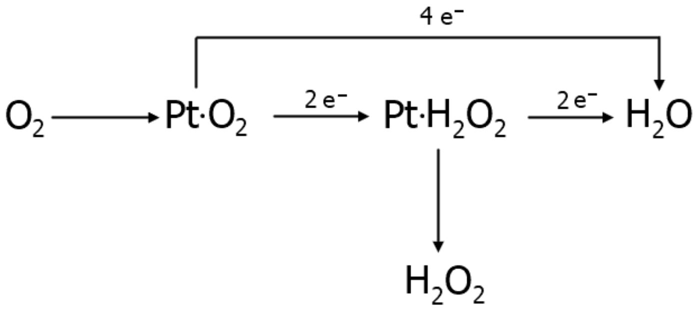

Figure 1.4: The series and direct mechansims of the ORR [26].

followed by either:

$$H_2O_2 + 2H^+ + 2e^- \rightarrow 2H_2O \tag{1.31}$$

or:

$$2H_2O_2 \rightarrow 2H_2O + O_2 \tag{1.32}$$

Advanced RDE experiments have shown that the 2 electron path, with the production of the peroxide intermediate H_2O_2, is dominated by the 4 electron transfer path [23, 27, 35] under normal fuel cell operating conditions. Yeager [27] found that peroxide formation was more significant on carbon cathodes or in alkaline solution while Paulus [23] found that for certain platinum crystal structures peroxide formation could reach as high as 6% at very low potentials (at 0.1V vs RHE). At standard FC operating voltages of 0.7-0.8V the formation was significantly lower, in the order of 0.2%. The formation of peroxide is still an active area of research however, as its formation can lead to the degradation of the Nafion membrane. Using density functional theory, Panchenko and Tripkovic [36, 37] investigated the formation of possible intermediate species, with both authors agreeing that peroxide formation to be insignificant.

Recently, the main focus of ORR kinetic research has therefore been gaining a greater understanding of the direct 4 electron path, now widely accepted to be the dominant pathway for the reaction [5, 30, 38, 39]. Of particular interest are the intermediate species that are formed during the reaction (and the quantities they are produced in) for different operating conditions and catalyst layer composition. If the rates of production of the intermediate species are known, the intermediate steps that are firing can be determined, as well as their energy barriers. This knowledge will lead to better design of catalysts that can favor one reaction over another, potentially allowing for the reduction of the kinetic losses.

It has long been assumed that the two Tafel slopes are a result of the changing coverage of the intermediate species on the catalyst [15–17]. The authors note that at low over-potentials, the intermediate species coverage is high leading to Temkin adsorption conditions, while at high over-potentials the coverage is significantly reduced, leading to Langmuirian adsorption conditions. The main distinction between the two adsorption conditions is that under Temkin adsorption conditions, the high coverage of the intermediate species leads to interaction between the adsorbed molecules and the adsorbing molecules, resulting in a dependence of the absorption energy on the coverage of the species. Under Langmuirian conditions, the absorption energy is independent of coverage [9]. This change from high to low coverage coincides with the change in Tafel slope so it is assumed that the coverage is affecting the mechanism of the ORR.

The change from high to low coverage of intermediate species can be shown experimentally using cyclic voltammetry (CV), where the working electrode potential is ramped linearly with time to a set potential, upon which the potential ramp is inverted [8]. Integration of the Pt-oxide region can be used to find the coverage of the intermediate species, which is commonly referred to as the oxide coverage in the literature. Examples of determining the oxide coverage from CVs can be seen in references [11, 40, 41]. Note that it is inaccurate to use the term ’platinum oxides’ here, as the intermediate species are not necessarily chemically, strongly bonded oxygen species *with* the platinum, they are more likely oxygen species that have been adsorbed *on* the surface of the reaction sites. Also the total coverage found using the CV method does not distinguish between different adsorbed species (e.g. it does not distinguish between O_{ads} or OH_{ads}) [42].

This uncertainty over which species were adsorbed onto the surface led to early researchers attempting to find the mechanism for the ORR by considering a wide variety of intermediate species and calculating the Tafel slope associated with an intermediate reaction that would produce the intermediate species. These slopes could then be matched against the Tafel slopes found experimentally and would then be attributed to the rate determining step of the ORR. Some of the most common intermediate adsorbed species considered include O_{ads}, $O_{2,ads}$, OH_{ads}, $H_2O_{2,ads}$, H_2O_{ads} and $HO_{2,ads}$, with a large number of paths analyzed to determine their Tafel slopes. Damjanovic [14] provides a summary of the potential pathways that were under consideration, 14 in total. Analysis of these steps, with the experimentally found Tafel slopes, gave rise to the assumption that the first charge transfer step is the rate determining step in both high and low Tafel slope regions. In a liquid electrolyte solution, this step is given as [43]:

$$O_2 + H_3O^+ + e^- \rightarrow O_2H + H_2O \tag{1.33}$$

The change in Tafel slope is attributed to the effect of the intermediate coverage on the free energy of activation of this step, which is given as the sum of the chemical and electrochemical contributions:

$$\Delta G = \Delta G_c + \beta F \Delta\phi \tag{1.34}$$

where ΔG denotes the Gibbs free energy of activation, β is the symmetry factor, normally taken as 0.5 for an elementary reaction, and $\Delta\phi$ is the potential between the electrode and the solution. The difference between the Temkin and Langmuirian adsorption isotherms are given in the dependence of the Gibbs free energy of the chemical contribution, ΔG_c. Under Langmuirian conditions, the ΔG_c is independent of coverage θ and potential $\Delta\phi$, while under Temkin conditions, ΔG_c is given as

$$\Delta G_c = \Delta G_o + \beta r(\theta - \theta_T) \tag{1.35}$$

where β is the symmetry factor, r is an energy factor and θ_T is the coverage at which the adsorption conditions change. This assumption that the RDS is the first charge transfer step is often cited when discussing the ORR [5, 30, 44]. However, it has not gained universal acceptance, for example, the chemical adsorption of O_2 onto the platinum was proposed as the RDS by Yeager [27]. Further, Parthasarathy found that for a solid state electrolytic cell, the RDS was likely to be a chemical step followed by the first electron transfer step at low current densities [32]. Hence, the nature of the ORR is still undecided.

1.3.1.3 Advanced Techniques

Recently, quantum mechanical (QM) models have allowed researchers to simulate the interaction between different species and catalyst at the atomic level. An example of a simulation is a single oxygen atom approaching a cluster of platinum atoms, where the breaking and formation of atomic bonds are simulated to find the most likely adsorption configuration. A commonly used method in quantum mechanical modeling is density functional theory (DFT), where the electronic energy density around the nucleus is solved for. More information on this method is found in [6, 38, 41, 44]. An early example of using DFT to analyze the ORR, was by Sidik [45], who modeled the interaction of two platinum atoms with a hydronium ion and two water molecules. They found that the electrochemical reaction:

$$O_2 + H^+ + e^- \rightarrow O_2H \tag{1.36}$$

was the rate determining step with an activation energy of 0.6eV at a cell potential of 1.23V. Norskov et al. [46] considered a simple dissociative mechanism, with O_{ads} and OH_{ads} as intermediate species and found the free energies of adsorption ranged between 0.8eV and 1.76eV for OH_{ads} and 1.58eV and 2.41eV for O_{ads} where the range in values is due to the effect of the coverage of the O_{ads} species. Further, a free energy diagram was presented for this reaction, that showed the variation of the free energies with change in potential. An associative mechanism was also considered where the oxygen does not dissociate into individual oxygen atom before the first charge transfer step. This results in the consideration of the $O_{2,ads}$ and $HO_{2,ads}$ intermediate species. Again a free energy diagram was constructed that showed the mechanisms dependence on potential and coverage. Norskov et al. concluded that both associative and dissociative pathways could contribute to the ORR. Walch [30] investigated a number of chemical reactions thought to be part of the ORR. It was found that the size and structure of the simulated platinum cluster played a large role in determining the barrier energy. It was also noted that the choice of approximation method could have a large effect on the computed binding energies. Keith [41] gives a review of DFT models in the literature and notes that while visualization techniques found that O_2 binds to platinum with a binding energy of 0.3-0.5eV, the range using DFT calculations was 0.1-1.95eV depending on the model used. Other factors that produced large deviations in results include the assumed binding site for the intermediate species and the geometry of the reaction site. In particular, Keith investigated the assumption of the gaseous reactants being solvated in the water and found that if this assumption is not made, the pathway for the ORR would proceed via the two electron path rather than the widely accepted four electron path. Fang [44] notes further complication in properly accounting for the cell potential in DFT calculations (normally an electrical field is applied to the domain to represent the potential, however the correlation is difficult to quantify). Complications such as those noted by Walch, Keith and Fang make simulation using QM difficult and applying results to fuel cell modeling should be done with caution. However, the technology is still relatively new and it is expected that further research will eliminate some of these issues so that it becomes a more prominent tool in the future.

1.3.2 Mathematical Modeling of the ORR

1.3.2.1 Modeling ORR kinetics

Markovic [47] investigated the kinetics of the ORR in a bromide electrolyte using RDE experiments, as adsorption of OH_{ads} onto to platinum sites is suppressed in the presence of Br^- anions. A theoretical model was derived that accounted for the effects of the coverage of the OH_{ads}, in particular, 1) a site blocking effect of the adsorbates as they compete with the oxygen molecules that try to adsorb onto the platinum and 2) the alteration of the free energy of adsorption of the intermediates by the presence of OH_{ads} on sites adjacent to the reaction site. These effects are accounted for by the following equation:

$$j = nFkc_{O_2}(1-\theta_{ad})^x \exp(-\beta FE/RT)\exp(-\gamma r\theta_{ad}/RT) \tag{1.37}$$

where n is the number of electrons, k is the rate constant for the rate determining step (again assumed to be the first charge transfer step), c_{O_2} is the concentration of O_2 in the solution, x is the number of Pt sites occupied by the adsorbed ion (varies from 1-3, i.e. an adsorbed molecule can block up to 3 platinum sites), j is the observed current density, E is the cell potential, β and γ are symmetry factors (assumed to be 0.5), and r is an energy parameter for the Temkin isotherm that defines the effect of the coverage on the free energy of adsorption of the adsorbing species. Note that there are two additional terms in equation (1.37) with respect to the standard Tafel equation, namely a pre-exponential factor $(1-\theta_{ad})^x$ that accounts for the site blocking effect of the intermediates and an additional exponential factor $\exp(-\gamma r\theta_{ad}/RT)$ that accounts for the change in free energy of adsorption.

Wang [48] derived a novel kinetic model based on the free energies of activation of four assumed steps and free energies of adsorption of two intermediate species. This model can show the change in slope (though the slopes predicted are not the widely accepted 60mV/dec and 120mV/dec) and shows the high coverage of oxides in the lcd region and low coverage in the hcd region. This model does not use the coverage of the intermediate species as an input parameter, as is the case for the model proposed by Markovic et al., nor is there an assumption of a rate determining step. The model is instead based on the free energies of activation of the assumed intermediate steps and the free energies of absorption of the intermediate species. These free energies could be found using *ab-initio* techniques such as quantum mechanical modeling and would therefore not require the use of experimental data. The aim of this work is to investigate the model proposed by Wang et al., and its implementation into a fuel cell model. It is described in greater detail in the following chapter.

1.3.2.2 The ORR in fuel cell modeling

To date, 1D, 2D and 3D fuel cell mathematical models typically represent the ORR using either the Butler-Volmer equation or the Tafel equation [49–61]. Authors often cite Parthasarathy et al. [31, 32] when choosing the kinetic parameters such as the oxygen reaction order or the transfer coefficient [51, 55, 57, 58, 60, 61]. However, modelers typically only choose parameters that characterize a single Tafel slope region, so the doubling of the Tafel slope is not accounted for. Broka et al. [51] investigated the influence of a number of parameters such as oxygen permeability on polarization curves produced from assuming either a pseudohomogeneous film or agglomerate CCL model. The hcd Tafel slope and exchange current from Parthasarathy was used to model the ORR reaction. Um et al. [55] modeled a transient, multi-component, multi-dimensional MEA using a CFD package and used the exchange current density and the open circuit potential found by Parthasarathy et al. Secanell and Dobson [57, 60, 61] used the lcd kinetic transfer coefficient from Parthasarathy along with parameters such as the exchange current density and oxygen reaction order. Sun et al. [58] investigated structural parameters that characterize a catalyst layer agglomerate model and, based on the data from Parthasarathy et al., switch from a transfer coefficient of one to one half when the cell potential drops below 0.8V. This switch will approximately return the correct Tafel slopes, however, the potential at which the switch occurs is constant which is not observed experimentally. A similar technique is used for the exchange current density and the value for oxygen diffusivity in Nafion is also taken from Parthasarathy et al. Despite the extensive research describing the changing Tafel slopes, the majority of researchers do not account for the losses from the change in Tafel slope when performing fuel cell simulations. The losses attributed to the change in Tafel slope are instead considered insignificant compared to other losses, or their existence is not acknowledged during PEM fuel cell operation. The losses are instead interpreted as being due to oxygen diffusion through the agglomerate structure of the catalyst layer or through liquid water [62, 63].

Suzuki [64] used Markovic's model [47] in a one dimensional fuel cell model that used the diffusion coefficient for oxygen as a fitting parameter. Linear sweep voltammetry (LSV) was used to find the potential dependent oxide coverage in both the anodic and cathodic directions and with this as an input to the model, the change in Tafel slope was reproduced. Subramanian [11] also used this model, with CV experiments used to find the change in oxide coverage. The equation was changed slightly from that presented in equation (1.37) so that the reference exchange current density was used instead of the rate constant. This, along with γr and the oxygen partial pressure were fitted to experimental data that accounted for all known transport losses such as oxygen diffusion and proton transport. Experimental results and results from the coverage dependent model were compared to a simple constant Tafel slope kinetic model presented by Neyerlin [63]. Both comparisons show the effect of the double Tafel slope, where Neyerlin's model was unable to capture the additional losses.

1.4 Contributions

The aim of this work is to contribute to the research being done in the area of fuel cell mathematical modeling by incorporating an accurate representation of the kinetics of the oxygen reduction reaction. The research will mainly take the form of the mathematical modeling of a novel kinetic model of the ORR in a fuel cell simulation. The main contributions to literature are:

1. Reformulation of the novel kinetic model proposed by Wang in order to correctly account for the local oxygen content at the reaction sites and the backward reactions.

2. Parametric estimation of the kinetic parameters that characterize the kinetic model, based on data obtained from the literature.

3. Integration of the kinetic model into an existing, 2D fuel cell MEA model and analysis of the model in comparison to the commonly used Tafel equation.

1.5 Thesis Outline

The first chapter presents a background on the kinetics of electrochemical reactions and on the structure and operation of a PEM fuel cell. Chapter 2 describes the novel kinetic model developed by Wang and the reformulation that correctly accounts for the oxygen concentration in the layer. The method for fitting the kinetic parameters to the model is then described, and the kinetics of the ORR are investigated, with an emphasis on the effect of the assumed intermediate species present in the CCL. In Chapter 3, the integration of the new kinetic model into a full MEA model is described. The effect of replacing the standard Tafel equation is investigated by means of parametric studies on the operating conditions of the cell and the structural parameters that characterize it. Chapter 4 will present the final conclusions as well as possibilities for future research.

Chapter 2

Kinetic Model

2.1 Introduction

In the previous chapter, a review of the research being undertaken in the field of the electrochemistry of the ORR in a fuel cell was presented. The review was by no means exhaustive and, as no conclusive consensus has been reached on the mechanism of the oxygen reduction reaction (ORR), it is clear that this is a complex and difficult area of research. Most fuel cell mathematical models to date simply use a Tafel equation to describe the reaction. A simple Tafel equation hides the complex, multi-step nature of the reaction, which can lead to significant errors in the predicted performance of the cell. Wang et al. [4], derived a novel kinetic model based on four intermediate steps, producing two intermediate adsorbed species, that uses the free energy of activation of the four steps and the free of energies of adsorption of the intermediate species as unknown kinetic parameters. This model is capable of predicting a change in Tafel slope and does not assume a rate determining step.

In this chapter, the double-trap, intrinsic kinetic pathway suggested by Wang [4] is presented. This model can better capture the characteristics of the reaction, in particular, the change in the Tafel slope and the production of intermediate species. This model is similar to one of the bifurcation branches in the advanced ORR kinetic model described by Ruvinskiy et al. [65], that also accounts for the 'series' pathway and the production of hydrogen peroxide. The first section will introduce the mathematical model and its derivation, and it will present the final equation that describes the production of current in the cell as well as expressions for the coverage of the intermediate species. The second section will present a validation study of the implementation of the model in the fuel cell modeling software. This validation will be based on the kinetic parameters presented by Wang et al. and deficiencies in the model will be discussed. The third section will describe the parameter estimation process that will be used to predict the new kinetic parameters for the model and the results from this process. The final section will present results from a study of the kinetic model with the new fitted parameters, in particular, examination of the predicted current, coverages and the energy barriers for each of the intermediate steps.

2.2 Double Trap Kinetic Model

2.2.1 Derivation

To derive the intrinsic kinetic equation, Wang et al. [4] assumed that there were four intermediate paths in the ORR and only two strongly adsorbed intermediates O_{ads} and OH_{ads}, as these intermediates are the most stable. The four reactions are given by:

$$1/2O_2 \Leftrightarrow O_{ads} \qquad \text{Dissociative Adsorption (DA)} \tag{2.1}$$

$$1/2O_2 + H^+ + e^- \Leftrightarrow OH_{ads} \qquad \text{Reductive Adsorption (RA)} \tag{2.2}$$

$$O_{ads} + H^+ + e^- \Leftrightarrow OH_{ads} \qquad \text{Reductive Transition (RT)} \tag{2.3}$$

$$OH_{ads} + H^+ + e^- \Leftrightarrow H_2O \qquad \text{Reductive Desorption (RD)} \tag{2.4}$$

The first reaction is the dissociative adsorption of oxygen onto the platinum surface. This reaction does not involve externally provided electrons and protons so it is assumed that its reaction rate is unaffected by the presence of the potential difference across the electrode/electrolyte interface. The intermediate produced in the reaction is adsorbed oxygen, O_{ads}. The second reaction is the reductive adsorption (RA) of molecular oxygen producing the second adsorbed species, hydoxyl (OH_{ads}). The reductive transition (RT) is the reduction of adsorbed oxygen to adsorbed hydroxyl while the final step is the reduction of adsorbed hydroxyl to produce water. The reductive steps involve the consumption of electrons and are therefore electrochemical reactions. Unlike the DA step, they will be affected by the cell potential. The DA and RA steps involve oxygen as the reactant and will depend on the local concentration of oxygen. The electrochemical steps will depend on the local concentration of hydrogen ions.

Note that these reactions can proceed in either the forward or backward direction, depending on the applied cell potential, the free energies of activation of the

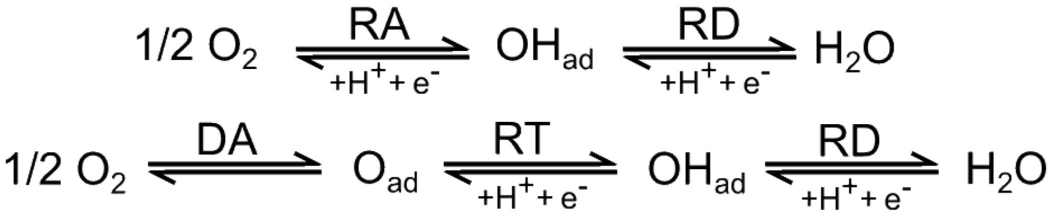

Figure 2.1: The assumed paths and intermediate species of the ORR [48].

steps and the free energies of adsorption of the intermediate species. While the free energies will be fixed values, the cell potential can vary during fuel cell operation, leading to some steps becoming more dominant than others at different potentials. Also note that the fractional stoichiometric number used in equations (2.1) and (2.2) is a simplification that allows for each step to be written as a single electron transfer reaction. It also removes a quadratic dependence on the coverage. A similar analysis to that done in Chapter 1 to derive the Butler-Volmer equation can therefore be used. The adsorption of molecular oxygen onto the platinum site could be a complex reaction with its own intermediate steps, as is suggested by Ruvinskiy et al. [65]. This simplification is justified by the original authors who found that the RT and RD steps were of more importance than the DA and RA steps, therefore the fractional number was chosen for simplicity. This may lead to inaccuracies in the model.

From examination of the assumed steps, it is clear that the starting point for the overall reaction is the adsorption of oxygen onto the platinum reaction site. This can occur through either the DA or RA step, producing two possible intermediates. The final step is the production of the water. Water production is achieved by the RD step only. This must therefore be the final step of the reaction and may only proceed by the reaction of the hydroxyl intermediate. Therefore, the two potential ORR pathways are (RA)→(RD) or (DA)→(RT)→(RD) as is shown schematically in Figure 2.1. Note that these paths can occur concurrently and no assumptions are made regarding a rate determining step. The rates of each reaction are determined using transition state theory [8], in a similar manner to the derivation of the Butler-Volmer equation in Chapter 1.

The reaction rate of each of the steps is given as [8]:

$$\nu_{DA} = k_{DA} c_{O_2}^{\frac{1}{2}} \theta_{Pt} - k_{-DA} \theta_{O} \tag{2.5}$$

$$\nu_{RA} = k_{RA} c_{O_2}^{\frac{1}{2}} c_{H^+} e^{-\beta E/kT} \theta_{Pt} - k_{-RA} e^{(1-\beta)E/kT} \theta_{OH} \tag{2.6}$$

$$\nu_{RT} = k_{RT} c_{H^+} e^{-\beta E/kT}(\theta_O) - k_{-RT} e^{(1-\beta)E/kT} \theta_{OH} \tag{2.7}$$

$$\nu_{RD} = k_{RD} c_{H^+} e^{-\beta E/kT}(\theta_{OH}) - k_{-RD} e^{(1-\beta)E/kT} \theta_{Pt} \tag{2.8}$$

The reaction rate ν_i, where i denotes one of the four steps, depends on a rate constant k_i and the concentration of the reactant, c_i. Note that the concentration of the adsorbed species is given in terms of the coverage of the species, θ_i. For the DA step the reverse reaction rate will depend on the coverage of the adsorbed oxygen, which is given by the θ_O term. In the forward direction, the oxygen reacts with the clean platinum surface. This will have a coverage given by the number of sites not covered by the two intermediate species, i.e. one minus the two coverages: $(1 - \theta_O - \theta_{OH})$. For brevity, the coverage of the clean platinum surface will be denoted by θ_{Pt}.

For a multi-step reaction the current produced is equal to the sum of the reaction rates of the steps that involve the transfer of an electron times Faraday's constant. Therefore, the current density produced in the overall reaction will be given by equation

$$j_k = F(\nu_{RA} + \nu_{RT} + \nu_{RD}) \tag{2.9}$$

If the reactions are at steady state, there will be no transient behavior in the production of the intermediate species. Then,

$$\frac{\mathrm{d}\theta_O}{\mathrm{d}t} = \nu_{DA} - \nu_{RT} = 0 \tag{2.10}$$

The production of θ_O will be governed by the relative speeds of the DA reaction that produces it and the RT reaction that consumes it. Therefore at steady state these rates must be in equilibrium.

For the θ_{OH} intermediate, the RA and RT steps that produce it are in equilibrium with the RD step that consumes the intermediate.

$$\frac{\mathrm{d}\theta_{OH}}{\mathrm{d}t} = \nu_{RA} + \nu_{RT} - \nu_{RD} = 0 \tag{2.11}$$

The substitution of these relationships into equation (2.9), will result in the kinetic current being given by

$$j_k = 2F\nu_{RD} = 2j_{RD} \tag{2.12}$$

where the kinetic current is given by the rate of the RD step only. The reaction constants, k_i, are difficult to determine either theoretically or experimentally so, as is done for the Butler-Volmer equation, the kinetic current produced according to the double trap equation is defined by the departure of the cell potential from equilibrium.

The equilibrium cell potential E_{eq} is used as a reference point. The reaction rate, kinetic current and coverage at this point are termed the exchange rates, ν^0, current j^0 and coverage θ_i^0 respectively. Note that the overall reaction rates are zero at the reference potential, therefore the forward and backward rates are equal. The exchange rate is then defined as:

$$\nu_{DA}^0 = k_{DA}(c_{O_2}^{ref})^{\frac{1}{2}}\theta_{Pt}^0 = k_{-DA}\theta_O^0 \tag{2.13}$$

$$\nu_{RA}^0 = k_{RA}(c_{O_2}^{ref})^{\frac{1}{2}}c_{H^+}^{ref}e^{-\beta E_{eq}/kT}\theta_{Pt}^0 = k_{-RA}e^{(1-\beta)E_{eq}/kT}\theta_{OH}^0 \tag{2.14}$$

$$\nu_{RT}^0 = k_{RT}c_{H^+}^{ref}e^{-\beta E_{eq}/kT}(\theta_O^0) = k_{-RT}e^{(1-\beta)E_{eq}/kT}\theta_{OH}^0 \tag{2.15}$$

$$\nu_{RD}^0 = k_{RD}c_{H^+}^{ref}e^{-\beta E_{eq}/kT}(\theta_{OH}^0) = k_{-RD}e^{(1-\beta)E_{eq}/kT}\theta_{Pt}^0 \tag{2.16}$$

where c_i^{ref} is the concentration of either oxygen or hydrogen ions at zero overpotential. As this case of zero overpotential is used as a reference point, the value of $e^{\beta E_{eq}/kT}$ is set to one.

Unlike the original authors of the model, here the reactant concentration is not considered to be constant. The concentration of c_{O_2/H^+}^{ref} at zero overpotential is the reference concentration, as was used in Chapter 1. This addition to the kinetic model will correctly account for the local oxygen concentration, which is of particular significant importance when determining the coverage of the intermediate species [66] and capturing the mass transport limiting region. The modification in the derivation can produce mass transport limiting effects similar to those found with the Tafel model. This effect is not seen with the original derivation, mass transport limiting effects are accounted by assuming a linear relationship between the current and the oxygen concentration. This approach requires the estimation of the value of the limiting current which, along with the assumption of the linear dependence of the current with the oxygen concentration, could result in significant inaccuracies.

The equilibrium free energies of adsorption of the intermediates can be defined using a Langmuirian isotherm [9]:

$$e^{-\Delta G_O^0} = \frac{\theta_O^0}{\theta_{Pt}^0} \tag{2.17}$$

$$e^{-\Delta G_{OH}^0} = \frac{\theta_{OH}^0}{\theta_{Pt}^0} \tag{2.18}$$

The free energies of adsorption are therefore equal to the ratio of the fraction of sites covered by the intermediate divided by the number of sites that are free of any intermediates, i.e. are 'clean'. These free energies represent the free energy of the intermediate once it is formed, i.e. the position of the 'Products' in Figure 1.2.

Based on the reaction rates at zero overpotential, the exchange currents can be defined. The original authors defined these currents as being independent of the coverage and so they are termed the intrinsic exchange currents. Using the formula $j_i = F\nu_i$ and equations (2.13)-(2.16):

$$j^0_{DA} = \frac{F\nu^0_{DA}}{\theta^0_{Pt}} = Fk_{DA}(c^{ref}_{O_2})^{\frac{1}{2}} = j^*_{DA}e^{-\Delta H^{*0}_{DA}/kT} = j^*e^{-\Delta G^{*0}_{DA}/kT} \tag{2.19}$$

$$j^0_{RA} = \frac{F\nu^0_{RA}}{\theta^0_{Pt}} = Fk_{RA}(c^{ref}_{O_2})^{\frac{1}{2}}c^{ref}_{H^+} = j^*_{RA}e^{-\Delta H^{*0}_{RA}/kT} = j^*e^{-\Delta G^{*0}_{RA}/kT} \tag{2.20}$$

$$j^0_{RT} = \frac{F\nu^0_{RT}}{(\theta^0_{O})} = Fk_{RT}c^{ref}_{H^+} = j^*_{RT}e^{-\Delta H^{*0}_{RT}/kT} = j^*e^{-\Delta G^{*0}_{RT}/kT} \tag{2.21}$$

$$j^0_{RD} = \frac{F\nu^0_{RD}}{(\theta^0_{OH})} = Fk_{RD}c^{ref}_{H^+} = j^*_{RD}e^{-\Delta H^{*0}_{RD}/kT} = j^*e^{-\Delta G^{*0}_{RD}/kT} \tag{2.22}$$

Here we apply the Arrhenius equation to relate the rate constants k_i to the free energies of activation ΔG^{*0}_i, as was done in Chapter 1. The pre-exponential factor j^*_i will be a combination of the pre-exponential factor A from the Arrhenius equation, c^{ref}_i, which is constant and Faraday's constant F. The pre-exponential factor j^*_i is assumed to be related to the entropy change of the reaction, i.e. $j^*_i = j^*\mathrm{e}^{\Delta S^0_i/kT}$, where j^* is termed the reference prefactor for the reaction [4]. This factor can be considered a scaling factor. G^{*0}_i is the free energy of activation of the ith step and are unknown variables of the system of equations that will be found using data fitting. This will be described in more detail in section 2.4. These parameters represent the height of the activation barrier that must be overcome before the reaction will proceed, as shown in Figure 1.2.

Now that the reference point and corresponding exchange reaction rates, currents and coverages are defined, the intrinsic reaction rates, currents and coverages at other potentials can be obtained. The original reaction rates, i.e. equations (2.5)-(2.8), are divided by the exchange reaction rates, equations (2.13) - (2.16), to get the intrinsic reaction rates.

$$\frac{\nu_{DA}}{\nu^0_{DA}} = \frac{k_{DA}c^{\frac{1}{2}}_{O_2}\theta_{Pt}}{k_{DA}(c^{ref}_{O_2})^{\frac{1}{2}}\theta^0_{Pt}} - \frac{k_{-DA}\theta_O}{k_{-DA}\theta^0_O} \tag{2.23}$$

$$\frac{\nu_{RA}}{\nu^0_{RA}} = \frac{k_{RA} c_{O_2}^{\frac{1}{2}} c_{H^+} e^{-\beta E/kT}\theta_{Pt}}{k_{RA}(c^{ref}_{O_2})^{\frac{1}{2}} c^{ref}_{H^+} e^{-\beta E_{eq}/kT}\theta^0_{Pt}} - \frac{k_{-RA}e^{(1-\beta)E/kT}\theta_{OH}}{k_{-RA}e^{(1-\beta)E_{eq}/kT}\theta^0_{OH}} \tag{2.24}$$

$$\frac{\nu_{RT}}{\nu^0_{RT}} = \frac{k_{RT} c_{H^+} e^{-\beta E/kT}\theta_{O}}{k_{RT} c^{ref}_{H^+} e^{-\beta E_{eq}/kT}\theta^0_{O}} - \frac{k_{-RT}e^{(1-\beta)E/kT}\theta_{OH}}{k_{-RT}e^{(1-\beta)E_{eq}/kT}\theta^0_{OH}} \tag{2.25}$$

$$\frac{\nu_{RD}}{\nu^0_{RD}} = \frac{k_{RD} c_{H^+} e^{-\beta E/kT}\theta_{OH}}{k_{RD} c^{ref}_{H^+} e^{-\beta E_{eq}/kT}\theta^0_{OH}} - \frac{k_{-RD}e^{(1-\beta)E/kT}\theta_{Pt}}{k_{-RD}e^{(1-\beta)E_{eq}/kT}\theta^0_{Pt}} \tag{2.26}$$

Note that unlike the original derivation, there is now a ratio between the local species concentration and the reference species concentration. Due to the presence of the ionomer film that conducts the protons, it can be assumed that the concentration of protons is constant through the layer and that it will be equal to the reference concentration. Hence equations (2.23)-(2.26) become:

$$\frac{\nu_{DA}}{\nu^0_{DA}} = \left(\frac{c_{O_2}}{c^{ref}_{O_2}}\right)^{\frac{1}{2}} \frac{\theta_{Pt}}{\theta^0_{Pt}} - \frac{\theta_O}{\theta^0_O} \tag{2.27}$$

$$\frac{\nu_{RA}}{\nu^0_{RA}} = \left(\frac{c_{O_2}}{c^{ref}_{O_2}}\right)^{\frac{1}{2}} \frac{e^{-\beta E/kT}\theta_{Pt}}{e^{-\beta E_{eq}/kT}\theta^0_{Pt}} - \frac{e^{(1-\beta)E/kT}\theta_{OH}}{e^{(1-\beta)E_{eq}/kT}\theta^0_{OH}} \tag{2.28}$$

$$\frac{\nu_{RT}}{\nu^0_{RT}} = \frac{e^{-\beta E/kT}\theta_{O}}{e^{-\beta E_{eq}/kT}\theta^0_{O}} - \frac{e^{(1-\beta)E/kT}\theta_{OH}}{e^{(1-\beta)E_{eq}/kT}\theta^0_{OH}} \tag{2.29}$$

$$\frac{\nu_{RD}}{\nu^0_{RD}} = \frac{e^{-\beta E/kT}\theta_{OH}}{e^{-\beta E_{eq}/kT}\theta^0_{OH}} - \frac{e^{(1-\beta)E/kT}\theta_{Pt}}{e^{(1-\beta)E_{eq}/kT}\theta^0_{Pt}} \tag{2.30}$$

Rearranging and noting that $j_i = F\nu_i$, the previous system of equations can be written as:

$$j_{DA} = \frac{F\nu^0_{DA}}{\theta^0_{Pt}}\left(\left(\frac{c_{O_2}}{c^{ref}_{O_2}}\right)^{\frac{1}{2}}\theta_{Pt} - \frac{\theta^0_{Pt}}{\theta^0_O}\theta_O\right) \tag{2.31}$$

$$j_{RA} = \frac{F\nu^0_{RA}}{\theta^0_{Pt}}\left(\left(\frac{c_{O_2}}{c^{ref}_{O_2}}\right)^{\frac{1}{2}} e^{-\beta\eta/kT}\theta_{Pt} - e^{(1-\beta)\eta/kT}\frac{\theta^0_{Pt}}{\theta^0_{OH}}\theta_{OH}\right) \tag{2.32}$$

$$j_{RT} = \frac{F\nu^0_{RD}}{\theta^0_O}\left(e^{-\beta\eta/kT}\theta_O - e^{(1-\beta)\eta/kT}\frac{\theta^0_{Pt}}{\theta^0_{OH}}\frac{\theta^0_O}{\theta^0_{Pt}}\theta_{OH})\right) \tag{2.33}$$

$$j_{RD} = \frac{F\nu^0_{RD}}{\theta^0_{OH}}\left(e^{-\beta\eta/kT}\theta_{OH} - e^{(1-\beta)\eta/kT}\frac{\theta^0_{OH}}{\theta^0_{Pt}}\theta_{Pt}\right) \tag{2.34}$$

Note that the two exponential terms have been combined to give a single exponential term that depends on the overpotential, (where the overpotential is defined as the cell potential minus the equilibrium potential, $\eta = E - E_{eq}$).

Now substituting equations (2.19)-(2.22) and (2.17)-(2.18) into the previous equations, the equations describing the current produced by each step can be written as:

$$j_{DA} = j^* \left(\frac{c_{O_2}}{c_{O_2}^{ref}} \right)^{\frac{1}{2}} e^{-\Delta G^*_{DA}/kT} \theta_{Pt} - j^* e^{-\Delta G^*_{-DA}/kT} \theta_O \tag{2.35}$$

$$j_{RA} = j^* \left(\frac{c_{O_2}}{c_{O_2}^{ref}} \right)^{\frac{1}{2}} e^{-\Delta G^*_{RA}/kT} \theta_{Pt} - j^* e^{-\Delta G^*_{-RA}/kT} \theta_{OH} \tag{2.36}$$

$$j_{RT} = j^* e^{-\Delta G^*_{RT}/kT} \theta_O - j^* e^{-\Delta G^*_{-RT}/kT} \theta_{OH} \tag{2.37}$$

$$j_{RD} = j^* e^{-\Delta G^*_{RD}/kT} \theta_{OH} - j^* e^{-\Delta G^*_{-RD}/kT} \theta_{Pt} \tag{2.38}$$

where the potential-dependent free energies of activation ΔG^*_i are:

$$\begin{aligned}
\Delta G^*_{DA} &= \Delta G^{*0}_{DA} & \Delta G^*_{-DA} &= \Delta G^{*0}_{DA} - \Delta G^0_O & (2.39)\\
\Delta G^*_{RA} &= \Delta G^{*0}_{RA} + \beta e\eta & \Delta G^*_{-RA} &= \Delta G^{*0}_{RA} - \Delta G^0_{OH} - \beta e\eta & (2.40)\\
\Delta G^*_{RT} &= \Delta G^{*0}_{RT} + \beta e\eta & \Delta G^*_{-RT} &= \Delta G^{*0}_{RT} - \Delta G^0_{OH} + \Delta G^0_O - \beta e\eta & (2.41)\\
\Delta G^*_{RD} &= \Delta G^{*0}_{RD} + \beta e\eta & \Delta G^*_{-RD} &= \Delta G^{*0}_{RD} + \Delta G^0_{OH} - \beta e\eta & (2.42)
\end{aligned}$$

where e is the charge of a single electron and is used to convert the units from volts to electron-volts.

The kinetic current produced in the reaction is given by equation (2.12) $j_k = 2j_{RD}$:

$$j_k = 2j^* e^{-\Delta G^*_{RD}/kT} \theta_{OH} - 2j^* e^{-\Delta G^*_{-RD}/kT} \theta_{Pt} \tag{2.43}$$

where here the backward rate is included. The original authors omitted the backward rate, as it was found to be insignificant. However, as the kinetic parameters will be fitted to the model, the backward step may become significant as the kinetic parameters are modified during the fitting process.

An expression for the coverages of the intermediate species can be found by returning to the steady state equations (2.10) and (2.11) and substituting in equations (2.35) to (2.38), again noting that $j_i = F\nu_i$:

$$C g_{DA} \theta_{Pt} - g_{-DA} \theta_O - g_{RT} \theta_O + g_{-RT} \theta_{OH} = 0 \tag{2.44}$$

$$C g_{RA} \theta_{Pt} - g_{-RA} \theta_{OH} + g_{RT} \theta_O + g_{-RT} \theta_{OH} - g_{RD} \theta_{OH} + g_{-RD} \theta_{Pt} = 0 \tag{2.45}$$

where $g_i = e^{-\Delta G^*_i/kT}$ and:

$$C = \left(\frac{c_{O_2}}{c_{O_2}^{ref}} \right)^{1/2} \tag{2.46}$$

These equations can be rearranged into a pair of linear equations:

$$0 = (Cg_{DA} + g_{-DA} + g_{RT})\theta_O + (Cg_{DA} + g_{-RT})\theta_{OH} - Cg_{DA} \tag{2.47}$$

$$\begin{aligned} 0 = {} & (Cg_{RA} - g_{RT} + g_{-RD})\theta_O + (Cg_{RA} + g_{-RA} + g_{-RT} + g_{RD} + g_{-RD})\theta_{OH} \\ & - (Cg_{RA} + g_{-RD}) \end{aligned} \tag{2.48}$$

Solving these equations will give the following expressions for the OH_{ads} and O_{ads} coverages:

$$\theta_{OH} = \frac{Cg_{DA}(Cg_{RA}+g_{-RD}-g_{RT})-(Cg_{RA}+g_{-RD})(Cg_{DA}+g_{-DA}+g_{RT})}{(Cg_{DA}-g_{-RT})(Cg_{RA}+g_{-RD}-g_{RT})-(Cg_{RA}+g_{-RA}+g_{-RT}+g_{RD}+g_{-RD})(Cg_{DA}+g_{-DA}+g_{RT})} \tag{2.49}$$

$$\theta_O = \frac{Cg_{DA}(Cg_{RA}+g_{-RA}+g_{-RT}+g_{RD}+g_{-RD})-(Cg_{RA}+g_{-RD})(Cg_{DA}-g_{-RT})}{(Cg_{DA}+g_{-DA}+g_{RT})(Cg_{RA}+g_{-RA}+g_{-RT}+g_{RD}+g_{-RD})-(Cg_{RA}+g_{-RD}-g_{RT})(Cg_{DA}-g_{-RT})} \tag{2.50}$$

The final system of equations that needs to be solved is given by:

- equation (2.43), which describes the current produced in the cell.
- equations (2.49) and (2.50), which describe the coverage of the intermediate species.
- equations (2.39)-(2.42), which are the potential-dependent activation energies for each of the intermediate steps.

2.3 Preliminary Results

The system of equations presented in the previous section were implemented in an in-house PEM fuel cell simulation software, the Fuel Cell Simulation Toolbox (FCST). This software is described in Chapter 3, along with the full set of equations that describe fuel cell operation. Before implementing the model in a full fuel cell simulation, the kinetic model was investigated in isolation in order to analyze the kinetics of the ORR. The first step was to validate the implementation of the model in the FCST code, using data from the original authors.

2.3.1 Model Implementation

In order to analyze this kinetic model, Wang et al. first obtained values for the unknown kinetic parameters, i.e. the free energies of adsorption of the two adsorbed species and the free energies of activation of the intermediate steps. Kinetic data

Table 2.1: Free energies of activation and adsorption as fitted by Wang et al. from RDE experiments [4]. Units are in eV.

ΔG^{*0}_{DA}	ΔG^{*0}_{RA}	ΔG^{*0}_{RT}	ΔG^{*0}_{RD}	ΔG^{*0}_{O}	ΔG^{*0}_{OH}
0.258	0.459	0.502	0.455	-0.477	-0.12

was obtained from RDE experiments and the model was fitted to the resulting polarization curve [4]. The authors note the difficulty in fitting the parameters, noting large uncertainties for the adsorption free energies. This was due to the lack of experimental data describing the coverage of the individual intermediates. The OH_{ad} free energy was fixed to $-0.12eV$ to ensure that the total coverage at low overpotentials was close to unity, while the RD step activation free energy was fixed to $0.455eV$, as it ensured a close fit to the kinetic data, allowing the other four parameters to vary. Table 2.1 shows the results from the parameter fitting.

Wang et al. further investigated this model by fitting the parameters to kinetic data obtained from PEM fuel cell experiments [48]. Experimental data was obtained from a fuel cell running on hydrogen and air at 80℃ and 100% humidity, in order to obtain a polarization curve. Kinetic data was extracted from the experimental data by accounting for the major losses incurred in a fuel cell. Many of the losses, such as the membrane resistance, were not considered significant by the authors so only the losses due to the cathode kinetics and oxygen depletion were taken into account. The kinetic losses are the losses being extracted from the data, while the oxygen depletion was accounted for by assuming a linear dependence of the oxygen concentration with the produced current

$$\frac{c_{O_2}}{c^{ref}_{O_2}} = 1 - \frac{j}{j_L} \tag{2.51}$$

where $c^{ref}_{O_2}$ is the reference oxygen concentration and j_L is the limiting current, i.e. the maximum current that can be produced before the oxygen is entirely consumed in the catalyst layer. Again, this equation is needed as the original model cannot correctly account for oxygen depletion. This is not the case with the modified derivation presented in this work.

The resulting polarization curve is shown in Figure 2.2(a). As is clear from the figure, the experimental data is best captured using the double kinetic model, with the commonly used Tafel kinetic model resulting in significant over-estimation of the cell performance.

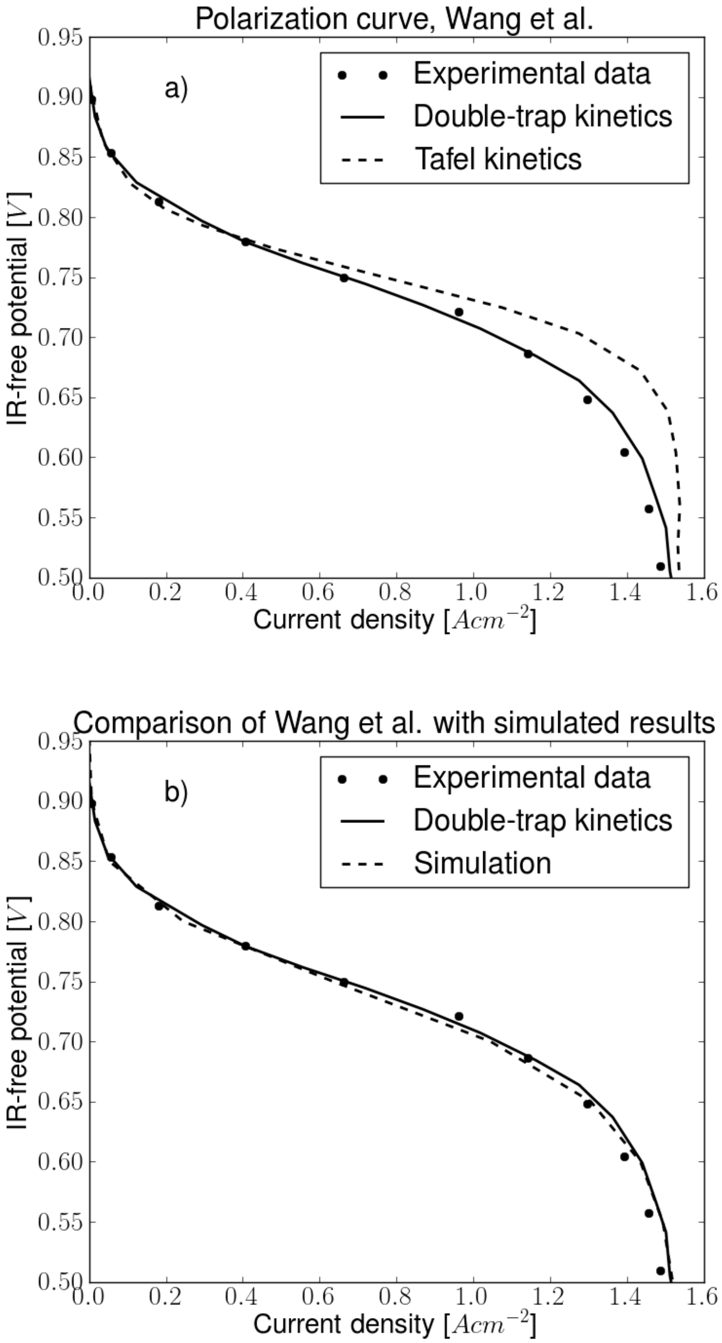

Figure 2.2: a) Polarization curve recreated from reference [48] showing the effect of using the double-trap kinetic model as compared to the Tafel kinetic model. b) Comparison of the polarization curve presented by Wang et al. and that computed using the model implemented in the FCST code.

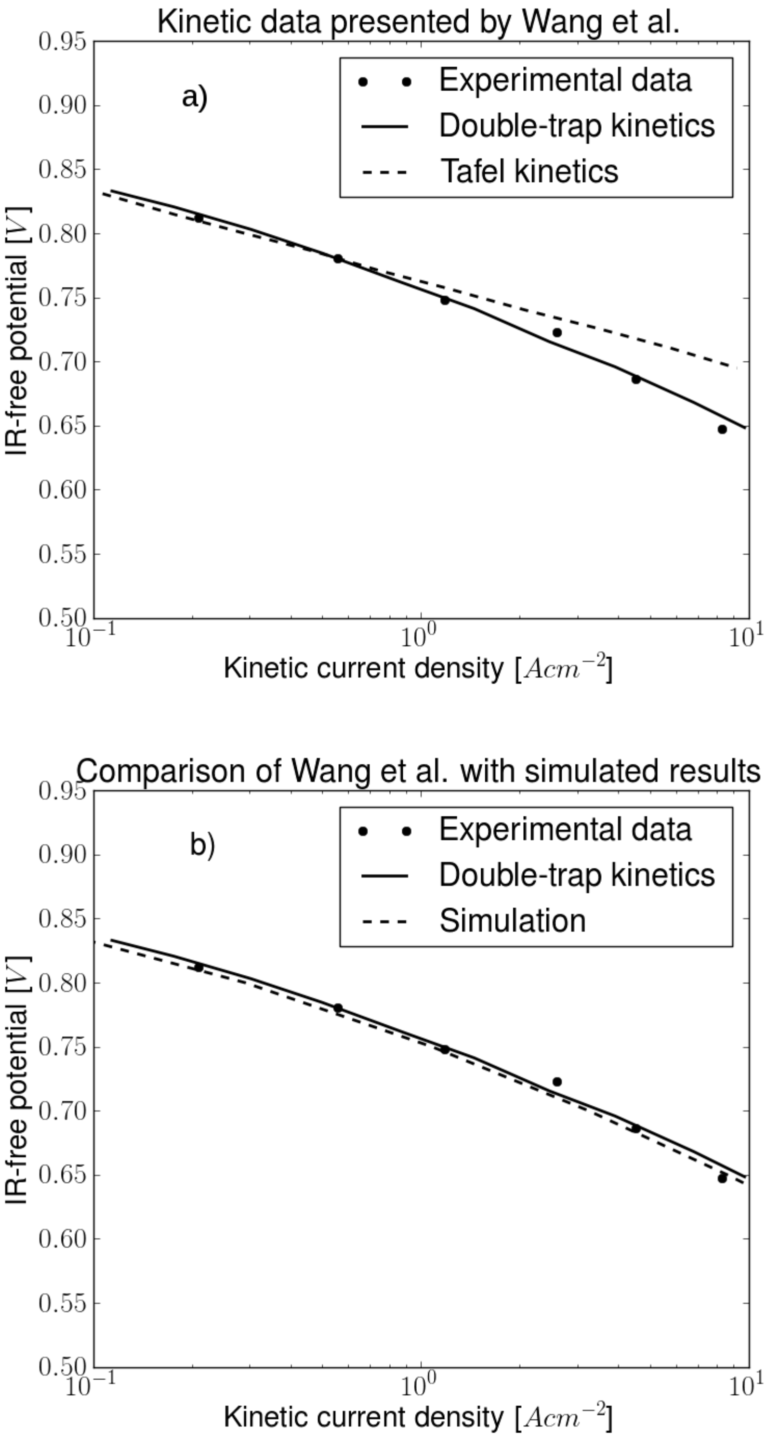

Figure 2.3: a) Kinetic data recreated from reference [48] where the kinetic current is plotted on a log scale. b) Comparison of the kinetic presented by Wang et al. and that computed using the model implemented in the FCST code.

In addition, Figure 2.2(b) also shows the results from the simulation of the kinetic model using the FCST code. This was done to ensure that the model was correctly implemented. The close agreement between the kinetic model as presented by Wang et al. and that from the FCST code shows that the model is working properly.

Figure 2.3(a) shows the case for removing the losses due to mass transport effects, i.e. equation (2.51) is used in post-processing. Note that the Tafel kinetic model shows a constant slope, computed assuming a transfer coefficient of one, as is commonly done in fuel cell modeling. It fails to match the experimental data which incurs additional kinetic losses. The double-trap is able to follow this trend due to the change in slope. Figure 2.3(b) shows a comparison of Wang's results and the results from the FCST code, which matches the trend. The small difference is due to numerical error from extracting the data from the figures presented in the original work. The results presented above are for purely kinetic losses, hence there are no mass transport or ohmic losses. In particular, the ratio of $c_{O_2}/c_{O_2}^{ref}$ will be one for this case, which leads to the model presented by the original authors.

2.3.2 Comparison with Experimental Data

The main feature of this model is that it can capture the change in the Tafel slope that is evident in experimental data. Wang et al. present little experimental data in their work, so this section will compare the model to data presented by Parthasarathy et al. [31, 32]. These papers present kinetic data obtained using a solid state micro-electrode, as discussed in section 1.3.1. This data was chosen as it shows the change in Tafel slope from a lower slope of approximately $60mV/dec$ to an upper slope of approximately $120mV/dec$. Further, the kinetic data was presented over a range of operating conditions making it ideal for parameter estimation, and was obtained using a solid state micro-electrode. This experimental setup better represents the ORR kinetics in a fuel cell in comparison to RDE experiments, as a solid Nafion membrane is used instead of a liquid electrolyte. This approach has also been used to obtain kinetic parameters by [21, 22, 33, 34]. The data from Parthasarathy et al. is also widely cited by researchers in the area of fuel cell modeling, as the authors reported several kinetic parameters, such as the exchange current density or oxygen reaction order. These parameters are then used by researchers in the area of fuel cell modeling to predict the produced current using the Tafel equation . In Chapter 3, a comparison between this commonly used method and using the double-trap kinetic model will be presented. Kinetic data for a number of different temperatures and cell pressures in Figures 2.4(a) and 2.4(b), for both the experimental and numerical data.

Neither plot shows very good agreement between the numerical and experimental data, most likely due to the difficulties in trying to capture an experimental process numerically. However, the change in Tafel slope is apparent, in both data sets. The change from one slope to another happens very suddenly in the experimental data, whereas the kinetic model predicts a much smoother transition. This gradual change in slope is evident in other experimental data, for example that presented by Holdcroft et al. [22, 33]. Of particular interest is the location of the change in slope and the values of each Tafel slope.

For the experimental data, the potential at which the change in Tafel slope is observed (i.e. the 'changeover potential') is different for the temperature and pressure studies, whereas the kinetic model has the same changeover potential. The experimental data shows a changeover potential at approximately 0.75V and 0.85V for the temperature study and pressure study respectively. The kinetic model changeover potential appears to lie between the two values shown in the experimental data, at approximately 0.8V.

The experimentally and numerically obtained Tafel slopes are presented in Tables 2.2(a) and 2.2(b). The numerical Tafel slopes were obtained by plotting the cell potential against the log of the current density. A linear trend-line was inserted in the lcd region over four or five data points, from a potential equal to the equilibrium potential up to 0.1V above changeover potential. Similarly, the hcd Tafel slope was obtained by inserting a trend-line that started from a cell potential at 0.1V below the changeover potential to the lowest potential. A gap of 0.2V was maintained around the changeover potential to ensure that only the linear region was captured. The slope of the inserted trend-lines was equal to the Tafel slopes. The experimental Tafel slopes used were reported by Parthasarathy et al.

The experimental data shows a lot of variability in the Tafel slopes, most likely due to the difficulties in obtaining kinetic data experimentally. Both the temperature and pressure studies show increasing lower Tafel slopes for increasing temperature and pressure, which is reproduced by the kinetic model in the temperature dependent case but not for the pressure case. The values for the numerically obtained slopes are consistently lower than the experimentally obtained slopes by

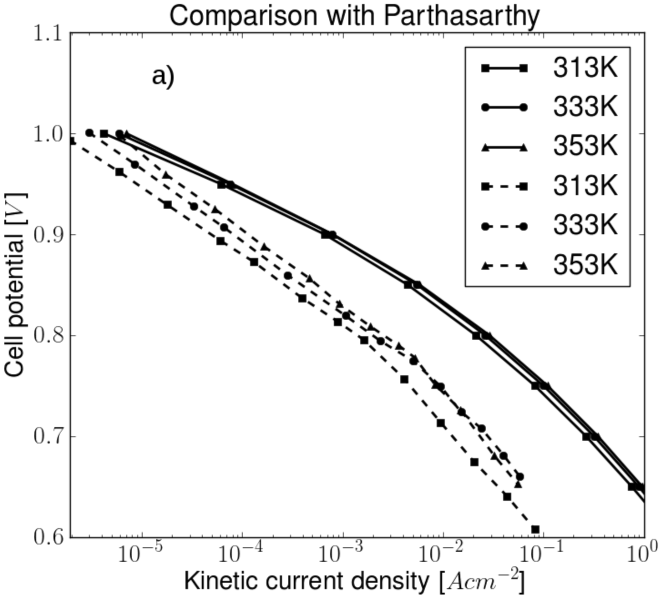

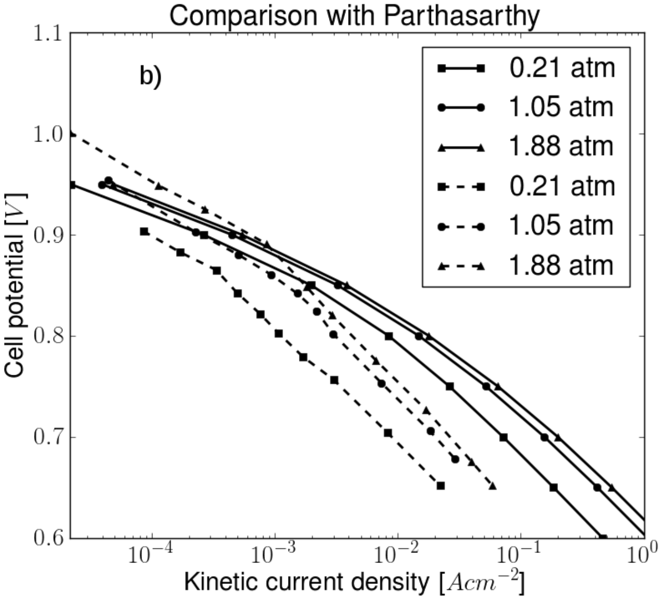

Figure 2.4: Kinetic data for a) different cell temperatures at a constant oxygen partial pressure of 5 atm and b) different cell pressures at a constant cell temperature of 50°C. The dashed lines are the kinetic data presented by Parthasarathy [32], while the solid lines are the data computed using the double-trap kinetic model.

Table 2.2: Comparison between experimentally and numerically obtained Tafel slopes for varying: a) temperatures (left) and b) pressures (right).

Temp. [K]	Experimental [mV/dec]	Numerical [mV/dec]
313	-67.6	-54.4
	-113.86	-121.4
323	-68.33	-54.3
	-119.53	-124.6
333	-69.35	-54.1
	-110.49	-127.7
343	-71.24	-53.9
	-113.76	-130.5
353	-76.22	-53.8
	-115.89	-133.0

Press. [atm]	Experimental [mV/dec]	Numerical [mV/dec]
0.21	-64.8	-49.9
	-121.2	-123.1
0.56	-68.9	-51.1
	-111.1	-123.6
1.05	-69.9	-51.9
	-125.1	-123.9
1.46	-71.9	-52.4
	-143.2	-124.1
1.88	-69.5	-52.8
	-138.7	-124.2

15-20mV/dec in the lcd region. For the upper Tafel slope, the large variability in the slopes makes generalization difficult, however the kinetic model consistently returns a value between 120-130mV/dec, which is the commonly assumed value. However, the highest current predicted by the numerical model is almost an order of magnitude higher than that of the experimental data. This effect is a result of the underprediction of the lcd Tafel slope, which leads to large errors in the hcd region.

The parametric study on the cell temperature for experimental and simulated data show individual I-V curves (current-voltage curves) that are quite close together. The kinetic model underpredicts the spread of the data due to the changing temperature, this may be due to the temperature causing other effects in the experiment that are not captured in the kinetic model.

The Tafel slope b is computed according to equation (1.28). This equation can be rearranged to find the transfer coefficient, α:

$$\alpha = \frac{-2.303RT}{bF} \tag{2.52}$$

where the apparent transfer coefficient α is used instead of the symmetry factor β, as the ORR is a multi-step reaction. Comparison of the transfer coefficients for the numerical and experimental data can give a insight into whether the temperature dependence of the ORR has been correctly predicted. For the experimental data, Parthasarathy et al. argue that the lower Tafel slope increases monotonically with temperature, meaning that the transfer coefficient is independent of temperature. For the numerical data, there is a consistent decrease, however it is very minor, so the slope can be considered constant. Because the temperature is changing, the transfer coefficient must also change to maintain the constant Tafel slope (see equation (2.52)). Similarly, the upper Tafel slope for Parthasarathy was considered constant, leading to a non-constant transfer coefficient. The kinetic model predicts a constant increase in Tafel slope, so the transfer coefficient is considered constant. The transfer coefficient was found to be one in the lower Tafel slope region for the experimental data, while the model predicts a range of 1.14 to 1.30. For the upper Tafel slope, Parthasarathy found a transfer coefficient ranging from 0.5 to 0.6, while the model predicts a constant value of approximately 0.51. The results are in reasonable agreement, so the trends with changing temperature can be considered to be captured by the kinetic model.

For the pressure dependent case, the main difference between the simulated and experimental plots is the spread of the I-V curves. Both show the I-V curves for the two highest pressures bunching together, compared to the lowest pressure curve. However, the difference in performance between the lowest and highest pressure is clearly greater for the experimental case. This spread can be characterized by the reaction order with respect to oxygen. The mass transport corrected Tafel equation is given by:

$$i = i_0 \left(\frac{p_{O_2}}{P_{O_2}^{ref}} \right)^{\gamma} e^{-\alpha F(E-E_{eq})/RT} \tag{2.53}$$

where p_{O_2} is the partial pressure of oxygen (note that concentration was used in Chapter 1, however they are related via the ideal gas law). γ is the reaction order with respect to oxygen. At a constant overpotential and temperature, equation (2.53) can be rewritten to give:

$$log(i) = log(C) + \gamma log(P_{O_2}) \tag{2.54}$$

where C accounts for all constants, i.e. the exponential term and the exchange current density. Plotting this equation will result in a linear profile, with a slope equal to the reaction order. An example of the linear profile is shown in Figure 2.5 for the experimental data only. The figure plots the current densities obtained at a constant overpotential of 0.5V (i.e. using the Nernst equation to account for the changing equilibrium potential) for the five oxygen partial pressures used in Table 2.2. The slope of the linear trend-line approximating the data points is equal to the oxygen reaction order at that overpotential. The Pearson correlation coefficient (commonly known as the R value) gives an indication of the strength of

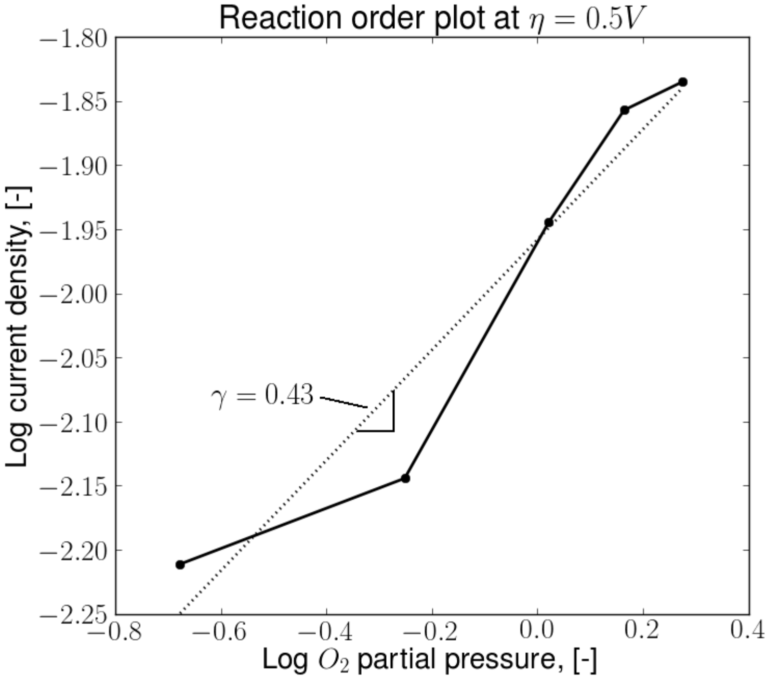

Figure 2.5: Example reaction order plot from the experimental data presented by Parthasarathy et al. [31]. The points are the experimental data points from the five pressure I-V curves. The dashed line shows the linear trend-line approximating the data points.

the correlation between the two variables. For the case shown in Figure 2.5, this value was at 0.92. Over the overpotential range for the experimental data shown in Figure 2.6, the R-value ranged from 0.86-0.96 where a value of 1 indicates a perfect fit. The deviation from 1 shown in the experimental data is likely due to a combination of experimental error and error occurring from extracting data from a journal article. The same method was used for the numerical data.

Figure 2.6 plots the reaction order obtained by this method for the kinetic model over a range of overpotentials at a constant temperature. The kinetic model unable to compute the reaction order at or close to zero overpotential. This was likely due to the very small current densities being computed, with values in the order of 1×10^{-12} being returned. Machine accuracy is at 1×10^{-16} which may impact on the results. Parthasarathy et al. obtained the reaction order at zero overpotential only, by extrapolating the I-V curves in the Tafel plots back to the equilibrium potential (and therefore finding the exchange current density). A similar extrapolation of the curve in Figure 2.6 to zero overpotential indicates that the model is returning

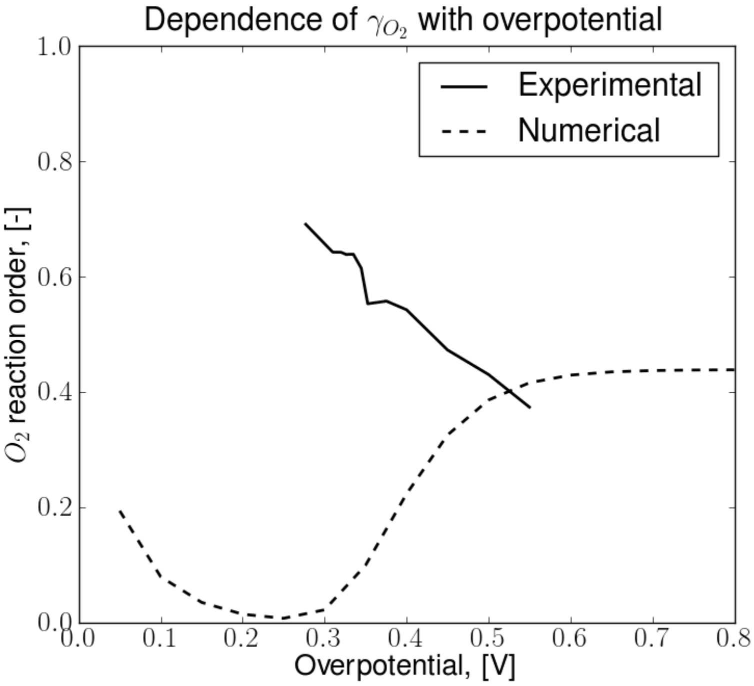

Figure 2.6: Variation of the oxygen reaction order with changing overpotential for the kinetic model (dashed line) and experimental data from Parthasarathy et al. [31] (solid line).

a value between 0.15 to 0.2. The reaction order reported by Parthasarathy et al. is one, obtained by extrapolating both the upper and lower Tafel slopes back to the equilibrium potential. The kinetic model therefore shows a significant deviation from the experimental data. This value is in agreement with data from Beattie [22] and Zhang [34]. More recent research into ORR kinetics by Neyerlin et al. [63] predicts a value of 0.54 for the reaction order, which is in better agreement with the kinetic model, however there is still significant error.

The numerical results obtained by the kinetic model show large variability in the reaction order, in particular at an overpotential of 0.2V to 0.3V where the reaction order is close to zero. Given that the equilibrium potential of the simulation is at approximately 1.2V, this reaction order exists at a cell potential of 0.9V to 1.0V. The effect of such a low reaction order can be seen in the lcd region in Figure 2.4(b) where the numerically obtained pressure curves are closer together than is seen in the hcd region. At lower potentials, or higher overpotentials, the reaction order rises to close to 0.45. This value is similar to that shown by Neyerlin et al. at zero overpotential, however the kinetic data shows that the reaction order changes with increasing overpotential so comparing the value at different overpotentials is not recommended. Neither Neyerlin nor Parthasarathy et al. report the reaction order with changing overpotential, Figure 2.6 was obtained by extracting data from the I-V curves in Figure 2.4(b). There was insufficient data to determine whether a steady state value is obtained. There will be some error in Figure 2.6, as the equilibrium potential for the I-V curves was not reported and the current densities had to be extracted from the Tafel plot taken from the article. However, extrapolating the data back to zero overpotential returns the reported value of unity. The experimental data shows a linear decrease in reaction order with increasing overpotential, such that there is closer agreement between the experimental and numerical value at hcd. Figure 2.4(b) also illustrates that choosing a single reaction order to characterize the entire overpotential range can induce significant errors, for the same reasons as choosing only a single Tafel slope.

The comparison with experimental data shows that the kinetic model can predict a change of slope at the correct cell potential, with Tafel slopes reasonably close to the expected values. However, closer inspection of the results from the kinetic model shows that key characteristics of the ORR kinetics are not captured, in particular the oxygen reaction order. These results were obtained by analyzing the model using parameters presented by Wang et al. In section 2.4, parameter estimation is used to fit the kinetic model to the data presented by Parthasarathy which should increase the accuracy of the model.

2.3.3 Analysis of Model

A key component of this model is the computation of the coverage of the intermediate species. The change in Tafel slope is attributed to the change from a high coverage of the intermediates to a low coverage, as was discussed in Chapter 1. Figure 2.7 shows the computed coverages of the OH_{ads} and O_{ads} species as well as the total coverage. The profiles show the high total coverage of the two species at low overpotentials and low total coverage at high overpotentials. The individual profiles shows the dominance of the O_{ads} species at low overpotentials, which decreases rapidly with increasing overpotential. The OH_{ads} species is initially at negligible coverage, however rises to a constant value of approximately 26% with increasing overpotential. The change-over from a mostly covered, to an oxide-free reaction surface occurs between overpotentials of 0.3V and 0.5V, corresponding to a cell

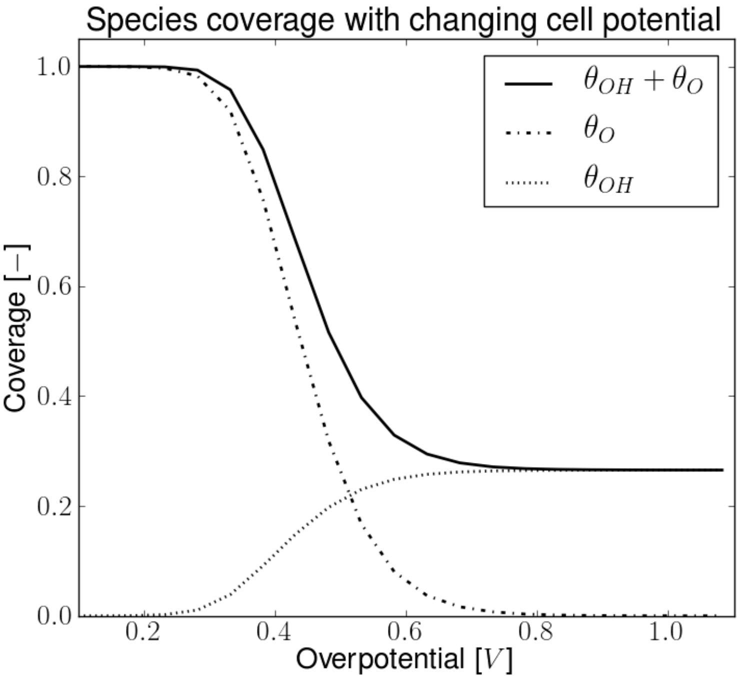

Figure 2.7: Coverage of the OH_{ads} and O_{ads} species as well as the addition of the two coverages.

potential of 0.6V and 0.8V. These values match with the potential at which the Tafel slope change occurs as is seen in the literature [22, 31–34].

The change in the dominant species is indicative of a change in the dominant mechanism of the ORR as predicted by the double-trap model. With the change in potential, the energy barriers as described in equations (2.39)-(2.42) will change, resulting in a change in the relative dominance of each of the reactions. The change in the energy barriers with cell overpotential is shown in Figure 2.8. For the initial adsorption of oxygen to the reaction site, the DA reaction dominates at low overpotentials, as the RA reaction has a higher energy activation barrier at low overpotentials. This dominance results in the higher production of the O_{ads} intermediate in comparison to OH_{ads}. Unlike the DA reaction, the RA reaction is an electrochemical reaction so the energy barrier decreases with increasing potential. At high overpotentials, the RA reaction is dominant, leading to a higher coverages of the OH_{ads} intermediate.

The high coverage of the O_{ads} species can also be attributed to the RT reaction. In particular, the backward step for this reaction is dominant over the forward reaction at low overpotentials. The RT reaction proceeds by reacting with an O_{ads}

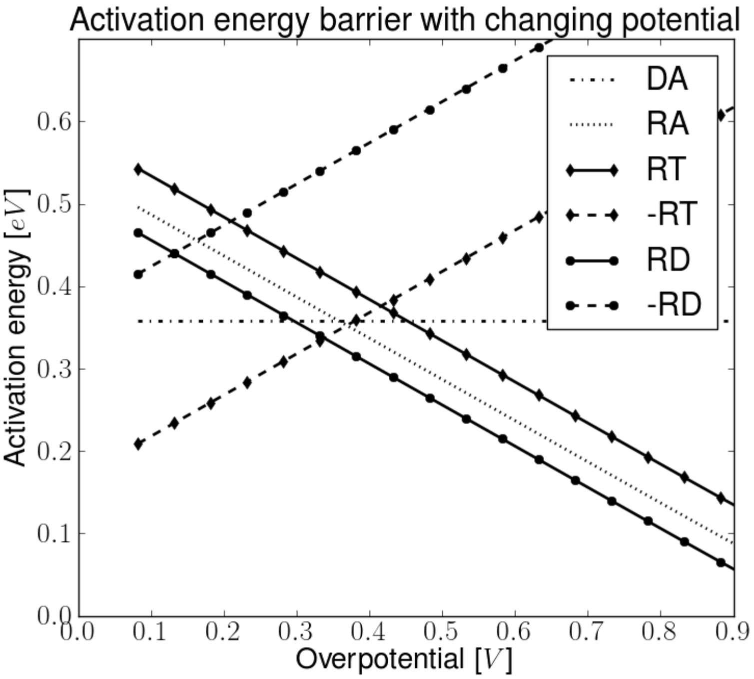

Figure 2.8: Potential dependent activation energy barriers for each of the four reactions for the forward and backward reaction. Note that the backward rates for the DA and RA reactions have been omitted.

molecule on the reaction surface, forming OH_{ads}. Therefore the backward reaction will react OH_{ads} to form O_{ads}, further reducing the OH_{ads} coverage and increasing the O_{ads} coverage. The change in the coverage of the intermediates is most pronounced around an overpotential of 0.4V, due to a change in dominance from: i) the DA to the RA reaction and ii) the backward RT reaction to forward RT reaction, as is shown in Figure 2.8. This change in dominance leads to the change coverage conditions and to a change in the Tafel slopes produced by the model.

In Figure 2.8, the backward reactions for the DA and RA were omitted. This was due to the high energy barriers for these reactions, making the reaction rates insignificant compared to the other reactions. This predicts that the absorbed species will not react to form oxygen at any potential. The backward RD reaction (dashed black), which would cause water to react to form the OH_{ads} intermediate, is initially smaller than the forward reaction. However, the reaction quickly increases and becomes insignificant even at very low overpotentials.

In Figure 2.9(a) and 2.9(b) the two potential paths of the ORR are plotted. The relevant dominance of each reaction can be seen by looking at the distance in

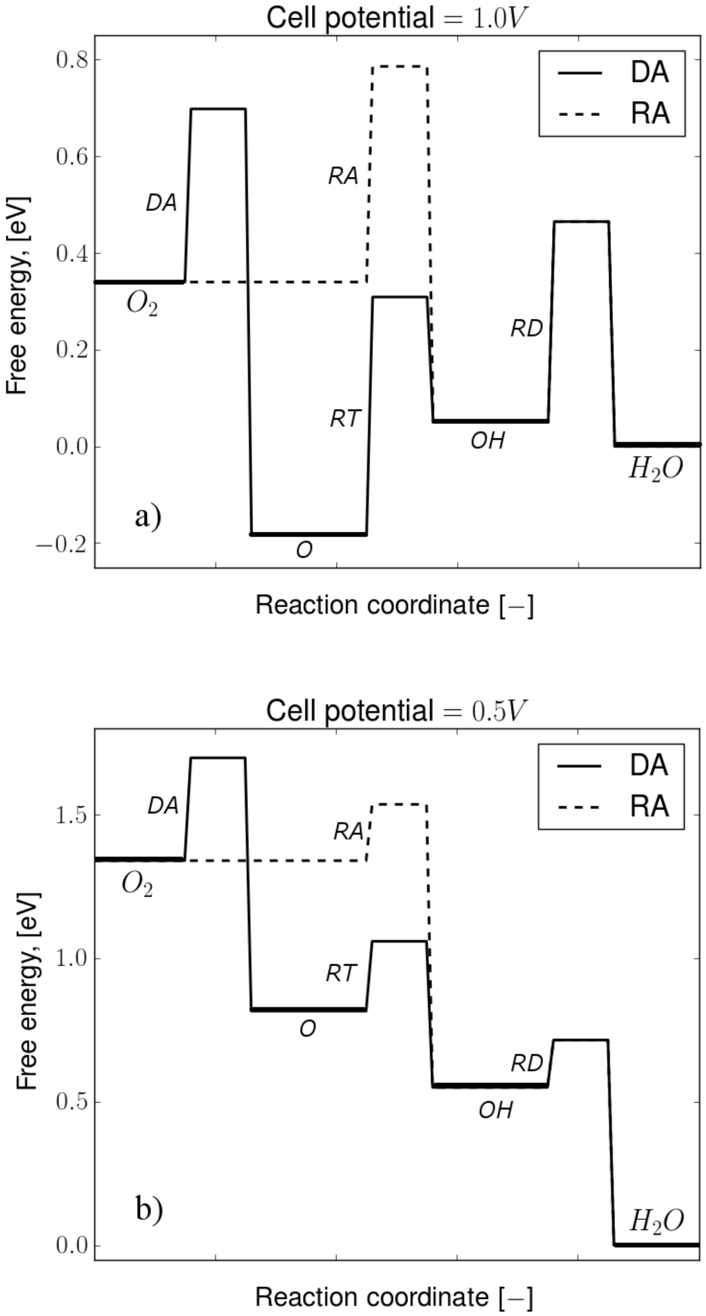

Figure 2.9: Reaction coordinate plot at a) a cell potential of $1.0V$ corresponding to the upper Tafel slope region, and b) a cell potential of $0.5V$ corresponding to the lower Tafel slope region. Note that both paths overlap for the RD reaction. The solid line denotes the path whereby the oxygen first desorbs onto the platinum as a O_{ads} species, while the dashed line denotes the case where OH_{ads} is formed first.

the y-direction between each stable species. Each of the peaks corresponds to a reaction: reading from left to right, the height of each peak denotes the forward energy of activation for the reaction. Reading from right to left, each peak height is the activation energy of the backward reaction. Note that water takes an energy of formation value of zero and all other species are measured relative to this. Oxygen also has an energy of formation of zero, however the oxygen is reacting with the hydrogen ions and electrons which will change its position on the figure. The absolute values are not of particular interest here however, the relative differences are of more importance.

The main difference between the two plots is the relative difference between the reactant of the ORR, O_2, on the left of each figure and the product, H_2O, on the right of each figure. It is clear that increasing the overpotential increases the distance between the positions of the two species (note the change in range on the y-axis between the figures). Figure 2.9(a) and 2.9(b) also shows the change in the positions of the adsorption energies of the intermediate species. The reason for high coverage of the O_{ads} species at low overpotentials is immediately apparent as it occupies the lowest energy configuration in Figure 2.9(a). Again the DA step shows a smaller energy barrier than the RA reaction, so O_{ads} is more likely to be formed. Any OH_{ads} that is formed is more likely to undergo a transition to O_{ads} via the backward RT reaction than complete the reaction and form H_2O. This is due to the greater energy barrier for the forward RD reaction compared to the backward RT reaction. It is clear that the low energy configuration of the O_{ads} species forms a 'hole' that is difficult to escape from, leading to high O_{ads} coverage.

Figure 2.9(b) shows the case for a higher overpotential. Now all the forward reactions are dominant compared to the backward reactions, leading to the greater relative distance between reactant and product. Most importantly, the OH_{ads} now has a lower energy configuration than the O_{ads} species, so the 'hole' in Figure 2.9(a) is not there. Indeed, the RA reaction is now more favorable than the DA reaction, so the O_{ads} is being produced in smaller quantities.

2.4 Fitting of Kinetic Parameters

2.4.1 Introduction

Figures 2.4(a) and 2.4(b) show significant differences between the experimental data presented by Parthasarathy et al. and the kinetic current computed by the double trap model. In particular, the maximum predicted current is an order of magnitude higher for the numerical data compared to the experimental data. Further, significant differences are observed in the Tafel slopes predicted by the double trap model. Tables 2.2(a) and 2.2(b) show Tafel slopes for experimental and numerical data, the numerical Tafel slopes in the lcd region in particular are significantly lower than those observed experimentally. The reaction order with respect to oxygen also shows significant errors. The experimental data shows a reaction order of unity, while Figure 2.6 shows that the double trap model does not match this value, with a predicted value of 0.2. Also, the high coverage at high overpotentials is not in agreement with the upper Tafel slope occurring on a clean platinum surface, for example as is presented by Subramanian et al. [11].

The performance of the model is dictated by the free energies of adsorption of the intermediate species and the free energies of activation of the four intermediate steps. The results in the previous section were obtained using values presented by the original authors, and significant errors are found when comparing the numerical data to experimental data. This section will attempt to improve the accuracy of the model by fitting the kinetic model to the experimental data presented by Parthasarathy et al.

In this work, the free energies on which the model is based will be termed the 'kinetic parameters'. Their values are not known as they are very difficult to determine experimentally. Theoretical investigation of these parameters is only possible using methods like DFT. Such methods are still in their infancy so they can not yet consistently predict such values, as discussed in section 1.3.1.3. Ideally the values for the kinetic parameters would be found theoretically or experimentally, however as this is not possible, parameter estimation will be used instead.

Parameter estimation can be used to determine unknown model parameters by comparing results from the model to experimental data. The numerical data can be adjusted to better fit the experimental data by systematically varying the unknown parameters. In the case of the double trap kinetic model, the current produced by the model is compared to the experimental current density presented by Parthasarathy et al. The functional minimized will be the normalized least-square difference between the numerical and experimental current density produced in the solid state cell. If a good fit to the data can be found, then the kinetic parameters such as the reaction order and Tafel slope should also match. The kinetic model is highly nonlinear in terms of the kinetic parameters, so a nonlinear optimization method will be used. The optimization methods are provided by an open source library developed in Sandia National Laboratory called the DAKOTA (Design Analysis Kit for Optimization and Terascale Applications) toolkit [67]. The FCST code has been coupled to this library, such that the FCST code behaves as an analysis package. The coupling allows the Dakota library to modify variables in FCST (e.g. the kinetic parameters) and read in the results from FCST (e.g. the current density). The coupling of Dakota and FCST is described in greater detail in references [68] and [69].

2.4.2 Least-Square Parameter Estimation Problem Formulation

The least square parameter estimation problem is defined as:

$$\text{Minimize } f(\bar{\boldsymbol{x}}) = \frac{1}{2}\sum_{i=1}^{N}\left[\frac{j_i^{exp} - j_i^{model}(\bar{\boldsymbol{x}})}{j_i^{exp}}\right]^2 \tag{2.55}$$

$$\text{w.r.t.:} \quad \bar{\boldsymbol{x}} = \Delta G_{OH}^{0}, \Delta G_{O}^{0}, \Delta G_{DA}^{*0}, \Delta G_{RA}^{*0}, \Delta G_{RT}^{*0}, \Delta G_{RD}^{*0} \tag{2.56}$$

$$\text{s.t.:} \quad -0.8 < \Delta G_{m}^{0} < -0.1 \tag{2.57}$$

$$0.1 < \Delta G_{n}^{*0} < 0.8 \tag{2.58}$$

$$0.8 < (\theta_{OH}(0.85V) + \theta_{O}(0.85V)) < 1.0 \tag{2.59}$$

$$0.0 < (\theta_{OH}(0.4V) + \theta_{O}(0.4V)) < 0.2 \tag{2.60}$$

In equation (2.55), $f(\bar{\boldsymbol{x}})$ is the objective function to be minimized. N is the number of experimental data points taken from the experimental data curves. For each curve (where a curve corresponds to a particular set of operation conditions, over a range of potentials), eight data points were taken. Four data points were taken in the lcd region and four data points were taken in the hcd region to ensure that one Tafel slope region was not favored over the other. The experimental current is given over several orders of magnitude, so the difference between the experimental and numerical data are weighted to ensure that data in the lcd region (which will be orders of magnitude smaller than the current in the hcd region) are given equal importance. The final objective function, $f(\bar{\boldsymbol{x}})$, is the root mean square of the data set.

In equation (2.55), the objective function is a function of the design variables $\bar{\boldsymbol{x}}$ (due to the dependence of j_i^{model} on $\bar{\boldsymbol{x}}$). These are the parameters to be varied. These variables are the free energies of activation of the intermediate species and of adsorption of the intermediate species, as is shown in equation (2.56).

Equations (2.57) and (2.58) show the bounds for the free energies of adsorption and activation respectively. m is the number of absorbed species (two in this work) and n is the number of intermediate reactions (four in this work). Keith et al. [41] presents a review of density functional theory calculations of the binding energy of oxygen to a platinum crystal. The results range from $0.1eV$ to $1.95eV$ depending on the assumptions of the model. The lower bound is set to $0.1eV$ in agreement with the range found by Keith et al. This also prevented the free energy reaching a value of zero, which was found to make the optimization unstable. The upper bound was set to $0.8eV$ instead of $1.95eV$ based on the results of a sensitivity analysis. The kinetic parameters were varied over a wide range to see which parameters had an effect on the produced current and the coverage of the intermediate species. An example of this sensitivity analysis is shown in Figures 2.10 a) and 2.10 b). The analysis shows that for high values for the activation energies, there is no change in the values of the current or coverages. For example, the current is unaffected if the DA activation energy is changed from $0.6eV$ to $0.8eV$. The gradient returned to the optimization software at this point will be close to zero, which can make it difficult to move the design variables such that the residual is minimized. The upper bound was restricted to $0.8eV$ so as to exclude most of these 'flat' regions. Some of the flat region was still included however, as these regions may shift slightly with the changing design variables. A similar sensitivity analysis for the absorption energies was performed and bounds of $-0.8eV$ to $-0.1eV$ were chosen.

The final part of the optimization formulation are two non-linear constraints. Matching the experimental data presented by Parthasarathy et al. should result in the model returning the correct Tafel slopes and other kinetic characteristics such as the oxygen reaction order. The coverages returned by the kinetic model should also match commonly observed trends, i.e. high coverage at low overpotentials and low coverage at high overpotentials. Parthasarathy et al. do not present experimental data that can be matched in the same way as the current, so two general constraints are added, i.e. equations (2.59) and (2.60). Equation (2.59) imposes that at low overpotentials, the total coverage returned by the kinetic model is greater than 80%.

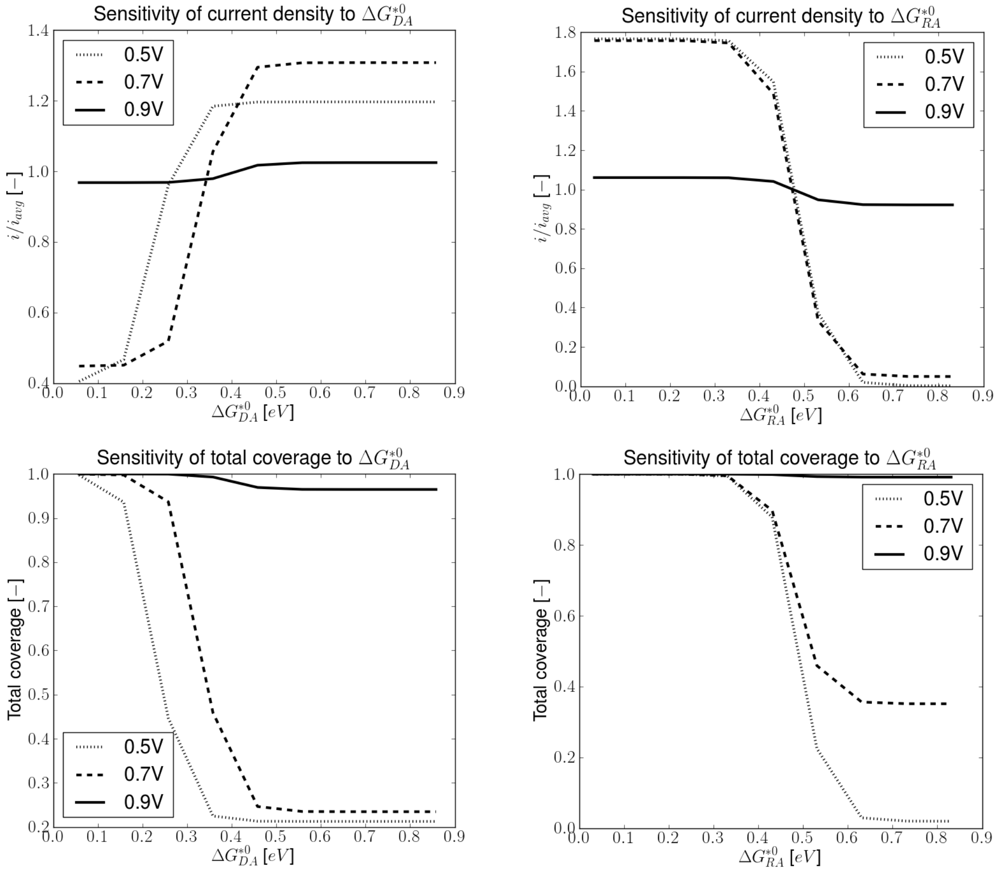

Figure 2.10: Sensitivity of the current density and total coverage as predicted by the double trap model to a) the free energy of activation of the DA reaction (left) and b) the RA reaction (right). This is done for a constant cell potentials of $0.5V$ (high overpotential), $0.7V$ and $0.9V$ (low overpotential). Note that current density plots are normalized by the average value of the current produced over all values for the design variable.

At high overpotentials, equation (2.59) imposes that the total coverage has to be lower than 20%. When first attempting the data fitting, the values at which the constraints were evaluated were varied in order to find the value that gave the lowest residual with a coverage profile that matches profiles seen in the literature. It was found that the high overpotential constraint was not significant as the coverages at high overpotential tended to be very close to zero. The optimizer also tended to return coverages that were very close to the low overpotential constraint. The potential at which this constraint was evaluated at was varied and it was found that using a cell potential of $0.85V$ gave the lowest residual with a coverage profile very similar to that produced by Subramanian et al. [11] (see Figure 2.14).

2.4.3 Solution Procedure

An interior-point, gradient-based nonlinear optimization method is used to solve the problem. The method, known as OPT++ [70], can be used for non-linear constrained optimization. The main reason for choosing this method was its quick convergence and its ability to apply non-linear constrains to the problem. One of the main weakness of this model is that it is a local model, i.e. it will find the closest minimum in the variable space. In order to guarantee that a global minimum is obtained, in this work numerous starting points are used and the results from the simulation that return the lowest residual are used. Gradients are required for this method, so numerical derivatives computed using central differencing are used, with a relative step size of 1×10^{-3}, or 0.1%. Implementing the analytical derivatives would be time consuming, and as an individual function evaluation typically takes in the order of half a second, the extra function evaluations needed to compute the derivatives are not computationally expensive.

2.4.4 Results

A number of experimental kinetic data curves from Parthasarathy et al. were chosen as the input data. Ideally, several curves would be chosen with varying pressures and temperatures, so that changing pressure and temperature trends could be captured. However, inspection of the two sets of data show that the data reported by Parthasarathy et al. in the temperature study does not match the data in the pressure study. In particular, the open cell potential and the potential at which the change in Tafel slope occurs is not consistent between the two sets of data (accounting for the changing operating conditions). Therefore, the temperature plots were not used in the parameter fitting as inconsistent data will result in the non-convergence of the optimization simulations. The data in the pressure study was chosen, as it was 'cleaner' than that of the temperature study (i.e. it was easier to extract the data points). The pressure dependence was also considered to be more important than the temperature dependence due to the closer agreement of the model with the transfer coefficient than the reaction order as shown in section 2.3.2.

I-V curves at three different pressures were chosen as the experimental data. The I-V curves chosen were for cell pressures of 0.56atm, 1.05atm and 1.88atm. The 1.05atm curve was chosen to be the reference condition for the parameter fitting.

Table 2.3: Starting points for the design variables. The first two are parameters presented by Wang et al., the third are the results from the single curve parameter fitting, while the final two are random starting points.

Case	G^{*0}_{DA}	G^{*0}_{RA}	G^{*0}_{RT}	G^{*0}_{RD}	G^{0}_{O}	G^{0}_{OH}
1	0.358	0.531	0.578	0.5	-0.524	-0.12
2	0.25	0.45	0.5	0.46	-0.47	-0.12
3	0.3598	0.6008	0.5846	0.562	-0.66	-0.3948
4	0.1424	0.6967	0.6237	0.5301	-0.3417	-0.3917
5	0.3467	0.3402	0.4780	0.4990	-0.1230	-0.1321

The curve will provide the reference oxygen concentration for the parameter fitting, which would be the oxygen concentration provided at an oxygen partial pressure of 1.05atm. As a result of this, the fraction $c_{O_2}/c^{ref}_{O_2}$, shown in equation (2.46), will be equal to one when the oxygen partial pressure is at 1.05atm. The changing equilibrium potential for the changing oxygen partial pressures is also accounted for.

The parameter estimation problem is solved with five starting points in order to ensure that the global minimum is found. The first two sets of starting points used are the free energies provided by Wang et al. Wang obtained the parameters by fitting to experimental current densities found using a fuel cell and an RDE. These are cases one and two respectively. Case three is a data set found from fitting to a single curve only. The model was initially fit to a single curve to test the optimization formulation. While convergence was achieved, the resulting kinetic parameters were not able to capture the trends shown by the experimental data for changing oxygen pressure. Fitting to multiple curves is used to ensure that this trend is captured. Cases four and five are data sets that were generated randomly. Table 2.3 gives the values for the starting points for each of the five cases.

Table 2.4: Optimization results from fitting to multiple pressure curves.

Case	G^{*0}_{DA}	G^{*0}_{RA}	G^{*0}_{RT}	G^{*0}_{RD}	G^{0}_{O}	G^{0}_{OH}	$f(\bar{\boldsymbol{x}})$	$\theta_{T,hcd}$	$\theta_{T,lcd}$
1	0.391	0.609	0.590	0.254	-0.343	-0.376	1.059	0.0005	0.800
2	0.391	0.609	0.590	0.278	-0.343	-0.376	1.059	0.0005	0.800
3	0.391	0.609	0.590	0.273	-0.345	-0.376	1.059	0.0005	0.800
4	0.391	0.609	0.590	0.128	-0.354	-0.376	1.059	0.0005	0.800
5	0.388	0.608	0.379	0.573	-0.208	-0.382	1.136	0.1714	0.804

2.4.4.1 Results from Parameter Estimation

The results from the parameter estimation are given in Table 2.4, where the nonlinear constraints are denoted θ_T. For the first three cases, convergence was achieved, with the optimizer terminating due to the norm of the gradient of the design variables with respect to the objective function being less than the relative gradient tolerance (set to 1×10^{-4}). Three converged cases all returned design variables that are very similar. For these cases, two parameters showed small differences which were restricted to the second significant digit (for the G^{*0}_{RD} parameter). The largest difference between the returned G^{*0}_{RD} parameters is ~8%, which resulted in insignificant differences between the final objective function and constraints. A post sensitivity analysis, such as that shown in Figure 2.17(a) and 2.17(b), was performed. The study shows that the objective function and the constraints were not sensitive to these parameters, so the differences in Table 2.4 area not significant.

Cases four and five did not result in convergence. The fourth case terminated due to many backtracks, which indicates that the simulation is stuck in a location that is not a minimum, but any attempts to move out of it are blocked by the constraints. To move out, the simulation would have to go back on itself (i.e. in the direction of increasing the residual). However, the returned kinetic parameters are very similar to those returned by the converged simulations, with the exception of the G^{*0}_{RD} parameter. Inspection of the G^{*0}_{RD} returned for previous iterations show the optimizer reducing the parameter down from an initial value of $\sim 0.5eV$ to 0.1234eV. From here it tries to raise it again, however it got 'stuck' due to the lcd non-linear constraint and terminated. So this simulation would likely have converged to a similar solution as the first three points. Case five terminated due to too many function evaluations and shows significant differences in the kinetic parameters. These results highlight the sensitivity of the optimization algorithm to the initial solution, therefore either the use of several starting points or the use of a global optimization algorithm such as genetic algorithms is highly recommended.

The final overall residual is 1.059. This cumulative residual is the addition of all of the individual weighted differences between each experimental data point and its corresponding numerical data point. These individual residuals were generally less than 10%, with four points out of the 24 having a value of 30% to 45%. Therefore, there is good agreement between the numerical simulation and the experimental

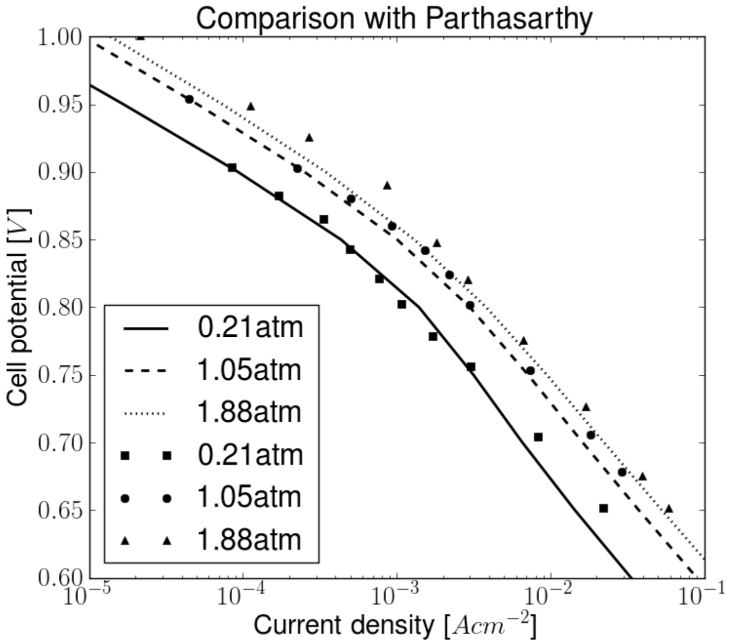

Figure 2.11: Kinetic data for different oxygen partial pressures at a constant cell temperature of 50℃. The points are the experimental data from Parthasarathy et al [31]. The lines represent the simulated data.

data points, barring a small number of errant data points that are likely due to the difficulty in performing solid-state cell experiments. It is also encouraging that none of the returned design parameters are close to their bounds. It shows that the chosen bounds did not interfere significantly with the optimization simulation.

The free energies chosen for this work are those returned by case two. Between the three cases that converged, case one shows the largest difference for the G^{*0}_{RD} parameter, while case three shows the largest difference for the G^0_O parameter.

2.4.4.2 Effect of Oxygen Partial Pressure

Using the results from case two as the input parameters to the kinetic model, the updated kinetic model is compared to the experimental data. Figure 2.11 shows the comparison between the simulated current density and the experimental data for varying oxygen partial pressures. The figure shows that the pressure curves are reproduced accurately. The maximum and minimum current densities are now the same for the simulated and experimental data as appears to be the case for the equilibrium potential.

The experimental data shows an increase in current with increasing oxygen par-

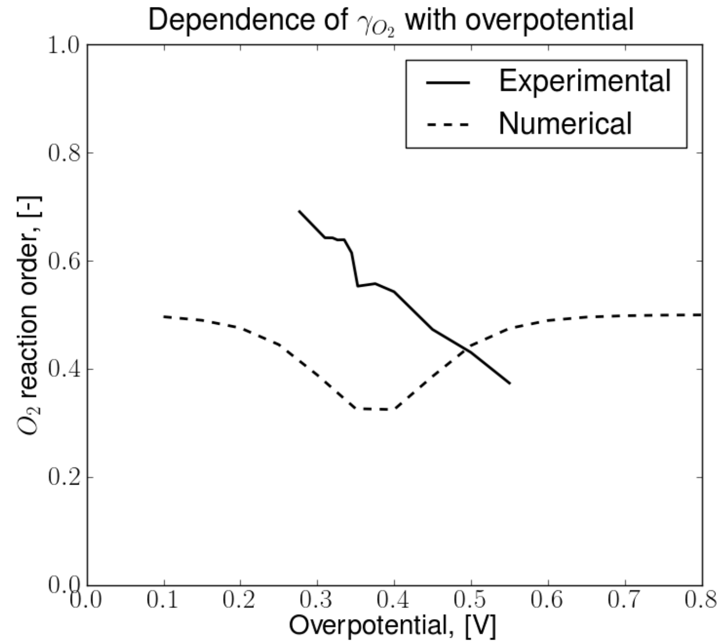

Figure 2.12: Variation of the oxygen reaction order with changing overpotential for the kinetic model (dashed line) using parameters from this work and experimental data from Parthasarathy et al. [31] (solid line).

tial pressure. The simulated data does not exactly reproduce the trend, with the simulated pressure curve at 1.88atm being consistently 'under' the experimental data points, especially in the lcd region. The reaction order with changing overpotential, computed using the same method described in section 2.3.2, is shown in Figure 2.12 for the kinetic model and the experimental data. The simulation was unable to return values close to zero overpotential, however extrapolation of the reaction order plot indicates that the value at zero overpotential is tending towards a value of 0.5. This is a clear improvement over the original parameters, however, it is still smaller than the value of unity found in the experimental data at zero ovepotential. In the hcd region, the experimental reaction order reduces to a value around 0.4 which is closer to the hcd value predicted by the kinetic model. Figure 2.12 shows a significant decrease in the reaction order to approximately 0.33 at an overpotential of 0.3V to 0.4V. As will be shown in Figure 2.14, this value corresponds with the changeover potential at which the local coverage conditions change.

The kinetic parameters were found by fitting to pressure curves only, so the discrepancy in the reaction order at zero overpotential may indicate that the model simply cannot reproduce this reaction order. This could be due to the assumed DA

Table 2.5: Comparison between experimentally and numerically obtained Tafel slopes for varying oxygen partial pressures.

Press. $[atm]$	Experimental $[mV/dec]$	Numerical $[mV/dec]$
0.21	-64.8	-64.4
	-121.2	-137.9
0.56	-68.9	-64.9
	-111.1	-135.1
1.05	-69.9	-65.5
	-125.1	-134.9
1.46	-71.9	-65.9
	-143.2	-131.9
1.88	-69.5	-66.3
	-138.7	-131.1

and RA intermediate steps (equations (2.1) and (2.2)) using one half oxygen stoichiometry. This assumption means that the model does not simulate the cleaving of the oxygen-oxygen double bond. The ORR model used by Ruvinskiy et al. [65, 66] does not make this assumption by adding additional intermediate steps whereby molecular oxygen absorbs to the platinum surface before electrochemically reacting to form the O_{ads} and OH_{ads} intermediates. Adding these additional intermediate reactions may improve the accuracy of the model and return a reaction order of unity. However, the reaction order predicted by the kinetic model appears to be in reasonable agreement with the experimental data at hcd. Further, a zero overpotential reaction order of 0.54 was experimentally obtained by other researchers such as Neyerlin et al. [63], which closely matches with the value obtained in this work. Therefore, the reaction order of 0.5 at zero overpotential may not be an error. Unfortunately, neither Neyerlin or Parthasarathy report the reaction order at other overpotentials so it is difficult to directly compare the experimental and numerical data with confidence.

The Tafel slopes returned by this model are shown in Table 2.5 and show good agreement with the experimentally found Tafel slopes. In particular, the lower Tafel slopes show better agreement than those found using the parameters presented by Wang et al. The upper Tafel slopes show some deviation from the experimental data. The general trend for the experimental data is for increasing Tafel slope with increasing oxygen pressure, the opposite is found with the kinetic model. This trend results in Tafel slopes being greater than the experimentally found slopes for low

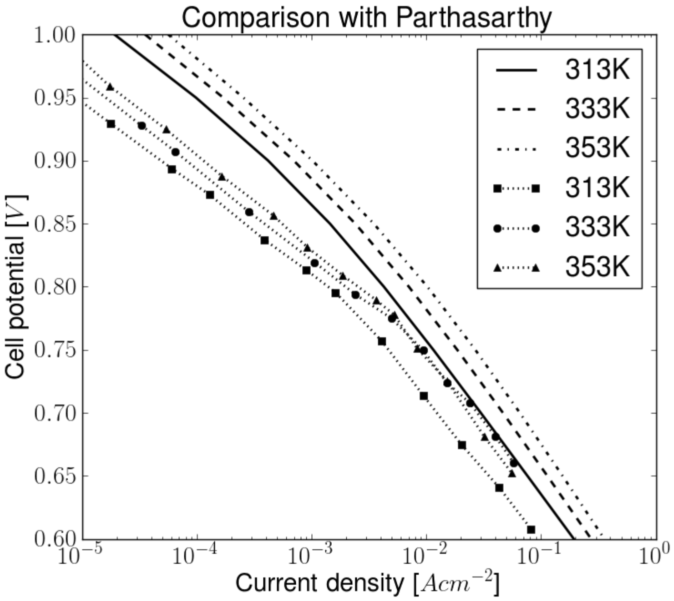

Figure 2.13: Kinetic data for different cell temperatures at a constant oxygen partial pressure of 5atm. The points are the experimental data from Parthasarathy et al [32]. The lines represent the simulated data.

oxygen pressures, which are also the oxygen pressures that are modeled in Chapter 3 and compared with experimental data. The kinetic model will therefore slightly overpredict the kinetic losses in the hcd region.

2.4.4.3 Effect of Cell Temperature

Polarization curves at different temperatures obtained experimentally and numerically, are shown in Figure 2.13. The comparison between the experimental and numerical data show significant errors. However, it is important to note that the experimental data for the pressure and temperature studies, reported in different articles by the same authors [31] and [32], are inconsistent. Therefore, only the trend with temperature is of interest. Further, the temperature dependent I-V curves were not used to estimate parameters.

The main difference is the changeover potential from one Tafel slope region to the other. The simulated results show a change over point at a cell potential of approximately 0.9V. In contrast, the experimental data shows a change over point at approximately 0.775V. The experimentally observed changeover potential in the temperature study is not consistent with the changeover potential from the pressure study. In addition to the data shown in his work, the pressure study also reports

Table 2.6: Comparison between experimentally and numerically obtained Tafel slopes for varying cell temperatures.

Temp. $[K]$	Experimental [mV/dec]	Numerical [mV/dec]
313	-67.6	-67.9
	-113.86	-123.9
323	-68.33	-69.6
	-119.53	-127.6
333	-69.35	-71.3
	-110.49	-131.2
343	-71.24	-72.9
	-113.76	-134.7
353	-76.22	-74.6
	-115.89	-138.1

kinetic data for oxygen pressures between 2-7atm, which includes data at 5atm. This is the pressure used in the temperature study. The changeover potential is observed to be at approximately 0.9V, in agreement with the value shown in by the kinetic model. The discrepancy between the changeover potentials makes comparing the two data sets difficult, however it can been seen in the low Tafel slope region that the spacing between I-V curves appears consistent for both the experimental and numerical data. This is not as clear in the high Tafel slope region, where the 353K temperature curve for the experimental data crosses the 313K temperature curve. this is likely showing losses that are not kinetic which will not be reproduced with the numerical model.

Table 2.6 shows the Tafel slopes that are found for the experimental and simulated data. Again, the lower Tafel slopes are showing good agreement, while the upper Tafel slope region is showing significant errors. The numerical upper Tafel slopes are consistently higher than the experimental ones, in particular in the area of high temperature. The trend seen in the numerical data is for increasing Tafel slope with increasing temperature, which is not observed in the experimental data. The literature is not consistent on this trend, Beattie [22] and Zhang [34] provide experimental data that is consistent with the numerical model (i.e. increasing Tafel slope with increasing temperature). Mani et al. [33] provide data that shows a constant Tafel slope with increasing temperature, which is consistent with the data from Parthasarathy et al. To better capture the hcd temperature trends, data that is consistent and accurate is required. Chapter 3 contains comparisons to experi-

Table 2.7: Percentage error between the Tafel slopes reported the experimental data in the temperature study and those predicted by the kinetic model using either the parameters from Wangs et al. or those fitted in this work.

	Low Tafel slope region					High Tafel slope region				
This work	-0.4	-1.9	-2.8	-2.3	2.1	-8.8	-6.8	-18.7	-18.4	-19.2
Wang et al.	19.5	20.5	22.0	24.3	29.4	-6.6	-4.2	-15.6	-14.7	-14.8

mental data at high temperatures (80℃ and 95℃) so the kinetic losses in the high Tafel slope region may be slightly overestimated. The changes of the Tafel slopes with changing temperature can be encapsulated by looking at the apparent transfer coefficient the model predicts. Parthasarathy et al. showed a constant transfer coefficient of unity in the low Tafel slope region, the double trap model predicts a value from 0.91 to 0.94. In the high Tafel slope region, a transfer coefficient of 0.5-0.6 is found by Parthasarathy, while a constant value of 0.5 is found by the kinetic model. Again, the transfer coefficient appears to be reasonably well captured.

Tables 2.7 and 2.8 shows the percentage difference between the Tafel slopes predicted using the original parameters reported by Wang et al. and the estimated parameters from this work. It is clear that the new parameters can accurately reproduce the experimental data, particularly in the lcd region. There are some errors in the hcd region, for both sets of estimated parameters. These errors are within the variations reported in the Tafel slopes given by Parthasarathy. Taking an average of all the high Tafel slope percentage errors returns a value of 12% for the new estimated parameters compared to an average error of 9% for the original parameters. However, in the low Tafel slope region, the average of the errors are 3% for the new parameters and 24% for the original parameters. This major discrepancy shifts the result in favor of the new parameters, with an overall average error of 8% compared to 16% for the original parameters, showing a clear improvement in accuracy. This result along with the improvement in the predicted reaction order and the range of predicted current density, show that the kinetic parameters obtained in this work significantly improve the overall accuracy of the kinetic model. Further comparison of the data sets will be made in Chapter 3, when both data sets are used in a full MEA model that simulates a fuel cell operating under realistic conditions.

Table 2.8: Percentage error between the Tafel slopes reported the experimental data in the pressure study and those predicted by the kinetic model using either the parameters from Wangs et al. or those fitted in this work

	Low Tafel slope region					High Tafel slope region				
This work	0.6	5.8	6.3	8.3	4.6	-13.8	-21.6	-7.8	7.9	5.5
Wang et al.	23.0	25.8	25.8	27.1	24.0	-1.6	-11.3	1.0	13.3	10.5

2.4.4.4 Effect on Coverage of Intermediate Species

Changing the free energies may change the relative dominance of the intermediate reactions, resulting in different mechanisms dominating and different profiles for the intermediate species. Therefore, the results and conclusions discussed in Section 2.3.3 may not apply to the updated model. Note that while coverage conditions were imposed when fitting the experimental data, the conditions were imposed to the total coverage, or summation, of the two intermediate species. No conditions are imposed relating to the profiles of the individual species.

Figure 2.14 shows the profiles of the intermediate species, as well as the total coverage. The total coverage profile is consistent with experimentally found coverages, where the lcd coverage is very high and the hcd coverage is very low. Experimental data was taken from work by Subramanian et al. who found the coverage profile given by the points. The kinetic model shows remarkably good agreement with the experimental data, in particular, the very sharp decrease in the coverage profile between an overpotential of 0.3V and 0.5V. It was found that by varying the potential at which the low overpotential constraint (equation (2.59)) was evaluated, the location of the sharp decrease region could be shifted to the right or left. For example, evaluating the constraint at $0.9V$ would maintain the very high and very low overpotential coverages at 0% and 100% respectively, but the onset of the drop in coverage would occur at a lower overpotential. Similarly, the onset of drop would occur at a high overpotential if the potential at which the constraint was evaluated was increased to $0.8V$. However, the residual for both of these cases was higher than that for the case were the constraint was evaluated $0.85V$. The fit the current density was deemed to be more important than matching exactly the coverage profile, so the constraint was evaluated at $0.85V$. Note that this general formulation of the constraints on the coverage were deliberately kept general due to the lack of kinetic data in the literature. The close agreement of the kinetic model with the unrelated

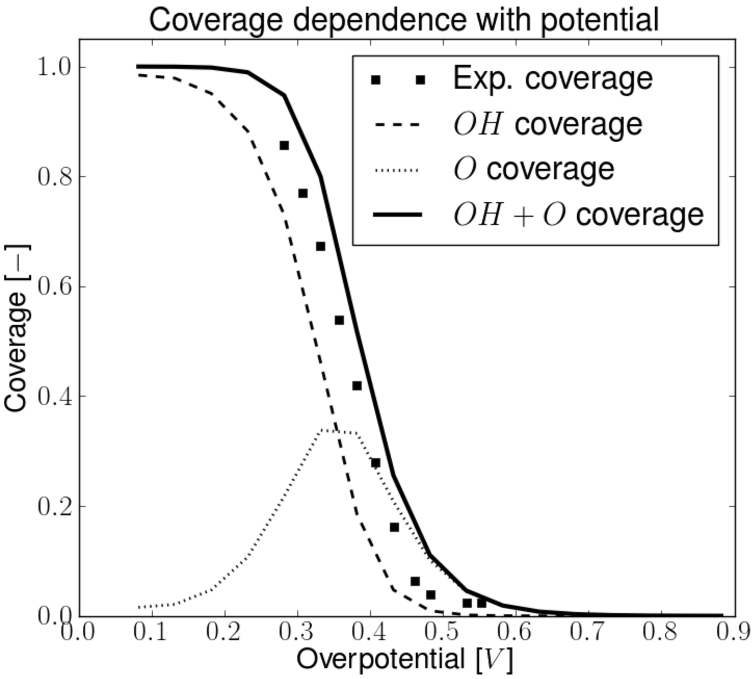

Figure 2.14: Coverage of the OH_{ads} and O_{ads} species as well as the addition of the two coverages. Experimental data points taken from Subramanian et al. [11].

coverage experimental data adds further validation to the accuracy of the kinetic model.

Figure 2.14 also shows the individual profiles of the intermediate species. The OH_{ads} intermediate is clearly the dominant species, covering the entire platinum surface at very low potentials, before quickly decreasing to zero. The O_{ads} intermediate is less prevalent, however still rises to over 30% in the sharp decrease region before reducing to zero. This is in contrast to the coverage profiles found by Wang et al. shown in Figure 2.7. Using the kinetic parameters provided by Wang et al., the O_{ads} was the dominant species, with the OH_{ads} intermediate only becoming prominent at higher overpotentials. However, the OH_{ads} coverage is non-zero at very high overpotentials using the original kinetic parameters, which is not consistent with the coverage profile given by Subramanian et al. Using the fitted parameters from this work, the very high overpotential coverage is zero, giving more confidence in the validity of the updated model. Note that this zero coverage at high overpotentials was not rigorously imposed during the data fitting. The second non-linear constraint imposes a total coverage of 0% to 20% in this region, so the optimizer is not overly constrained in this region. That the model will naturally return a zero coverage profile at high overpotentials gives further confidence to the enhancements made to the original model, in particular, correctly accounting for oxygen depletion.

Figure 2.15 shows the profiles of the total coverage as well as the individual species for different oxygen partial pressures. The total coverage profile shows small changes over the four different oxygen pressures, which are over a wide range (0.01atm to 5 atm). Interestingly the coverage of the intermediate species shows significant changes. At zero overpotential, the OH_{ads} species entirely covers the reaction sites, however diminishes to zero with increasing overpotential. At very high oxygen partial pressures, this occurs very rapidly, due to the rapid increase in the O_{ads} intermediate which achieves coverages as high as 60% at 5atm of oxygen pressure. These results show that experimenters should exercise caution when trying to determine the intermediate species that dominates the ORR, as the dominant species may change with changing oxygen pressure.

2.4.4.5 ORR Mechanism

Wang et al. report that O_{ads} is the dominant species in the lcd region, whereas this work predicts that the OH_{ads} species will be dominant. This change in dominance is due to the differences in the free energies used by Wang et al. and those used in this work. As the absorption and activation energies have changed, the conclusions reached in section 2.3.3 using Wangs parameters are not valid here. Figures 2.16(a) and 2.16(b) show the changing energy barriers for the intermediate reactions in the lcd and hcd regions respectively using the fitted parameters from this work. The general trend for the energy barriers is the same as for the trends found using the original kinetic parameters, at low overpotentials the energy barriers are higher than those for high overpotentials. However, for the new kinetic parameters the OH_{ads} intermediate occupies the lowest energy state in contrast to O_{ads} in the original work. This accounts for the change in dominance from O_{ads} to OH_{ads} with the change in parameters. The new parameters show that at low overpotentials, any water in the layer will spontaneously form OH_{ads} (i.e. the backward RD energy barrier is negative, meaning that there is no barrier to the formation of OH_{ads}). This dominance of the OH_{ads} intermediate due to the absorption of water predicted by the kinetic model is also seen experimentally in the research performed by Murthi et al. [71]. Rotating ring disk electrode experiments in oxygen-free sulphonic acid were performed and the current density was recorded. The reaction proceeded by reacting

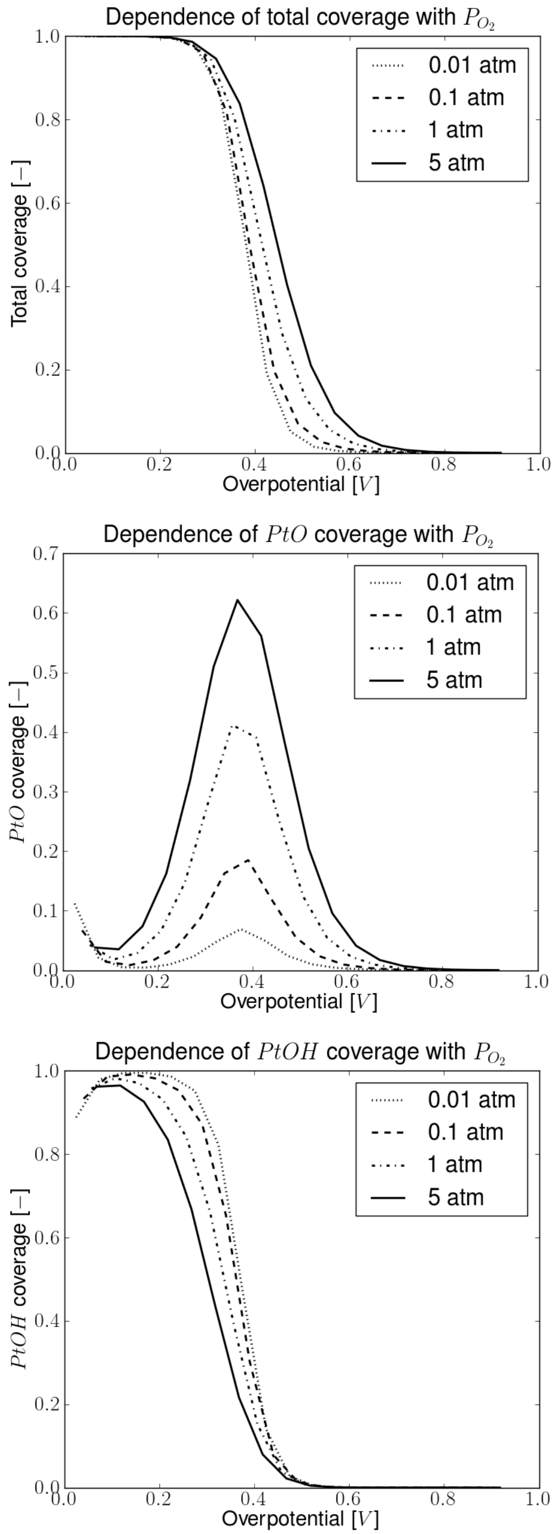

Figure 2.15: Coverage of the OH_{ads} and O_{ads} species and the total coverage for changing oxygen partial pressures.

the water introduced into the acid in varying amounts. When very low quantities of water were introduced into the acid, the doubling of the Tafel slope was not present and a CV showed lower coverage of intermediate species. The experimental results in [71] agree very well with the results obtained using the kinetic model.

Figure 2.16(b) shows that H_2O occupies the lowest energy state at high overpotentials, hence the ORR can now be completed. This is facilitated by the forward RD reaction becoming dominant over the backward reaction, indeed, the forward reaction is now spontaneous, so any OH_{ads} produced will quickly form water. This accounts for the rapid decrease in the OH_{ads} shown in Figure 2.14. The small rise and then decrease in the O_{ads} intermediate can be accounted for by noting that the forward RT reaction barrier is initially higher than that of the forward DA reaction. As the overpotential increases, the RT barrier reduces in size until it is smaller than the DA barrier, leading to the O_{ads} being cleaned from the surface. This is further facilitated by the RA forward reaction barrier reducing in size relative to the DA barrier, leading to greater production of OH_{ads} compared to O_{ads}.

The change in the Tafel slope with increasing overpotential is most likely due to the change in dominance from the backward RD reaction to the forward RD reaction, along with the change in dominance of the RA reaction pathway compared to the DA reaction pathway. This leads to the change in the coverage profile from high coverage to low coverage, which leads to a different Tafel slope. The reason for the low value for the Tafel slope in the lcd region compared to the high Tafel slope in the hcd region is difficult to determine. The Tafel slope is generally given in units of mV/dec and therefore describes how much additional overpotential must be applied to achieve an increase of a decade in the current density. It can therefore be considered the sensitivity of the produced current density to a change in the applied overpotential. At low overpotentials, each of the reactions is likely to be important. The DA barrier is less than the RA barrier so will dominate, yet the considerable RT barrier must still be overcome, before both reaction paths must overcome the smaller RD barrier. A change in overpotential in this regime will reduce the energy barrier of the RA and RT barrier(recall that the DA reaction is not electrochemical, see equation (2.1)). Therefore a small change in overpotential will result in the simultaneous lowering of energy barriers in both reaction pathways, resulting in the 'overall' reaction rate requiring little overpotential to make a large change in current.

By contrast, at high overpotentials, the RA pathway is more active than the

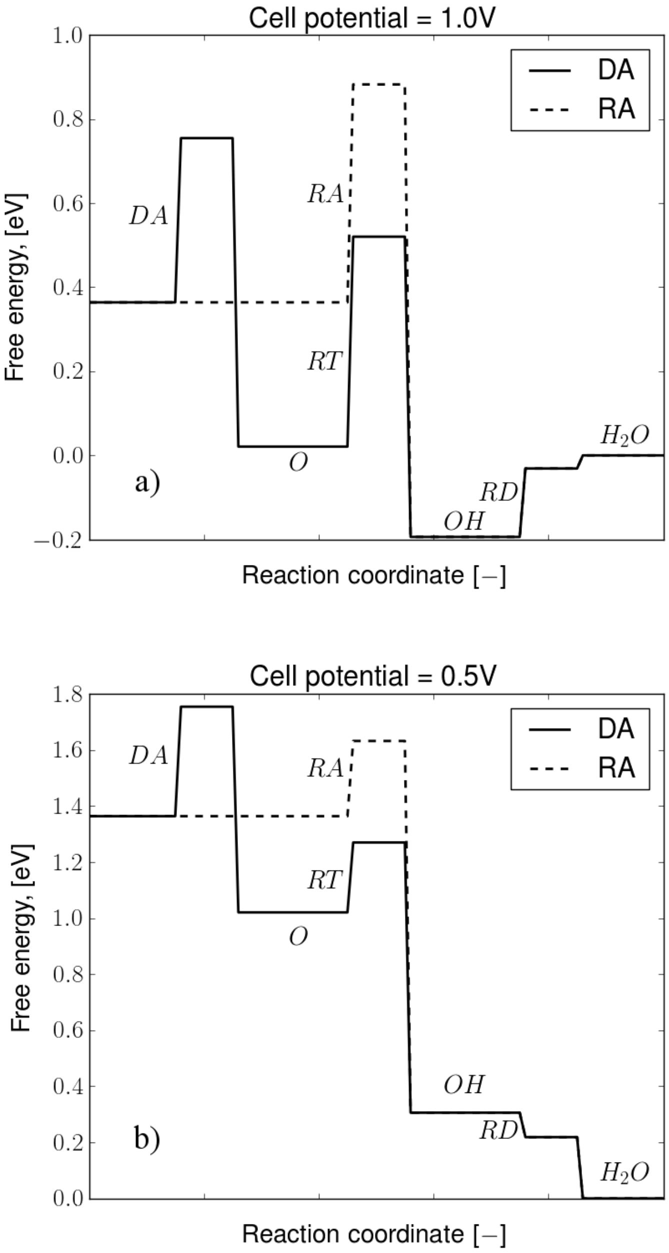

Figure 2.16: Reaction coordinate plot at a) a cell potential of $1.0V$ corresponding to the lower Tafel slope region, and b) a cell potential of $0.5V$ corresponding to the upper Tafel slope region. Note that both paths overlap for the RD reaction. The solid line denotes the path whereby the oxygen first desorbs onto the platinum as a O_{ads} species, while the dashed line denotes the case where OH_{ads} is formed first.

DA reaction, removing the importance of the RT reaction at the same time. At this overpotential, the forward RD barrier now dominates the backward RD barrier, however the forward barrier is now negative, resulting in a spontaneous reaction. As there is no barrier to be overcome, increasing the overpotential will not increase the rate at which this reaction occurs. Therefore only a reduction in the RA barrier will produce a meaningful change in the current density. So, because increasing the overpotential will only reduce a single important barrier, the value of the Tafel slope is greater at high overpotentials compared to at low overpotentials where a change in overpotential produced a meaningful decrease in the barriers of three reactions.

Finally, the changing energy barriers can shed some light on the reason for the shape of the reaction order plot as shown in Figure 2.12. The figure shows that at low and high overpotentials the reaction order has a value of 0.5, with a decrease to 0.33 at an overpotential around 0.35V. A value of 0.5 matches the 1/2 stoichiometry of the assumed intermediate reactions that involved molecular oxygen (i.e. equations (2.1) and (2.2)). At low overpotentials, the DA reaction has a lower energy barrier than the RA reaction, so the molecular oxygen reacts primarily along the DA pathway. At high overpotentials, the RA reaction has the lower energy barrier. The one half reaction order reflects that all the molecular oxygen is reacting via one pathway only, i.e. the RA pathway, corresponding to the one half stoichiometry. At medium overpotentials, the DA and RA energy barriers are closer in value such that both pathways are simultaneously reacting the molecular oxygen. A rise in coverage of the O_{ads} intermediate is seen in this potential region which is not being reacted by the RT reaction to form OH_{ads}. The O_{ads} is therefore blocking the overall reaction so the oxygen used to form the O_{ads} is 'wasted'. Hence, the reaction order drops in this region, which is indicative of the reaction using the provided oxygen in a less 'effective' manner. This reduction in the oxygen reaction order, coupled with the value of 0.91-0.94 for the apparent transfer coefficient, would indicate that the overall ORR does not have a rate determining step at low current densities. If one of the steps was the RDS, then the overall transfer coefficient and reaction order would mirror the transfer coefficient and reaction order of the step. This is clearly not the case at low current densities. At high current densities, the reaction appears to be absorption limited, as the reaction order is one half, as is the transfer coefficient. This leads to the conclusion that the reductive absorption step is the RDS. This is also apparent in the energy barrier diagram at high overpotentials, the RD reaction is spontaneous and the DA energy barrier is higher than that of the RA energy barrier so the RA reaction will dominate. Note that these conclusions are the result of the simplifying assumption that the initial reaction of the ORR can be simplified to $1/2O_2$ being reacted on the platinum. If the assumed intermediate steps are changed to include the reaction steps presented by Ruvinskiy et al., where oxygen with a stoichiometry of one participates in the initial reaction, then the reaction order may also change to one, matching with the experimental data. Further research in this area is needed to investigate this possibility.

The conclusions reached here should be treated with caution. Figures 2.17(a) to 2.17(d) shows sample results from a post-sensitivity analysis, where the sensitivity of the current density and the non-linear constraints to changes in the design variables is plotted. The current density is normalized by the average of the current produced over a single curve. The current densities are produced in different orders of magnitude depending on the cell potential, so normalization is required to compare each of the curves. The results are shown for a cell potential of 1.0V and 0.85V corresponding to the low overpotential region, and at 0.4V which is in the high overpotential region. The 0.4V and 0.85V are also the potentials at which the nonlinear constraints are evaluated.

Figure 2.17(b) and (d) shows the change of the current current density with the changing free energy of adsorption of the OH_{ads} species. The value for this parameter returned by the optimizer is shown with a solid vertical line. The figure shows that a change in the OH_{ads} absorption free energy will produce significant changes in the current density at low overpotential. The optimizer could potentially change this parameter in order to further reduce the objective function. However, the low overpotential constraint (the bound of which the optimizer was very close to) shows some sensitivity to the changing OH_{ads} absorption free energy, so the optimizer is constrained. This gives very little room for any variance in this parameter, giving some confidence in the final value chosen by the optimizer for the the value of the free energy of the OH_{ads} intermediate.

In contrast, Figure 2.17(a) and (c) shows the dependence of the free energy of activation of the RD reaction. The optimizer chose a value of 0.278eV for this parameter, however increasing or decreasing that value by 0.1eV (a 35%) change will produce no change in the computed current at any overpotential. The high overpotential has constraint some sensitivity to this parameter, however this constraint

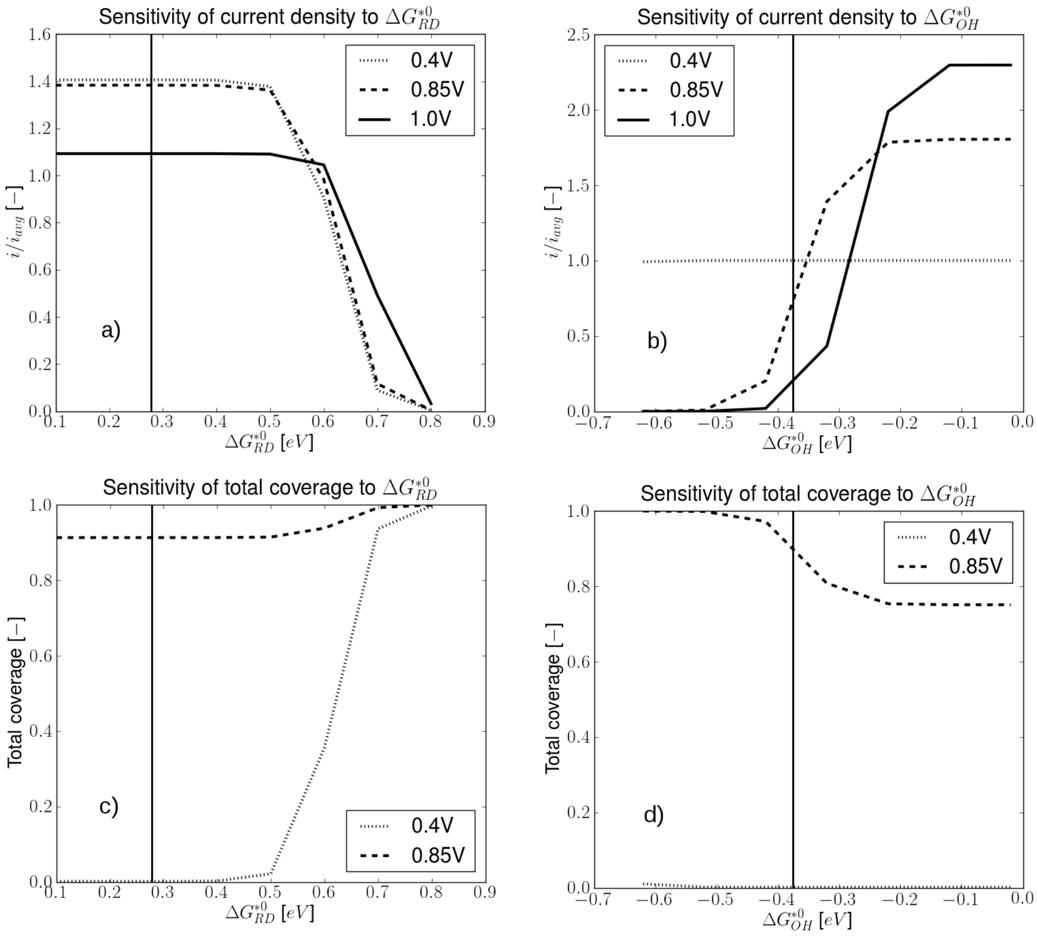

Figure 2.17: Sensitivity of the current density, hcd coverage constraint (0.4V) and lcd constraint (0.85V) as predicted by the double trap model to a) the free energy of activation of the RD reaction, a) and c), and to the free energy of adsorption of the OH_{ads} intermediate b) and d). The current density sensitivity analysis is done for a constant cell potentials of $0.4V$ (high overpotential), $0.85V$ and $1.0V$ (low overpotential). The solid vertical line shows the value of the fitted parameter. Note that current density plots are normalized by the average value of the current produced for a single curve.

was not close to its upper bound, so its importance is less than that of the low overpotential constraint, which shows no sensitivity. This trend shows that the RD free energy could be changed significantly but show no appreciable effect on the final result as far as the optimizer is concerned. The potential for large variance in this parameter gives less confidence to the value chosen by the optimizer. While changing this parameter will not vary the final objective function or constraint, it may effect the results shown in Figures 2.16(a) and 2.16(b) by changing the size of the energy barriers.

This analysis shows the difficulties in attempting to draw conclusions on the fundamental nature of the ORR based on the results of parameter fitting. Parameter insensitivities can hide the significant variability of the kinetic parameters which may effect the energy barriers show in Figures 2.16(a) and 2.16(b). More rigorous analysis is needed in order to investigate the mechanism of the ORR with confidence. This would require improvements in the experimental data such as performing the parameter fitting with more data that covers a wider range of operating conditions, providing data that is 'cleaner', i.e. shows clear trends with minimal experimental error and providing more data on the nature of the coverage of the intermediate species. The optimization would need to be improved by probing the design space with a greater number of initial points or using different optimization methods such as global methods to ensure that the global minimum is found. Nevertheless, the kinetic model with the fitted parameters from this work has significantly improved the accuracy of the model in comparison to the kinetic parameters provided by Wang et al. With the new parameters, the model was shown to better capture the experimental Tafel slopes, oxygen reaction order and also show remarkable agreement with experimentally obtained coverage profiles.

Chapter 3

PEM Fuel Cell Modeling

3.1 Introduction

Kinetic losses, such as those presented in the previous section, are due to the energy barriers that must be overcome in order for the half cell reactions described in equations (1.2) and (1.3) to proceed. A fuel cell operating under realistic conditions will incur a number of other losses that will limit its performance, such as the transport of reactants to the reaction sites. This chapter will describe a mathematical model that accounts for the main mass and charge transport losses that are incurred in a fuel cell.

The main aim of this chapter is to examine the effect of using the kinetic model described in Chapter 2 to describe the kinetic losses incurred by the ORR in cathode catalyst layer of the fuel cell. The new kinetic equation will be implemented in the fuel cell model and compared to the same fuel cell model with the commonly used Tafel equation that does not account for the doubling of the Tafel slope. The relative importance of the doubling of the Tafel slope can then be investigated in relation to some of the major losses incurred in a fuel cell, namely the ohmic losses incurred in the membrane and the mass transport limitations (when the fuel cell cannot provide enough oxygen to maintain the reactions). The accuracy of the model will be judged based on comparison to experimental data.

3.2 Membrane Electrode Assembly (MEA) Model

3.2.1 Overview

Figure 3.1 shows a schematic of the PEM fuel cell that is modeled in this work. The model is based on the MEA model developed by Secanell [68], and further

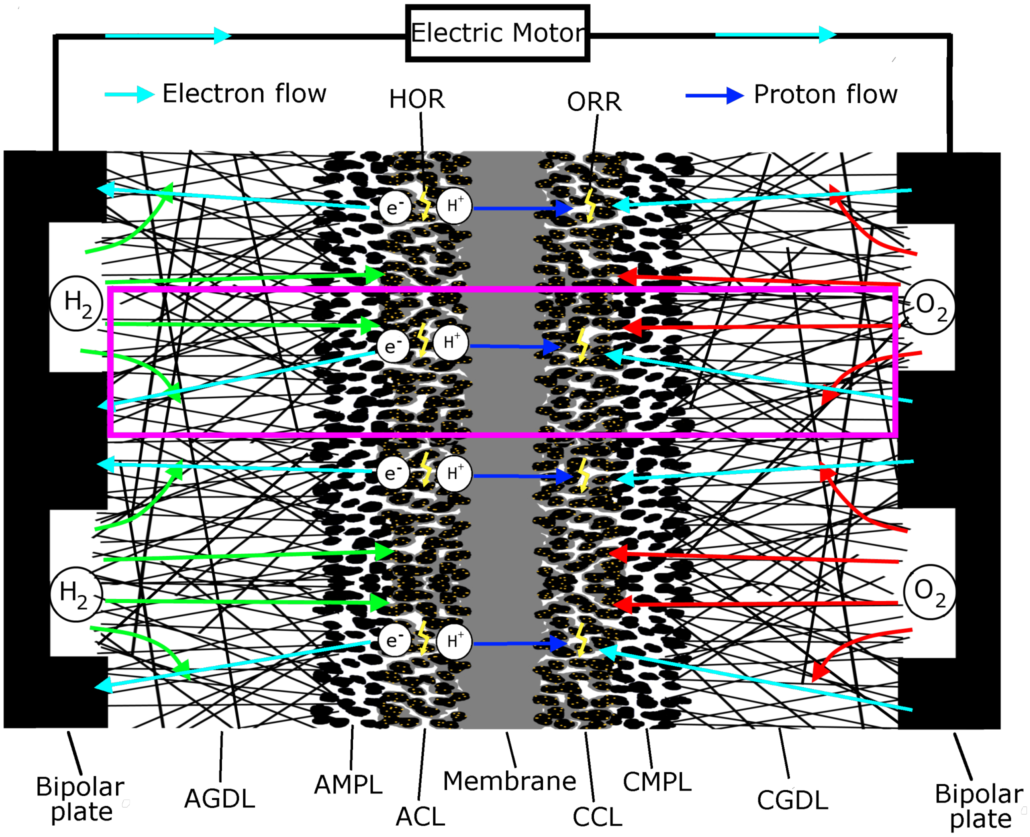

Figure 3.1: An across-the-channel section of a single PEM fuel cell. The computational domain is shown by the solid purple line.

extended by Dobson [69]. The model is a 2D, across-the-channel model. The model accounts for the transport of gases from the channel towards the reaction site, with the species transport occurring in the in-plane and through-plane directions. This model assumes steady state operation. The basis for this assumption is that the fuel cell has been operating for a sufficient length of time to allow the cell to equilibriate.

In this model, the transport of five species is considered. The first are the reactants, hydrogen and oxygen, which are delivered to the fuel cell via the gas channels etched into the bipolar plate. The hydrogen is delivered on the anode side of the cell, while oxygen is delivered on the cathode side. The reactant must travel through the gas diffusion layer (GDL) and the micro-porous layer (MPL) in order to reach the catalyst layer (CL) where the reactions can occur. Hence, the transport of the reactants is considered only in the GDL, MPL and CL on both the anode and cathode side, and their consumption occurs in the CL.

The presence of water is also considered in the model. It is assumed that the reactants are provided to the cell as a humidified gas. Oxygen is delivered in the form of humidified air, so that the cathode gas is a mixture of nitrogen, oxygen and water vapor. Hydrogen is delivered as a binary mixture of pure hydrogen and water vapor. Water is also produced in the cathode catalyst layer as the product of the ORR, hence a source will be included to account for its production. Water is assumed to be produced in vapor form and its condensation is not considered. Modeling water in liquid and vapor form adds major complexity to the model, as two phase models are required. The assumption that water exists only in vapor form can be justified by the interest of this work on the kinetic region, i.e. low current densities, and by limiting the study to a low relative humidities (RH) for the input gases and high cell temperatures, i.e. 80°C and 95°C.

The input gases need to be humidified to ensure adequate hydration of the membrane and ionomer in the CL. The membrane is a polymer-electrolyte that will absorb and desorb water during operation. The relative humidification level of the membrane will affect its ability to conduct protons from the anode to cathode catalyst layers. Therefore, the MEA model accounts for water adsorption, desorption and transport in the electrolyte. Once water is absorbed into the membrane, it can travel from one side to another based on a chemical gradient or due to electrochemical drag. The water will therefore exist throughout the cell, as water vapor in the anode and cathode side GDL, MPL and CL, and as absorbed liquid water in the membrane and CL.

The fuel cell is assumed to operate at a constant temperature and pressure. This assumption, coupled with the assumption that the gases behave as ideal gases, result in the total concentration of all species being constant in the anode and cathode. The molecular volume of a single species can therefore be expressed as a fraction of the total molecular volume present in each side of the cell. This fraction is called the mole fraction. The addition of the mole fractions for each species for a gaseous mixture will equal one. As such, only the mole fraction of water vapor is solved for, as the mole fraction of hydrogen can be found by subtracting the mole fraction of water vapor from one. Similarly, water vapor and oxygen only are solved for in the cathode side. This reduces the number of equations needed in the fuel cell model.

The transport of the charged species is also considered. Protons are produced in the anode side of the cell and will travel from the anode catalyst layer, through the membrane to the cathode catalyst layer. It is assumed that there is sufficient anion

Table 3.1: Table of unknown variables solved for in the MEA model.

Electrode	Anode				Cathode		
Unknown variable	GDL	MPL	CL	PEM	CL	MPL	GDL
O_2 molar fraction, x_{O_2}					X	X	X
H_2O molar fraction, x_{H_2O}	X	X	X		X	X	X
Electron potential, ϕ_s	X	X	X		X	X	X
Proton potential, ϕ_m			X	X	X		
Water absorbed by ionomer, λ			X	X	X		

groups present in the membrane and the ionomer in each CL to allow for the free transport of protons. This assumption leads to the uniform concentration of protons in the membrane and CLs such that the transport of protons is dependent on the electrolyte potential only. The electrolyte potential will be solved in the membrane and both CL.

Electrons produced in the anode CL cannot travel through the membrane and must travel back through the anode GDL and MPL to the bipolar plate, through the external load and the cathode side bipolar plate, GDL and MPL to the cathode catalyst layer. These layers are assumed to be electronic conductors. This assumption leads to the transport of electrons being dependent on the electronic potential only. The electronic potential is therefore solved for in each layer, apart from the membrane.

There are therefore five unknowns that will be solved for. Table 3.1 provides a summary of these variables, along with which layers each unknown is present in. The composition and structure of the individual layers are varied in order to accommodate each of the species present in the layer.

3.2.2 Governing Equations

The governing equations for the five solution variables can be found by performing a mass balance across an infinitesimal control volume:

$$\frac{\mathrm{d}c_i}{\mathrm{d}t} + \nabla \cdot \mathbf{N}_i = S_i \tag{3.1}$$

where c_i is the molar concentration of the i^{th} species, $\mathbf{N}_i$ is the molar flux of the i^{th} species and S_i denotes the source/sink term for the species. This model is assumed to operate at steady state, therefore the time dependent term is zero. The system of equations will therefore take the form of

$$\begin{aligned} \nabla \cdot \mathbf{N}_{O_2} &= S_{O_2} \\ \nabla \cdot \mathbf{N}_{H_2O} &= S_{H_2O} \\ \nabla \cdot \mathbf{N}_{H^+} &= S_{H^+} \\ \nabla \cdot \mathbf{N}_{e^-} &= S_{e^-} \\ \nabla \cdot \mathbf{N}_{\lambda} &= S_{\lambda} \end{aligned} \tag{3.2}$$

3.2.2.1 Gaseous Species

The fluxes for the gaseous species are assumed to be described by Fick's first law of diffusion, i.e.

$$\mathbf{N}_i = -D_{ij} \nabla c_i \tag{3.3}$$

where D_{ij} is the diffusion coefficient of a species i in a binary mixture with species j. The anode is fed with a binary mixture of hydrogen and water vapor so this assumption is valid provided there is no convection. The no-convection assumption arises from the assumption that the cell is isobaric, resulting in no driving force for convective flow. At the anode, only an equation for the water vapor mole fraction is solved for. The mole fraction of the hydrogen is found using $x_{H_2} = 1 - x_{H_2O}$. The cathode side of the cell is fed with humidified air, i.e. a mixture of nitrogen, oxygen and water vapor. This is a multi-component mixture and should therefore be described by the Maxwell-Stefan equations. This set of equations can describe the flux of species i by considering its interaction with all other species. However, air can be considered a dilute mixture, due to the high mole fraction of nitrogen in comparison to the other species. Because the oxygen and vapor are provided in much lower mole fractions than that of nitrogen, the interactions between the oxygen and vapor should be negligible. The system can therefore be considered a pair of binary mixtures of vapor in nitrogen and oxygen in nitrogen.

The Fick's law assumption will lead to the flux of the oxygen and water vapor being described using:

$$\mathbf{N}_{O_2} = -c_g D_{O_2,N_2} \nabla x_{O_2} \tag{3.4}$$

and

$$\mathbf{N}_{H_2O} = -c_g D_{H_2O,N_2} \nabla x_{H_2O} \tag{3.5}$$

where x_{O_2} is the mole fraction of oxygen, x_{H_2O} is the mole fraction of water vapor and c_g is the total gas concentration is the anode/cathode (note that the multiplication of x_i and c_g will give the concentration of species i, c_i). The diffusion coefficients

D_{ij} are found using Chapman-Enskog theory. Note that the coefficients returned by Chapman-Enskog theory will be bulk diffusion coefficients, i.e. applicable when the mixture is in a free space. The fuel cell layers are porous materials so diffusion coefficients will have to be adjusted to account for the tortuosity and porosity of the layers in which the species are found. This is described in section 3.2.4.

3.2.2.2 Charged Species

The transport of protons and electrons is considered in this model. Assuming an infinitely dilute electrolyte, the flux of protons is governed by the Nernst-Planck equation:

$$\mathbf{N}_{H^+} = -D_{H^+}\nabla c_{H^+} - \frac{z_{H^+}F}{RT}D_{H^+}c_{H^+}\nabla\phi_m + c_{H^+}\vec{v} \tag{3.6}$$

For a solid electrolyte, the velocity term $\vec{v}$ will be zero. Due to the presence of ionomer chains through the catalyst layers and membrane, it can be assumed that the concentration of protons will be evenly distributed throughout the domain and equal to the number of sulphonic acid groups in the polymer electrolyte. The gradient of the proton concentration will therefore be zero. Equation (3.6) then reduces to the following equation:

$$\mathbf{N}_{H^+} = -\frac{z_{H^+}F}{RT}D_{H^+}c_{H^+}\nabla\phi_m \tag{3.7}$$

where z_{H^+} is the valency of a proton (i.e. +1). D_{H^+} is the diffusion coefficient of the protons in the electrolyte, c_{H^+} is the concentration of protons in the ionomer and ϕ_m is the ionomer potential, one of the solution variables. Many of the terms can be grouped together to find the proton conductivity of the ionomer:

$$\sigma_m = \frac{z_{H^+}^2F^2D_{H^+}c_{H^+}}{RT} \tag{3.8}$$

where σ_m is the conductivity of the the ionomer. The final form of the proton flux in the ionomer will be given as:

$$\mathbf{N}_{H^+} = -\frac{\sigma_m}{z_{H^+}F}\nabla\phi_m \tag{3.9}$$

For an electronic conductor, Ohm's Law will give a similar result:

$$\mathbf{i} = z_{e^-}F\mathbf{N}_{e^-} = -\sigma_s\nabla\phi_s \tag{3.10}$$

where z_{e^-} is the valency of an electron (and is equal to -1) and ϕ_s is the solid phase potential, one of the solution variables.

3.2.2.3 Absorbed Water

The final equation in the system of equations (3.2) governs the transport of absorbed water in the polymer electrolyte. The model used in this work is the same as that presented by Springer et al. [50]. The model accounts for the transport of water due to electro-osmotic drag and diffusion due to a concentration gradient. The transport of water due to electro-osmotic drag relates to protons traveling from the anode to the cathode and dragging water molecules with it due to their polarity. It was found experimentally that a single ion will drag 2.5 molecules of water across the membrane when it is fully hydrated and in equilibrium with liquid water. The amount of water available in the membrane to be moved by the protons is given by the water content, λ, which is expressed as the ratio of water molecules per sulphonic acid group, (SO_3^-), present in the polymer electrolyte.

$$\lambda = \frac{c_{H_2O}}{c_{SO_3^-}} \tag{3.11}$$

where c_{H_2O} is the concentration of water molecules that have been absorbed into the membrane and $c_{SO_3^-}$ is the concentration of sulphonic groups. This concentration can be approximated using the density of the dry membrane and the equivalent weight of the ionomer. The equivalent weight (EW) is defined as the dry mass of the membrane per mole of SO_3^-, and is specified by the membrane manufacturer. Hence, $c_{SO_3^-}$ can be found using

$$c_{SO_3^-} = \frac{\rho_{m.dry}}{EW} \tag{3.12}$$

where $\rho_{m.dry}$ is the dry membrane density. Springer et al. found experimentally a maximum water content of 22 when the membrane is immersed in liquid water at 100°C. It was assumed that the number of water molecules dragged with each proton was linearly proportional to the water content in the membrane, so the drag coefficient n_{drag} was expressed as:

$$n_{drag} = \frac{2.5}{22}\lambda \tag{3.13}$$

based on experimental data [50]. The water flux can then be described by:

$$\mathbf{N}_{w,drag} = n_{drag}\mathbf{N}_{H^+} \tag{3.14}$$

where the proton flux $\mathbf{N}_{H^+}$ is given by equation (3.9).

The diffusion of water in the membrane takes the same form as that used by for the transport of gaseous species. The flux of water due to diffusion is given by:

$$\mathbf{N}_{w,diff} = -D_{H_2O}\nabla c_{H_2O} \tag{3.15}$$

where D_{H_2O} is the diffusion coefficient of water in the ionomer. Using equations (3.11) and (3.12), the concentration of water can be replaced with the gradient of the water content:

$$\mathbf{N}_{w,diff} = -D_{\lambda}\frac{\rho_{m,dry}}{EW}\nabla\lambda \tag{3.16}$$

where D_{λ} is now the water content diffusion coefficient.

3.2.3 Source Terms

Having derived expressions for the fluxes in each of the governing equations, they can now be expressed as:

$$\begin{aligned}
\nabla\cdot\left(-c_g D_{O_2,N_2}\nabla x_{O_2}\right) &= S_{O_2}\\
\nabla\cdot\left(-c_g D_{H_2O,N_2}\nabla x_{H_2O}\right) &= S_{H_2O} + S_{\lambda}\\
\nabla\cdot\left(-\frac{\sigma_m}{z_{H^+}F}\nabla\phi_m\right) &= S_{H^+}\\
\nabla\cdot\left(-\frac{\sigma_s}{z_{e^-}F}\nabla\phi_s\right) &= S_{e^-}\\
\nabla\cdot\left(n_{drag}\frac{\sigma_m}{z_{H^+}F}\nabla\phi_m + D_{\lambda}\frac{\rho_{m,dry}}{EW}\nabla\lambda\right) &= -S_{\lambda}
\end{aligned} \tag{3.17}$$

The right hand side terms S_i for each of the equations will now be defined. There are two types of source terms that are considered in this model. S_{λ} refers to the absorption/desorption of water in the membrane. This will affect the water equation and the water content equation. The remaining source term relate to the current produced in the cell.

3.2.3.1 Current Production

The current produced in the cell will act as a sink for the oxygen, electrons and protons, and a source for the water equation on the cathode side of the cell. On the anode of the cell, the current produced will act as a source for electrons and protons. Therefore the source terms for the first four equations in equation (3.17) will depend on the current produced in the cell. The current is a flow of protons/electrons flowing in the electrolyte/carbon phase respectively.

The current produced in the ORR is related to the flux of a charged species by:

$$\mathbf{N}_i = -\frac{s_i}{nF}\mathbf{i} \tag{3.18}$$

where s_i is the stoichimetry of the species i, n is the number of electrons transferred in the reaction (four in the ORR) and $\mathbf{i}$ is the volumetric current density, i.e. the current produced per cm^3 catalyst layer. Applying this to the first four equations in equations (3.17):

$$\begin{aligned}
\mathbf{N}_{O_2} &= -\frac{1}{4F}\mathbf{i} \\
\mathbf{N}_{H_2O} &= \frac{2}{4F}\mathbf{i} \\
\mathbf{N}_{H^+} &= -\frac{4}{4F}\mathbf{i} \\
\mathbf{N}_{e^-} &= -\frac{4}{4F}\mathbf{i}
\end{aligned} \tag{3.19}$$

Similarly, in the anode side of the cell, the HOR will provide the source terms for the protons and electrons:

$$\begin{aligned}
\mathbf{N}_{H^+} &= \frac{2}{2F}\mathbf{i} \\
\mathbf{N}_{e^-} &= \frac{2}{2F}\mathbf{i}
\end{aligned} \tag{3.20}$$

Note that the signs have changed, as the HOR is producing the species, rather than consuming them, as is the case for water vapor in the ORR.

As shown in equations (3.2), the gradient of the species flux is equal to the source term for each equation. Therefore, equations (3.17) can be written as:

$$\begin{aligned}
\nabla \cdot (c_g D_{O_2,N_2} \nabla x_{O_2}) &= \frac{1}{4F}\nabla \cdot \mathbf{i} \\
\nabla \cdot (c_g D_{H_2O,N_2} \nabla x_{H_2O}) &= -\frac{1}{2F}\nabla \cdot \mathbf{i} + S_\lambda \\
\nabla \cdot \left(\frac{\sigma_m}{F}\nabla \phi_m\right) &= \frac{1}{F}\nabla \cdot \mathbf{i} \\
\nabla \cdot \left(\frac{\sigma_s}{F}\nabla \phi_s\right) &= -\frac{1}{F}\nabla \cdot \mathbf{i} \\
\nabla \cdot \left(n_{drag}\frac{\sigma_m}{F}\nabla \phi_m + D_\lambda \frac{\rho_{m,dry}}{EW}\nabla \lambda \phi_s\right) &= -S_\lambda
\end{aligned} \tag{3.21}$$

where the valency of the charged species z_i is accounted for. Note that there is a sign change on the source term for the water equation, due to the production rather than consumption of the species in the overall reaction. There is also an additional source term in the water equation due to the absorption of water into the membrane. This source term will be equal but opposite to the source term in the fifth equation in equations (3.17). The equations for the proton/electron transport will have the opposite signs to those shown when solved on the anode side.

The volumetric current $\mathbf{i}$ in the CCL is typically computed using the Tafel equation, as was derived in equation (1.26):

$$\mathbf{i} = i_0 \left(\frac{c_{O_2}}{c_{O_2}^{ref}} \right)^{\gamma} \exp\left(\frac{-\alpha F \eta}{RT} \right) \tag{3.22}$$

where oxygen depletion is accounted for with the inclusion of the $c_{O_2}/c_{O_2}^{ref}$ term. The overpotential η is computed using:

$$\eta = (\phi_s - \phi_m) - E_{eq} \tag{3.23}$$

where the equilibrium potential E_{eq} is computed using the Nernst equation (1.22).

In this work, this equation will be compared to the double-trap intrinsic kinetic equation that was derived in Chapter 2 (equation (2.43)):

$$j_k = 2j^* e^{-\Delta G^*_{RD}/kT} \theta_{OH} - 2j^* e^{-\Delta G^*_{-RD}/kT} (1 - \theta_O - \theta_{OH}) \tag{3.24}$$

An advanced kinetic model can also be used to account for the anodic current produced in the cell. The Butler-Volmer model is commonly used to account for the anodic current, as the overpotentials are smaller than those in the cathode and the backward reaction is important, so the Tafel equation cannot be used. In this work, the dual-pathway kinetic model developed by Wang et al. [72] is used to model the hydrogen oxidation reaction. The model assumes a single absorbed intermediate PtH and three intermediate steps giving two potential pathways for the overall reaction. The absorption of hydrogen onto the platinum can occur due to a Tafel or Heyrovsky reaction, while the Volmer reaction accounts for the desorption. The equation is given by

$$j_k = \frac{c_{H_2}}{c_{H_2}^{ref}} \left[j_{0T} (1 - e^{-2F\eta/\gamma RT}) + j_{0H} (e^{F\eta/\gamma RT} - e^{-F\eta/\gamma RT} e^{-F\eta/2RT}) \right] \tag{3.25}$$

where the exchange current density for the Tafel-Volmer and Heyrovsky-Volmer pathways are given by j_{0T} and j_{0H} respectively and γ is a potential constant.

Note that each of the above equations will return the current per cm^2 of platinum surface rather than the volumetric current required in equations (3.21). To convert to the volumetric current, both equations (3.22), (3.24) and (3.25) need to be scaled by the active area. This term relates the unit area of platinum surface available to the reaction per unit volume. Hence the units of $\frac{cm^2 Pt}{cm^3 CL}$. The active area, A_v is given by equation:

$$A_v = A_0 V_{Pt} \tag{3.26}$$

where V_{Pt} is the volumetric loading of platinum per cm^3 of catalyst layer and will be a property of the ink used to produce the catalyst layer. A_0 is the catalyst surface are per unit mass of catalyst particle and describes how much surface area is available to the reaction for a given mass of catalyst. Data provided by E-TEK [73] was used to do a least squares fit in order to find an equation that depends on the platinum to carbon weight ratio $Pt|C$:

$$\begin{aligned} A_0 = &7.401 \times 10^6 (Pt|C)^4 - 1.811 \times 10^7 (Pt|C)^3 + 1.545 \times 10^7 (Pt|C)^2 \\ &-6.453 \times 10^6 (Pt|C) + 2.054 \times 10^6 \end{aligned} \tag{3.27}$$

3.2.3.2 Membrane Water Sorption

The adsorption and desorption of water in the membrane is governed by a sorption isotherm. This water sorption between the CL and membrane will ensure that the membrane water content and the CL water vapor are in equilibrium, as the model is steady state. Based on the cell temperature, the humidification level of the membrane, and the activity of the water vapor in the catalyst layer, water vapor will either be absorbed from the CL gas pores into the ionomer or will be desorbed from the ionomer into the CL gas pores. The equilibrium sorption isotherm is given by Liu [74]:

$$\lambda_{eq} = \left[1 + 0.2352 a_w^2 \frac{T(^\circ C) - 30}{30}\right] (14.22 a_w^3 - 18.92 a_w^2 + 13.41 a_w) \tag{3.28}$$

where a_w is the activity of the water vapor in the CL and is given by:

$$a_w = \frac{p_{H_2O}}{p_{sat}} = RH \tag{3.29}$$

p_{H_2O} is the partial of the water vapor at the ionomer/CL interface and is obtained with the multiplication of the mole fraction of the water vapor by the cell pressure. The water saturation pressure is temperature-dependent and is provided by Springer et al. [50] as:

$$log_{10}(p_{sat}) = -2.1794 + 0.02953 T_{cell} - 9.1837 \times 10^{-5} T_{cell}^2 + 1.4454 \times 10^{-7} T_{cell}^3 \tag{3.30}$$

A difference between the equilibrium water content and the local membrane water content will result in water absorption/desorption. The sorption rate, S_λ is given by:

$$S_\lambda = k_\lambda \frac{\rho_{m,dry}}{EW} (\lambda_{eq} - \lambda) \tag{3.31}$$

where the rate constant k_λ is set to 100000 to ensure a strong coupling between the CL and ionomer.

The final system of equations solved in this work can be written as:

$$\begin{aligned}
\nabla \cdot (c_g D^{eff}_{O_2,N_2} \nabla x_{O_2}) &= \frac{1}{4F} \nabla \cdot \mathbf{i} \\
\nabla \cdot (c_g D^{eff}_{H_2O,N_2} \nabla x_{H_2O}) &= -\frac{1}{2F} \nabla \cdot \mathbf{i} + k_\lambda \frac{\rho_{m,dry}}{EW} (\lambda_{eq} - \lambda) \\
\nabla \cdot \left(\frac{\sigma^{eff}_m}{F} \nabla \phi_m \right) &= \frac{1}{F} \nabla \cdot \mathbf{i} \\
\nabla \cdot \left(\frac{\sigma^{eff}_s}{F} \nabla \phi_s \right) &= -\frac{1}{F} \nabla \cdot \mathbf{i} \\
\nabla \cdot \left(n_{drag} \frac{\sigma^{eff}_m}{F} \nabla \phi_m + D_\lambda \frac{\rho_{m,dry}}{EW} \nabla \lambda \right) &= -k_\lambda \frac{\rho_{m,dry}}{EW} (\lambda_{eq} - \lambda)
\end{aligned} \tag{3.32}$$

3.2.4 Layer Properties

The effective properties that are used as the coefficients to the Laplacian equations in equations (3.32) are properties of the layers that comprise the fuel cell. The first four equations are solved in different layers, each having different composition and structure. Note that in this work, the layers in both the anode and cathode side are assumed to have the same composition and structure, so any effective properties will apply to both sides.

Figure 3.2 shows the micro-structure of each of the layers. The gas diffusion layers must transport gaseous species and electrons. They are assumed to be composed of a network of carbon fibers, arranged in a random anisotropic manner. The carbon fibers allow for the transport of electrons, while the space between the fibers (i.e. the pore space) allows for the transport of gaseous species. The micro-porous layers also transport gaseous species and electrons. Their structure is assumed to be composed of an random isotropic arrangement of carbon particles bound with PTFE. The carbon particles allow for the transport of electrons, while the pore space transports the gaseous species. The catalyst layer must transport gaseous species, electrons and protons. Similarly to the MPL, the CL is composed of carbon particles and pore spaces. However, ionomer (usually Nafion) is added to allow for the transport of protons. The membrane is assumed to be composed of a solid polymer-electrolyte (usually Nafion) which allows for the transport of protons and also absorbs water in liquid form.

In the presence of the ionomer and a solvent, the carbon particles agglomerate into a network of spherical agglomerates as shown in Figure 3.2. The agglomerate model of the catalyst layer is an active area of research [61, 75, 76]; however, it adds additional complexity to the model. For this work, each layer is assumed to be macro-homogeneous, i.e. they can be characterized by averaged quantities across the layer. This assumption does not, therefore, take into account the micro-structure of the layers.

Each layer, besides the membrane, is assumed to be a porous media. Due to the macro-homogeneous assumption for each of the layers, they can be characterized by the volume fractions of each of the phases that compose the layer. The GDL is constructed from a matrix of carbon fibers, with pore space between the fibers. Two distinct phases are present: pore space and solid phase. The porosity (or pore volume fraction) of the layer is defined as the fraction by volume of the pore space to the total volume of the layer. The remaining volume fraction accounts for the solid phase. A similar analysis can be used for the MPL. The CL is composed of pore space, the electrolyte and the carbon particles. Therefore, three volume fractions need to be considered. The GDL and MPL porosity is typically given by the manufacturer. The solid volume fraction can be found using $\epsilon_S = 1 - \epsilon_V$, where ϵ_S and ϵ_V is the volume fraction of the solid and the porosity respectively.

The CL volume fractions can be computed with the knowledge of the composition of the ink that was used to create the layer. The CL is typically made by preparing an ink that contains carbon particles coated with platinum, ionomer and a solvent. This ink can then be painted onto a membrane in a layer typically 10-20 microns thick. The ink composition is commonly reported based on the mass of the catalyst,

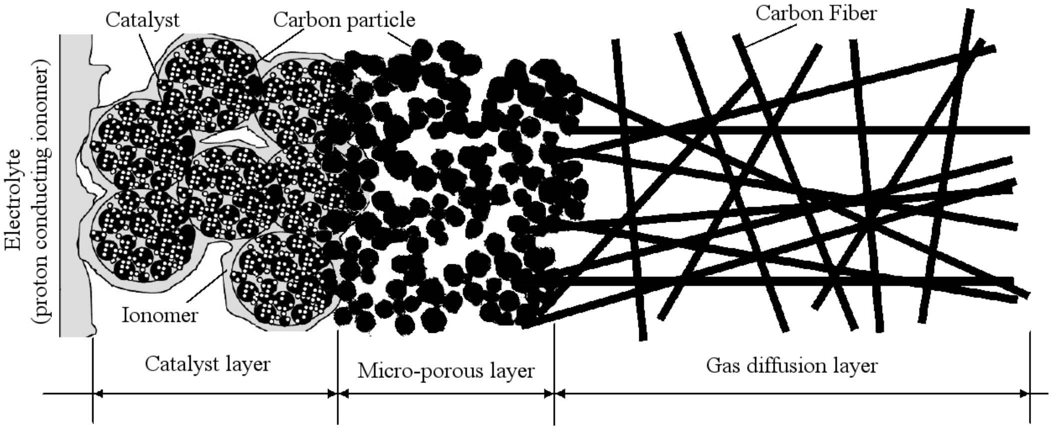

Figure 3.2: The micro-structure of each of the layers in the MEA.

carbon and ionomer used. The mass of carbon used in the layer is reported as a percentage of the platinum mass and is denoted $Pt|C$.

The volume fraction of the solid phase can be computed using [77]

$$\epsilon_S = \left(\frac{1}{\rho_{Pt}} + \frac{1 - Pt/C}{Pt/C \rho_c} \right) V_{Pt} \tag{3.33}$$

where ρ_{Pt} and ρ_c are the densities of the carbon and the platinum respectively. The volume fraction of the ionomer can be determined with knowledge of its mass fraction, X_N. The ionomer fraction is computed using

$$\epsilon_N = \frac{X_N}{\rho_{N,dry}(1 - X_N)} \frac{1}{Pt/C} V_{Pt} \tag{3.34}$$

where $\rho_{N,dry}$ is the density of the dry ionomer. The remaining volume fraction will be porosity of the layer and is given by

$$\epsilon_V = 1 - (\epsilon_S + \epsilon_N) \tag{3.35}$$

With the volume fraction defined, the equation coefficients can be scaled to account for the reduced volume in which the species can be transported. The most commonly used method for computing effective properties is the Bruggemann relation given by

$$D^{eff} = \epsilon^{1.5} D \tag{3.36}$$

where D^{eff} is the effective property of the layer, D is any bulk property (examples include diffusion coefficients, the conductivity of bulk ionomer or bulk carbon) and ϵ is the volume fraction of the phase in which the species is being transported.

One of the weakness of the Bruggemann relation is that transport will occur even for very low volume fractions. Percolation theory can also be used to account for layer porosity and tortuosity. Percolation theory states that there exists a volume fraction below which the species transport will not occur. An extreme example is considering the flow of gas through a porous material with a porosity of 1%. Gas transport will not occur unless the very small pore space forms a continuous network through the material, which is highly unlikely for such a small porosity in a random and homogeneous material. The Percolation equation is written as:

$$D^{eff} = D \left(\frac{\epsilon - \epsilon^{th}}{1 - \epsilon^{th}} \right)^{\mu} \Theta(\epsilon - \epsilon^{th}) \tag{3.37}$$

where D is any bulk property, ϵ^{th} is the threshold volume fraction below which transport will not occur and μ is the network constant that accounts for the characteristic shape of the curve described by the equation. The Heaviside function is used to enforce that transport will not occur below the threshold value:

$$\Theta(\epsilon - \epsilon^{th}) = \begin{cases} 0 \text{ for } (\epsilon - \epsilon^{th}) < 0 \\ 1 \text{ for } (\epsilon - \epsilon^{th}) \geq 0 \end{cases} \tag{3.38}$$

The 'effectiveness' of a layer can be defined with the specification of the threshold volume fraction and the network constant. These values are generally found from fitting to experimental data.

3.2.4.1 Gas Diffusion Layer

The GDL is considered an anisotropic layer, as the stacking arrangement of the fibers results in large pores in the through-plane direction, facilitating gas transport but impeding electron transport, as electrons must jump between fibers. Electron transport is improved in the in-plane direction, as the electrons can move along individual fibers. Gas transport is impeded however. To account for anisotropic gas transport in the GDL, Tomadakis et al. [78] used an equation similar to percolation:

$$D^{eff}_{O_2,i} = D_{O_2}\epsilon \left(\frac{\epsilon - \epsilon^{th}}{1 - \epsilon^{th}}\right)^{\mu^i} \Theta(\epsilon - \epsilon^{th}) \tag{3.39}$$

where the subscript i denotes the in-plane or through-plane direction. Tomadakis performed numerical simulations of overlapping fibers and found values of 0.118 for the percolation threshold and 0.785 and 0.521 for the network constant in the through- and in-plane respectively. Again, bulk diffusion coefficients are computed using Chapman-Enskog theory, which will also be used in the MPL and CL. Electron transport has not been extensively studied to date due to the relatively small losses incurred. Secanell [68] fit a Bruggemann type relation to experimental data provided by Toray for the TGP-H series GDLs. Bulk values of $16.02 S/cm$ and $272.78 S/cm$ were found along with exponentials of 1.0 and 1.5 for the in- and through-plane respectively.

3.2.4.2 Micro-Porous Layer

The MPL is a random isotropic arrangement of carbon particles, so in- and through-plane values are not needed. Here, the bulk conductivity of the solid phase is given by that of the carbon particles, which is given as $88.9 S/cm$. Values of 0.118 and 2.0 are used for the threshold volume fraction and network constant respectively for both pore and solid phases. Due to the similar composition and structure of the MPL to the CL, these values were taken from the fit to experimental data performed by Secanell [68] to packed carbon black particles.

3.2.4.3 Catalyst Layer

The CL is also a random isotropic arrangement of carbon particles, however the volume fraction of ionomer must also be considered. To find the effective transport properties of oxygen in the CL, Dobson [69] fit the percolation equation to experimental data provided by Yu and Carter [79]. A threshold value of 0.3 and 4.0 was found.

When considering the transport of the reactants to the reactions sites, it is assumed that the reaction sites are covered with an infinitely thin layer of ionomer. The dissolution of oxygen into the ionomer is governed by Henry's Law. The partial pressure of the reactant at the pore/ionomer interface will determine the concentration of the reactant in the ionomer. For example for the cathode side:

$$c_{O_2} = \frac{x_{O_2}(c_g RT)}{H_{O_2,N}} \tag{3.40}$$

where c_{O_2} is the oxygen concentration at the reaction site, which is used in the equations (3.22) and (3.24) to compute the current density. c_g is the total species concentration in the cathode, its multiplication by the molar fraction and the gas constant times the temperature will give the partial pressure for oxygen at the ionomer/pore space interface. Henry's constant is denoted $H_{O_2,N}$, which controls the dissolution rate of the gas into the ionomer. The oxygen also has to diffuse through the ionomer film to the reaction site. In this work, it is assumed that the film is infinitesimally thin so the diffusion of oxygen in Nafion is not accounted for. The same analysis is used for the anode side, where here hydrogen is the reactant. This will result in a different value for Henry's constant.

Data for the conductivity of the electrolyte phase was taken from Iden et al. [80, 81]. To measure the proton conductivity in a CL, two MEA samples were prepared. The first was a standard MEA, however it was manufactured by the decal transfer of a catalyst layer onto one side of a membrane. This was repeated, and the two half catalyst coated membranes (CCM) were then hot pressed together. The reason for this unusual manufacturing technique was that the second sample included a pseudo-catalyst layer (PCL) in between the two CCMs. The PCL was made in the same manner as the anode and cathode, however no platinum was used in its manufacture. It was not electrochemically active, however it still shared the same structure and composition of the actual catalyst layers. By comparing the ohmic losses in each of the samples, the effective proton conductivity of the PCL could

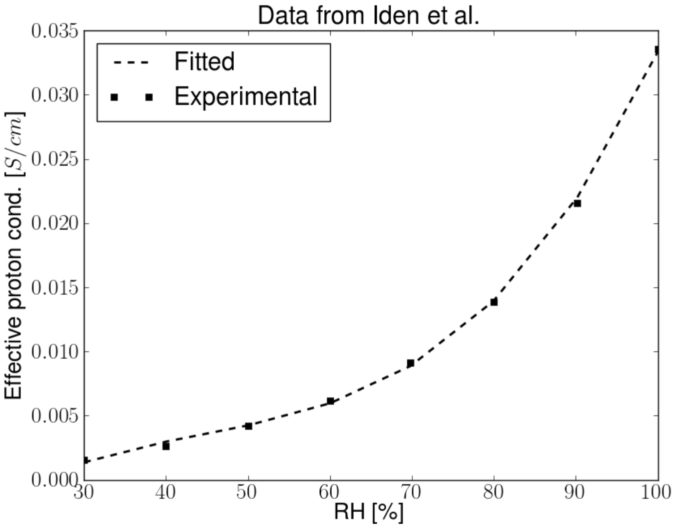

Figure 3.3: Fit to experimental data provided by Iden et al. [80].

be determined at different RH conditions. In this work, a third order polynomial expression for the effective proton conductivity with respect to the relative humidity was used to fit the experimental data from Iden [80] in order to estimate the effective proton conductivity

$$\sigma_m^{eff} = 1.329\times10^{-7}RH^3 - 1.767\times10^{-5}RH^2 + 9.058\times10^{-4}RH - 1.349\times10^{-2} \quad (3.41)$$

Note that this value was found at a constant temperature of 80℃ and an ionomer volume fraction of 0.19. Values in the area of 0.19 for the ionomer volume fraction are typically found in catalyst layers. It is assumed that any deviation from ionomer loading should be minor. Figure 3.3 shows the fit between the experimental effective values and those computed using equation 3.41. The parameters used in the MPL for electron conductivity are also used in the CL.

3.2.4.4 Membrane

Finally, while the membrane is not a porous media, some properties of the layer need to be specified. A temperature and water content dependent fit to membrane bulk conductivity was performed by Dobson [69], using data for an NRE211 membrane taken from BekkTech LLC [82]:

$$\sigma_m = (0.020634 + 0.01052\lambda - 1.0125\times10^{-4}\lambda^2)\exp\left(752\left(\frac{1}{T_0} - \frac{1}{T}\right)\right) \quad (3.42)$$

where $T_0 = 30^oC$.

The diffusion coefficient of liquid water in the membrane is provided by Motupally et al. [83] which depend on the water content and cell temperature.

$$D_\lambda = \begin{cases} D_{H_2O} = 3.10 \times 10^{-3}\lambda(-1 + e^{0.28\lambda})\text{exp}\left(\dfrac{-2436.0}{T}\right) & \text{if} \quad 0 < \lambda \leq 3 \\ D_{H_2O} = 4.17 \times 10^{-4}\lambda(1 + 161e^{-\lambda})\text{exp}\left(\dfrac{-2436.0}{T}\right) & \text{if} \quad 3 < \lambda \leq 17 \end{cases} \tag{3.43}$$

3.2.5 Solution method

The system of partial differential equations in (3.32) characterizes the physical phenomena occurring in a fuel cell under operation. The system is highly nonlinear due to the current density source term so the system will be solved numerically using an iterative method. The method used in this work is Newton's method, where the system of equations is linearized about a perturbation in the solution variables. The generic formulation for Newton's method is given as:

$$\frac{\partial R(u^n)}{\partial u}(-\delta u) = [R(u^n)] \tag{3.44}$$

where $R(u^n)$ denotes the system of equations given in equations (3.32) which depend on the solution variables u. n denotes the step of the iterative solver, while δu is the perturbation on the solution variables. Taking a Laplace equation as an example (each of the governing equations are Laplacians):

$$R(u^n) = \nabla \cdot (k\nabla u^n) - f(u^n) = 0 \tag{3.45}$$

Perturbing the equation and then performing a Taylor series expansion:

$$R(u^{n+1}) = R(u^n + \delta u) = R(u^n) + \left.\frac{\partial R}{\partial u_i}\right|_{u=u^n} \delta u_i + O(\delta u_i^2) \tag{3.46}$$

where the $\frac{\partial R}{\partial u_i}$ is the Jacobian of the residual, i.e. its derivative with respect to each of the solution variables. The second term is the variation of the residual $R(u)$ and is given by:

$$\frac{\partial R}{\partial u}\delta u = \nabla \cdot (k\nabla \delta u) - \left.\frac{\partial f(u)}{\partial u_i}\right|_{u=u^n} \delta u_i \tag{3.47}$$

This assumes that the coefficient k does not depend on the solution variables, as is the case in the majority of the governing equations being solved in this work. The objective of an iterative solver is to drive the residual to zero i.e. $R(u^{n+1}) = 0$. Therefore, the final equation will take the form:

$$\nabla \cdot (k\nabla \delta u) - \left.\frac{\partial f(u)}{\partial u_i}\right|_{u=u^n} \delta u_i = \nabla \cdot (k\nabla u^n) - f(u^n) \tag{3.48}$$

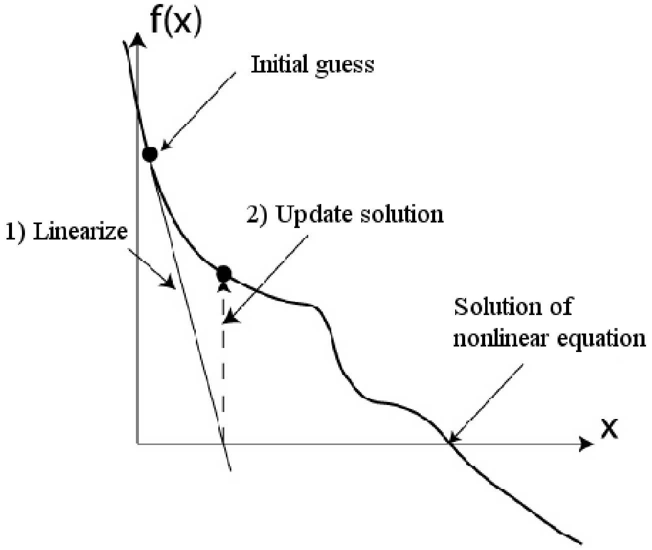

Figure 3.4: Graphical representation of Newtons method.

This system of equations is linear in terms of δu and so can be solved using a PDE solver.

An initial solution u_0 is required, about which the initial linearization can be applied. Equation (3.48) is then solved to find the solution perturbation δu. The solution can then be updated according to:

$$u^{n+1} = u^n + \delta u \tag{3.49}$$

The system is linearized about the updated solution and the process is repeated until convergence is achieved. This is shown graphically in Figure 3.4.

Equation (3.48) represents a system of linear equations. To solve this system of PDEs, the finite element method is used. Using this method, the domain of interest is broken into elements over which the system of equations are solved individually. An example of a grid used in this work is shown in Figure 3.5, where each quadrilateral represents a single element. In this work, a Bubnov-Galerkin method is used to obtain the weak form of the equations and continuous, second order Lagrange elements are used. The integrals over each element are evaluated using Gauss-Legendre quadrature. The system matrix and right hand side vectors can then be evaluated for each element, and because neighboring elements will share the same nodes, a global system matrix and right hand side vector will need to be assembled. The solution to the global system matrix will ultimately return the solution perturbation δu, which is then returned to the Newton solver which will update the solution and linearize the system of equations again.

Once the Newton solver has converged, the mesh is refined to achieve a grid independent solution. Adaptive refinement is used, where the refinement occurs only in the cells that are producing the largest error. This is in contrast to global methods, where the entire grid is refined equally. A single refinement will refine the 30% of cells that have the highest error and will coarsen 3% of cells that produce the smallest error. Refinement to a single cell will generate four additional cells, so a single adaptive refinement will roughly double the number of cells. However, they will be localized in the area of greatest error (typically where the gradients are steepest), the equivalent localized refinement achieved using global refinement will result in significantly more cells. The error estimator is provided by Kelly et al. [84].

The solver for the global system matrix is the direct solver UMFPACK [85]. A direct solver is needed as the system of equations will be unsymmetric due to the Jacobian of the source term, so iterative solvers such as the conjugate gradient method cannot be used. Finite element information is provided by the deal.II (Differential Equations Analysis Library) libraries [86, 87]. The libraries provide the implementation of the direct solver, handlers for the grid, finite elements and the degrees of freedom, as well as adaptive refinement capability and the post-processing routines. The FCST (Fuel Cell Simulation Toolbox) code [68] provides the local system and RHS vector assembly, as well as libraries describing physical phenomena and properties commonly found in fuel cells. The FCST code is an open-source in-house code that provides interfaces to the deal.II libraries and the DAKOTA optimization libraries.

3.2.5.1 Boundary conditions

Figure 3.5 shows an example mesh used to discretize the computational domain. Note that the domain includes only half of one of the current collectors and half of one of the gas channels. An actual fuel cell will have several channels, and therefore current collectors, in parallel in the in-plane direction. This model takes into account the symmetry of the computational domain about the top and bottom surfaces as is shown in Figure 3.1. There are six boundaries to be considered in this model. The top two boundaries are symmetric boundaries, hence a no-flux boundary is applied to each of the equations. The other four boundaries represent the location of the

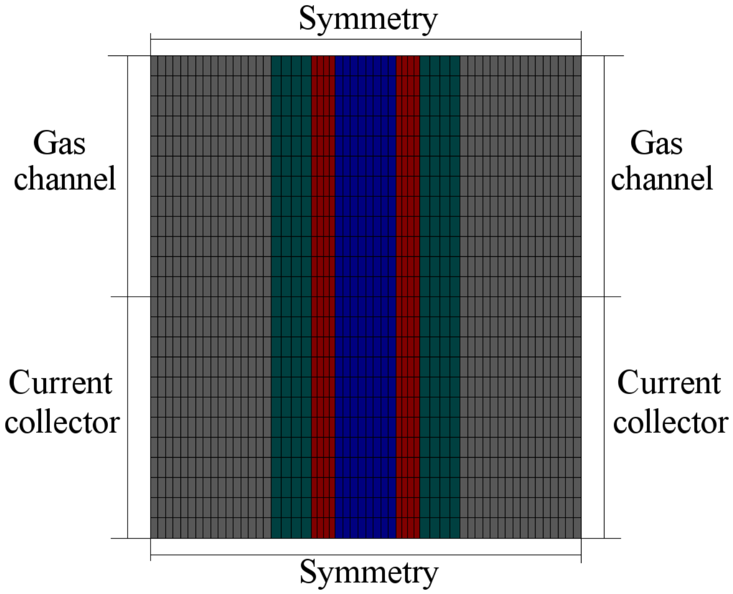

Figure 3.5: Grid used to discretize the computational domain.

gas channel, where the reactants are provided, and the current collector, where the electrons are provided.

At both of the current collectors, a Dirichlet boundary condition is imposed on the solid phase potential solution variable, while Neumann conditions are applied to the others. Each of the boundaries fluxes are set to zero, representing zero flux through the surface. The solid phase potential is set to zero on the anode side of the cell, while a potential of $\phi_s = V_{cell}$ is applied to the cathode side. V_{cell} represented the voltage difference across the cell, i.e. the operating voltage. From this voltage, the resulting current is computed by the model and the performance of the cell can be investigated.

At both of the gas channels, a Dirichlet boundary condition is imposed on the gaseous species solution variables, while Neumann conditions are applied to the others. Again, each of the boundaries fluxes are set to zero. At the cathode side, the oxygen mole fraction solution variable is set to to $x^0_{O_2}$, while at the anode side, the water vapor mole fraction solution variable is set to to $x^0_{H_2O}$. These values are computed based on the operating conditions of the cell. In particular, they will depend of the pressure and relative humidity at which the anode and cathode gases are provided, as well as the cell temperature. The oxygen mole fraction is computed on the assumption that it is delivered in air, where its fractional content is at 21%.

Table 3.2: GDL, MPL and CL structural and composition properties

Parameter	**Value**
Structural dimensions	
CCL thickness, $[cm]$	1×10^{-3}
CMPL thickness, $[cm]$	5×10^{-3}
CGDL thickness, $[cm]$	2.5×10^{-2}
Membrane thickness, $[cm]$	2.5×10^{-3}
AGDL thickness, $[cm]$	2.5×10^{-2}
AMPL thickness, $[cm]$	5×10^{-3}
ACL thickness, $[cm]$	1×10^{-3}
Current collector width, $[cm]$	0.1
Channel width, $[cm]$	0.1
Layer Composition	
GDL porosity	0.6
MPL porosity	0.4
Percentage platinum by weight	0.46
Platinum loading per unit volume, $[\frac{mg}{cm^3}]$	400
Electrolyte loading	0.3

3.2.6 Input Parameters

The input parameters are described in this section. The input parameters described here are taken from references [68, 69] and are chosen so that they describe a realistic fuel cell MEA operating under typical operating conditions. The model is accurate enough that the results can be compared to experimental data. Table 3.2 gives the structural parameters for each of the layers that comprise the cell. In particular the dimensions of the layers are given, as well as their composition.

The properties of the materials that the layers are composed from are described in Table 3.4, while the parameters used to determine the effective properties of the layers are given in Table 3.3. Finally the operating conditions for the model are given in Table 3.5. The parameters given in these tables describe the base case.

3.3 Results and Discussion

3.3.1 Base Case

This section will compare the results from an MEA simulation, using the input parameters in Tables 3.2 to 3.5, with three different ORR kinetic models in the cathode catalyst layer. The first source term uses the commonly used Tafel kinetic model based on parameters taken from the experimental data presented by Parthasarathy

Table 3.3: GDL, MPL and CL transport properties

Parameter	**Value**
Structural dimensions	
Gas transport properties	
GDL porosity threshold	0.11
GDL porosity network const.	0.785
MPL porosity threshold	0.118
MPL porosity const.	2
CL porosity threshold	0.3
CL porosity network const.	4
Solid transport properties	
GDL solid threshold X	0.0
GDL solid network const.	1.5
GDL solid threshold X	0.0
GDL solid network const.	1.0
MPL solid threshold	0.118
MPL solid const.	2
CL solid threshold	0.118
CL solid network const.	2
Ionomer transport properties	
CL effect. ionomer transport	Experimental data [80]

et al. [31, 32]. A transfer coefficient of one is commonly used in the literature [57, 60, 61], giving a constant Tafel slope of approximately 70mV/dec over the entire potential range at a temperature of 80°C. The second model (denoted Wangs parameters in the figures) is the double-trap kinetic model developed by Wang et al. using the kinetic parameters provided by Wang et al. [48]. The final source term (denoted This work) will be the double-trap kinetic model using the kinetic parameters fitted in this work to the experimental data provided by Parthasarathy et al.

Figure 3.6 shows the obtained polarization curves using each of the kinetic models. The drop in performance from the doubling of the Tafel slope is evident in the curve from this work. In the high overpotential region, the current density is significantly lower than that returned by the Tafel kinetic model. As expected, the low overpotential regions are quite similar. The Tafel kinetic model takes its parameters from the experimental data given by Parthasarathy et al. in the low overpotential region. The fitted parameters for the double trap model were fitted to the same data and the errors found when reproducing the kinetic data were small in the low overpotential region. The double-trap model actually out-performs the Tafel model

Table 3.4: Material properties

Parameter	**Value**
Nafion 1100	
$H_{O_2,N}$, $[Pa \cdot cm^3 \cdot mol^{-1}]$	3.1664×10^{10}
$D_{O_2,N}$, $[cm^2 \cdot s^{-1}]$	9.726×10^{-10}
$H_{H_2,N}$, $[Pa \cdot cm^3 \cdot mol^{-1}]$	6.94×10^{10}
$D_{H_2,N}$, $[cm^2 \cdot s^{-1}]$	12.8×10^{-10}
Equivalent weight, $[g \cdot mol^{-1}]$	1100
Dry membrane density, $[g \cdot cm^{-3}]$	2.0
Water sorption time const., $[s^{-1}]$	10000
Platinum	
Cathodic transfer coefficient (Tafel)	1
Oxygen reaction order (Tafel)	1
Exchange current density (Tafel), $[A \cdot cm^{-2}]$	2.47×10^{-8}
Reference O_2 conc. (Tafel), $[mol \cdot cm^{-3}]$	7.25×10^{-6}
Reference O_2 conc. (Double-Trap), $[mol \cdot cm^{-3}]$	3.36×10^{-6}
Anodic potential range const. (Dual-Path)	1.2
Reference H_2 conc. (HOR), $[mol \cdot cm^{-3}]$	0.59×10^{-6}
Exchange current density OH, $[A \cdot cm^{-2}]$	0.01
Exchange current density OT, $[A \cdot cm^{-2}]$	0.47
Carbon	
Particle electrical conductivity, $[S \cdot cm^{-1}]$	88.9
Fiber electrical conductivity X, $[S \cdot cm^{-1}]$	16.03
Fiber electrical conductivity Y, $[S \cdot cm^{-1}]$	272.78
Density, $[g \cdot cm^{-3}]$	2

Table 3.5: Operating conditions

Parameter	**Value**
Input conditions	
Cell temperature, $[K]$	353
Cathode pressure, $[Pa]$	101325
Cathode relative humidity	0.7
Anode pressure, $[Pa]$	101325
Anode relative humidity	0.7

in this region, as the experimental Tafel slopes were slightly less than the 70mV/dec used in the Tafel model. The small gains here are quickly lost with the change in Tafel slope however.

By contrast, the double-trap model with the parameters taken from Wang et al. predict a higher overall performance than that shown by the Tafel model. These parameters returned significant errors in the low overpotential region when compared to the data from Parthasarathy et al. The lower Tafel slope returned in this region results in significantly higher performance over Tafel kinetics. The curve then falls to meet the Tafel curve, as the doubling of the Tafel slope begins to reduce the double-trap model performance. The limiting current is reached before the two curves crossover however.

Figure 3.7 shows a Tafel plot for each of the cases over the potential range. The match in the Tafel slopes between the Tafel model and the fitted parameters is clear in the low overpotential region, while the smaller Tafel slope of the Wang's parameters curve causes the higher performance. At currents of approximately 10^0

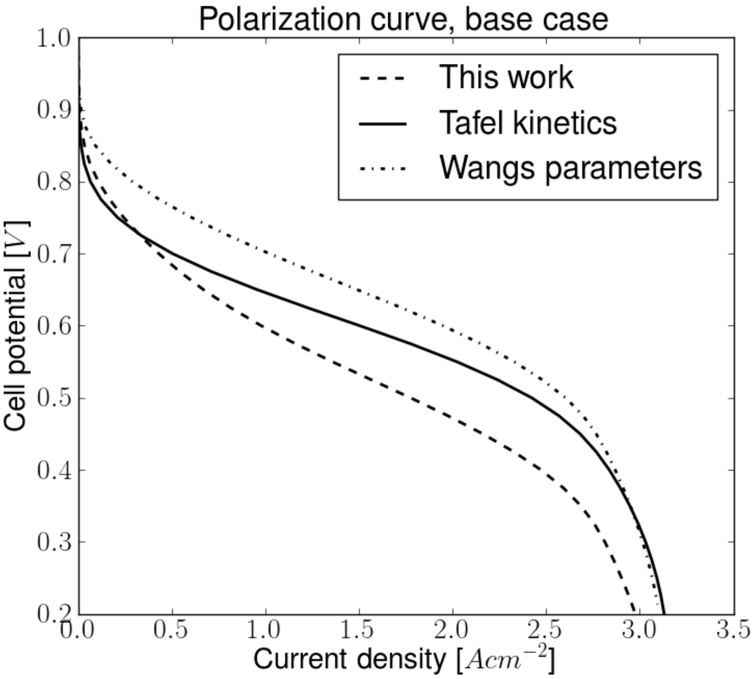

Figure 3.6: Polarization curve for the base case using three source terms. The solid line is the results from using Tafel kinetics. The double-trap model with Wang's parameters are shown in fine dash, while the dashed line uses the parameters from this work.

($1Acm^{-2}$), the Tafel slope changes for the double-trap model causing the drop in performance, as evidenced in the deviation from the linear slope. Other effects such as ohmic losses in the membrane and oxygen depletion cause further changes in slope, which is also seen in the Tafel kinetics curve.

The exchange current density for the double-trap model is not specified as an input parameter, as is the case in the Tafel kinetic model. However, its value can be found with extrapolation of the curve back to the open cell potential, which is $1.16V$ for the operating conditions used in the base case. It can be seen that using Wang's parameters will result in an exchange current density that is over an order of magnitude smaller than the other curves. However, the model quickly overtakes the other curves due to its smaller Tafel slope. This shows the importance of accurately capturing the low overpotential region. The region exists over several decades of current density so a small differences in Tafel slope (units of mV/dec) can have major effects in the performance of the overall model, as seen in the significant difference between Wang's parameters and parameters from this work. By contrast, upper Tafel slope is seen only over a single decade of current production and occurs

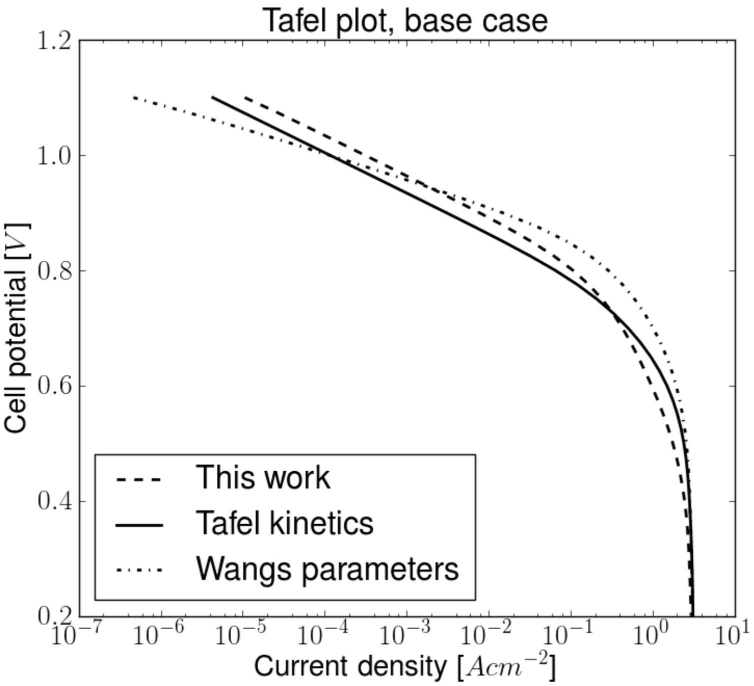

Figure 3.7: Tafel plot for the base case using three source terms. The solid line is the results from using Tafel kinetics. The double-trap model with Wang's parameters are shown in fine dash, while the dashed line uses the parameters from this work.

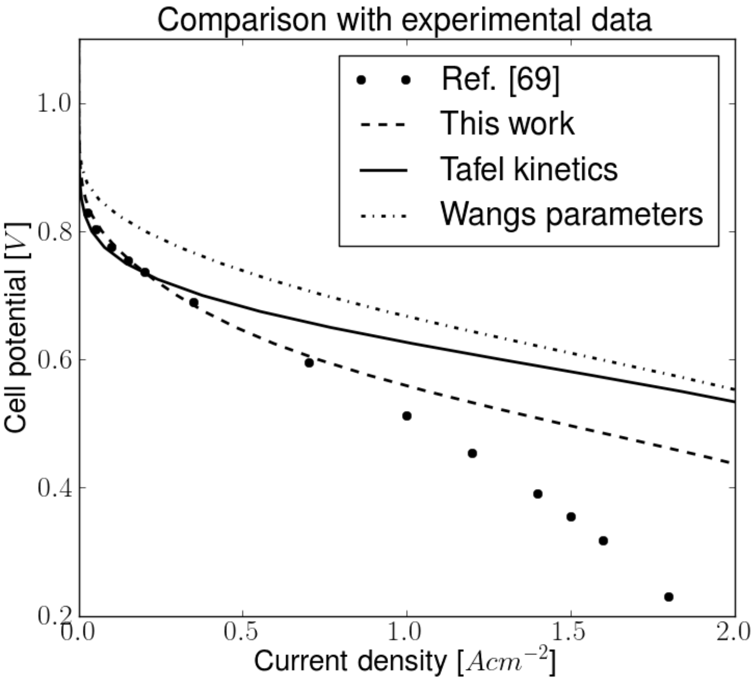

Figure 3.8: Comparison between the three kinetic models and example experimental data. Points represent the experimental data, while the solid line is the results from Tafel kinetic model. The dashed line is the results from the double model model using parameters from this work, while the dash-dot line uses parameters from Wang et al.

in the area where other losses are also significant. Using the base case with the source term from this work as an example, the predicted exchange current density is of the order of 1×10^{-6}. At a cell potential of 0.8V (where the change in Tafel slope occurs), the current produced is of the order of 1×10^{-1}, leading to the low Tafel slope being applied over 5 decades of current density. At a cell potential of 0.2V, the computed current is of the order of 1×10^{0} (the current is approximately 3A/cm^2). The upper Tafel slope is therefore applied only over a single decade of current. As a further example, if the lower Tafel slope was 70mV/dec instead of 60mV/dec and the upper Tafel slope was 140mV/dec instead of 120mV/dec, then the percentage error in both regions for the Tafel slopes are the same. However, the lcd region will overpredict the losses by a total 50mV, while the hcd region losses are only overpredicted by 20mV. Hence, a better approximation of the lcd Tafel slope is preferred.

A final comparison between the double-trap model with Wang's parameters and the fitted parameters from this work can be made against experimental data. Figure

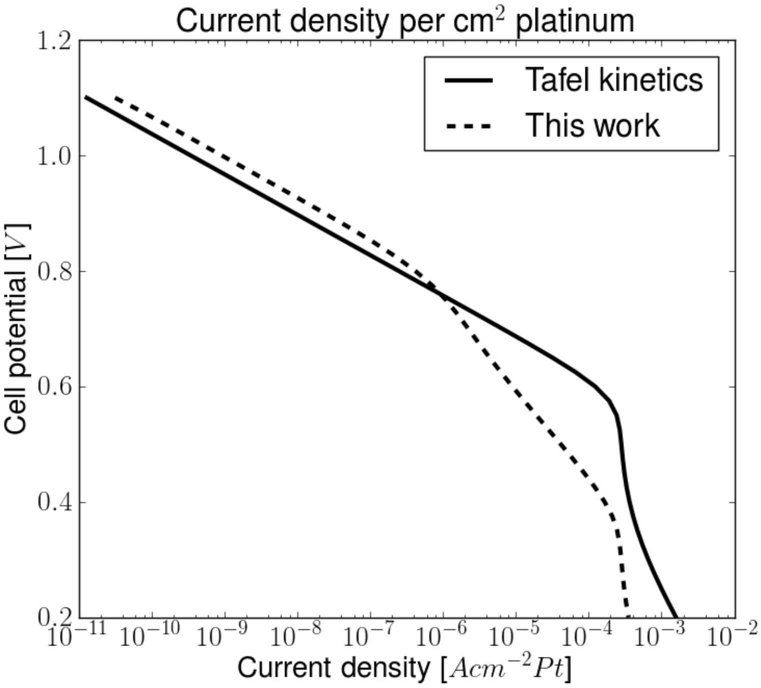

Figure 3.9: Tafel plot showing the current density per cm^2 platinum surface. The dashed line is the results from using the Tafel kinetic model, while the solid line is the double-trap model with the fitted parameters from this work.

3.8 compares the results from each of the source terms to experimental data provided by NRC-IFCI [69] (see Section 3.3.2.1). The resulting polarization curves show that the closest match is to the double trap kinetic model with the parameters from this work. The experimental data shows significant kinetic losses, with the ohmic losses only becoming significant at a cell potential of approximately $0.7V$ (the kinetic region is characterized by the exponential shape at the start of the curve, whereas the ohmic losses take a linear form in the middle region). The parameters from Wang et al. have low kinetic losses in the low overpotential region, while the Tafel model does not have the increased kinetic losses in the high overpotential region so neither can match the losses in the kinetic region. The ohmic region for both of these source terms becomes significant at a higher cell potential (compared to the source term from this work) of approximately $0.8V$ leading to high overall performance. Further discussion on the comparison with experimental data is presented in section 3.3.2.1. Figure 3.8 shows that the kinetic parameters from this work better fit the experimental data compared to the parameters from Wang et al. so Wang's parameters will not be considered for rest of this work.

The reduced performance predicted by the double-trap kinetic model is due to the increase in Tafel slope at high overpotentials. This results in the need for greater overpotentials to produce the same amount of current in comparison to Tafel kinetics. This is shown in Figure 3.9, which shows the current density per centimeter squared of platinum surface. This can be considered the 'effectiveness' of the platinum at completing the ORR, i.e. how much current density each centimeter squared of platinum can produce. In the low overpotential region, both models have a similar performance. In the high overpotential region, the double trap model shows a significant drop in performance. If both models were producing the same amount of current, e.g. $10^{-4} Acm^{-2} Pt$ (corresponding to approximately $2Acm^{-2} CL$), the double trap model would need a greater amount of platinum surface to produce the current at the same overpotential.

The differences in the effectiveness can also been seen with the investigation of the profiles of the solution variables and current density across the CCL. Figures 3.10 and 3.11 shows the solution profiles for the oxygen and water vapor molar fraction, overpotential, membrane water content and current density in the CCL for the double trap model and the Tafel kinetic model respectively. The intermediate species are also shown for the double trap model. The profiles are taken at constant current densities of $0.07A\ cm^{-2}$, $1A\ cm^{-2}$ and $3A\ cm^{-2}$, taking from Figure 3.8. The first current density is in the low overpotential region where kinetic losses are the most significant. The second is in the high overpotential region, where ohmic losses dominate. The third is in the high overpotential region where oxygen depletion is responsible for the loss in performance.

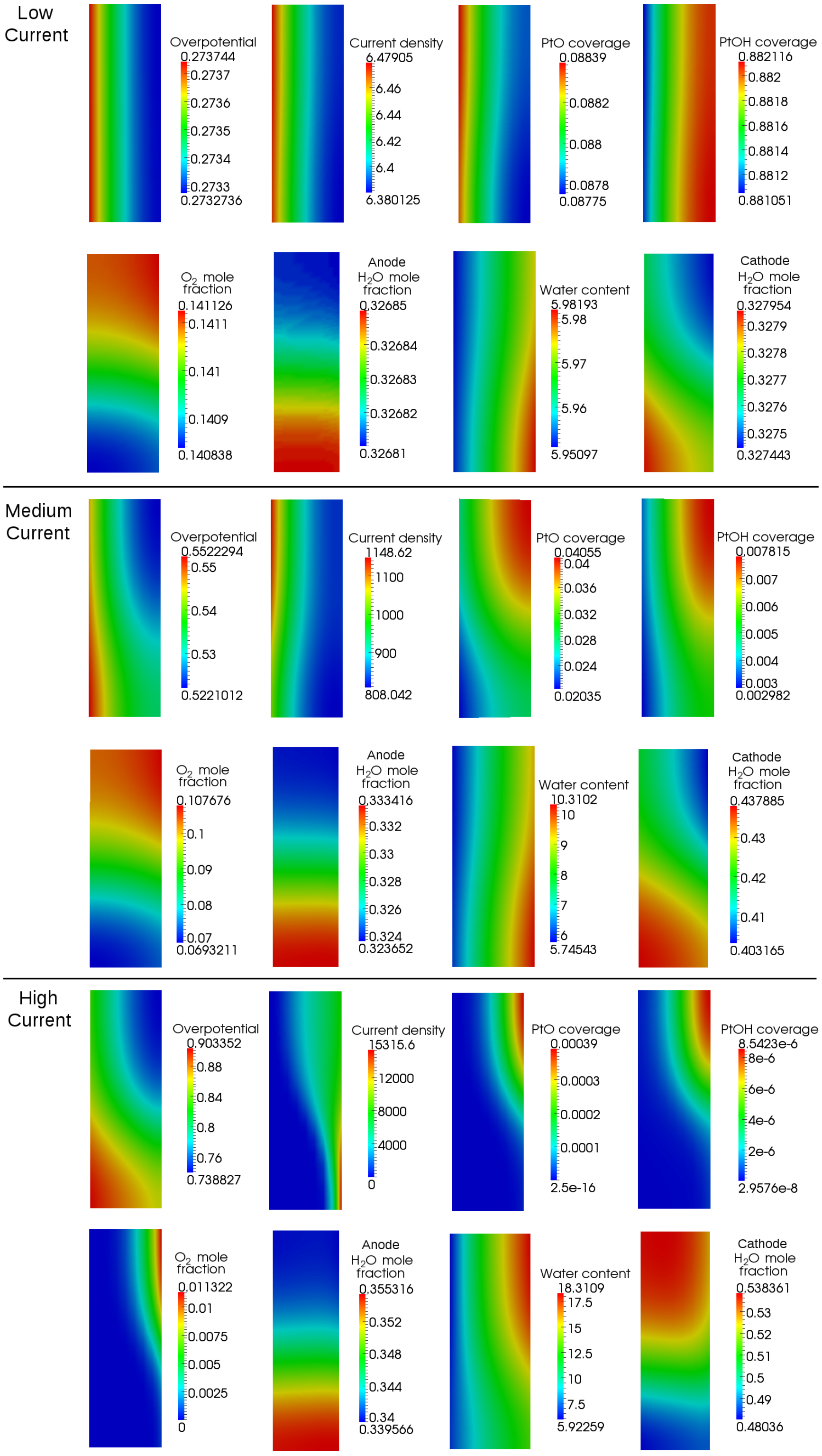

Figure 3.10: Profiles of the oxygen and water vapor molar fraction, overpotential, membrane water content, current density and intermediate solution profiles for the double trap model using the fitted parameters. The top profiles are for a current density of $0.07 A\ cm^{-2}$, the middle is at $1 A\ cm^{-2}$ and the bottom is $3 A\ cm^{-2}$.

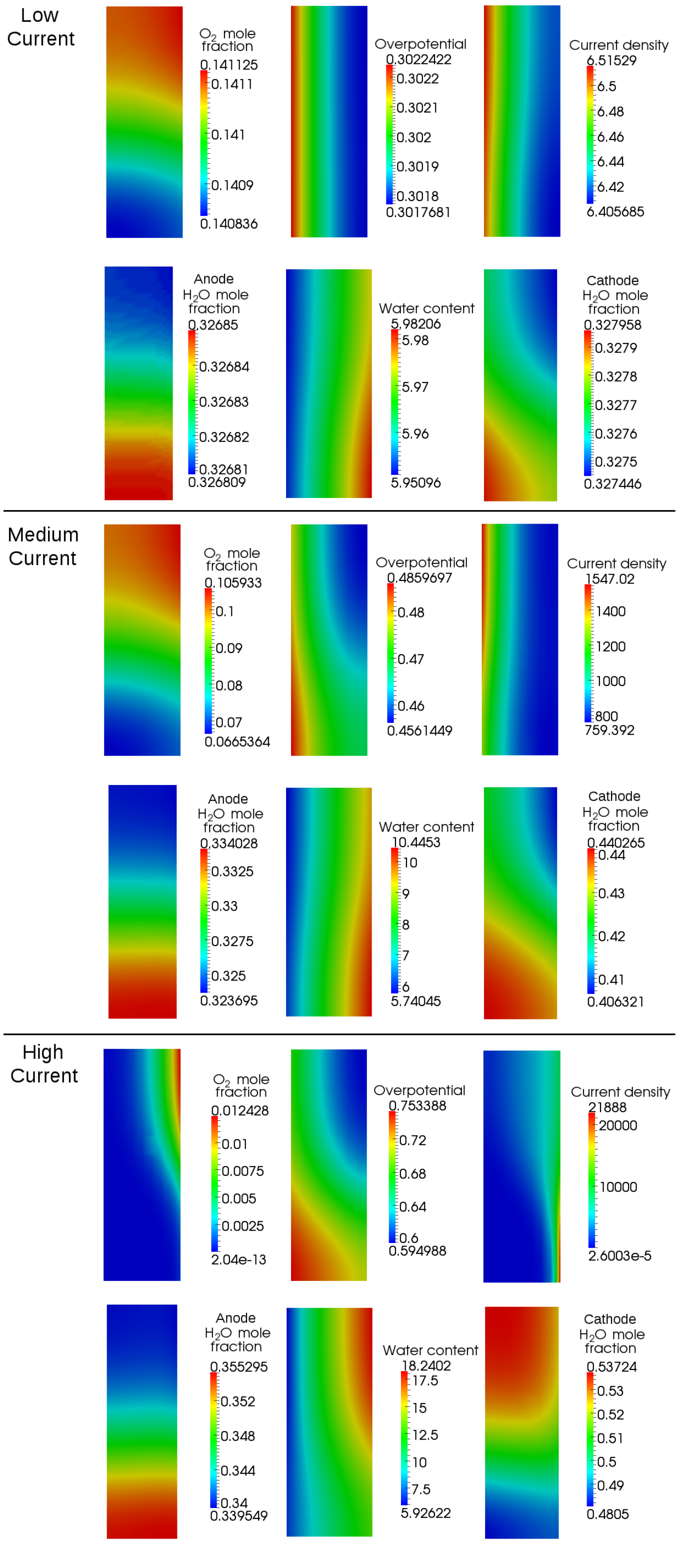

Figure 3.11: Profiles of the oxygen and water vapor molar fraction, overpotential, membrane water content and current density for the Tafel kinetic model. The top profiles are for a current density of $0.07A\ cm^{-2}$, the middle is at $1A\ cm^{-2}$ and the bottom is $3A\ cm^{-2}$

Of particular interest is the distribution of the current density across the CCL. At low overpotentials the current shows a very similar profile in both kinetic models, due to the very similar Tafel slopes. The overpotentials are very similar and show little variation across the layer. At the medium current density, there is some distinction between the profiles. The Tafel model shows a higher range of current densities in the layer and is less homogeneous than that of the double trap model. The overpotentials are greater for the double trap model, as the higher Tafel slope results in higher kinetic losses throughout the layer. The trend is clearer in the highest current density profiles. In both cases, the current distribution is produced entirely in a small region at the CCL/MPL interface, due to the lack of oxygen in the layer. Because of the higher effectiveness of the Tafel model, the upper limit of the current density range, $21888 Acm^{-3}$, is significantly higher than that of the double trap model. This allows the Tafel model to produce all the current in a smaller region, with most of the CCL producing no current. The double trap model can produce a maximum current density of $15315.8 Acm^{-3}$ so is forced to use more of the CCL. Higher overpotentials are needed, with the difference in the ranges at approximately $150 mV$.

The figures also show the mole fraction of water in both catalyst layers as well as membrane water content. The mole fraction of water in the anode CL does not change significantly during fuel cell operation, as water is not produced in the anode. Hydration is provided by the relative humidity of the hydrogen gas and by the diffusion of water across the membrane. Even at the highest current density, the anode hydration level is not significantly raised from the base level provided by the RH of the input gases. This lack of hydration can be explained by looking at the membrane water content, at medium and high currents there is a large gradient across the layer, with the anode side at a constant lambda value of 5. By contrast, at the cathode side there is an increasing water content with increasing current due to the production of water in the CCL. At medium currents, the CCL shows a maximum water vapor molar fraction of almost 44%. At a temperature of 80℃, the saturation pressure of water is 47311Pa. Once the partial pressure of the water vapor reaches this value, the vapor will condense and form liquid water. The presence of liquid water in the catalyst layer will impede the transport of oxygen to the reaction site and will incur major losses in performance. This effect is not accounted for in his work so the results presented in this section may not be valid after liquid water

Table 3.6: Operating conditions for the experimental data.

Case	**Pressure (atm)**	**Temperature (°C)**	**RH (%)**
1	1	80	50
2	1	80	70
3	1	95	50
4	1	95	70
5	2	80	50
6	2	80	70
7	2	95	50
8	2	95	70

begins to form. The total pressure in the cell is at 101325Pa, so the saturation pressure will be reached when mole fraction of water vapor is at 46%. At medium current ($1Acm^{-2}$), the mole fraction of almost 44% is close to the formation of liquid water, so results after $1Acm^{-2}$ should be discounted as significant losses are known to be unaccounted for.

3.3.2 Comparison with experimental data

3.3.2.1 Operating conditions

To further validate the model, the double-trap kinetic model, using parameters fitted in this work, was compared with the Tafel kinetic model against experimental data previously published by our research group in collaboration with the National Research Council Canada - Institute for Fuel Cell Innovation (NRC-IFCI) [69]. The data is a series of polarization curves over a number of operating conditions obtained using a $48.4cm^2$ MEA. The MEA catalyst layers were prepared with a platinum loading of $0.4mg/cm^2$ and a Nafion loading of 30% weight. These were coated onto an NRE-211 membrane to form a catalyst coated membrane (CCM). The resulting CCM was then inserted between two SIGRALET 24BC GDLs and the cell was assembled between straight flow-through channels. The MEA is very similar to that described by the base case in the previous section, with catalyst layers being slightly thicker at $1.1\mu m$. Further, the active area was measured experimentally and was found to be approximately $2 \times 10^5 \frac{cm^2 Pt}{cm^3 CL}$ by cyclic voltammetry. The single cell was tested using excess stoichiometries to reduce mass transport limitations. Pure hydrogen and air were fed to the cell at various relative humidities, temperatures and pressures. Eight cases tested were at the operating conditions shown in Table 3.6 and the results were found to be highly reproducible.

These cases were simulated using the two ORR kinetic models. The resulting polarization curves are given in Figures 3.12 and 3.13. At higher current densities, for all cases, the experimental data shows higher losses in the mass transport region that are not accounted for by this model. These losses are likely due to the simplifying assumptions made in the formulation of the MEA model, such as a macro-homogeneous catalyst or that there is an infinitesimally small layer of ionomer around the catalyst particles. The additional losses at higher current densities are not likely to be a result of the kinetic model so the discussion will be kept to the low current density region (up to approximately $0.5A/cm^2$) where kinetic losses are most pronounced.

At lower current densities, Figure 3.12 shows that the double-trap model better follows the trends in the experimental data. Both the Tafel and the double-trap model have similar profiles up to a cell potential of approximately $0.8V$, at which the change in Tafel slope for the double-trap model incurs greater losses across the ohmic region. These additional losses are also seen in the experimental data, leading to a close match with the double-trap model. There is a slight overprediction of the kinetic losses at approximately $0.5Acm^{-2}$, the upper Tafel slope may be slightly overpredicted at this temperature. The fit to the data is improved with the increase in relative humidity, this is most likely due to the proton conductivity being better modeled at higher RH. At 50% RH, there is a higher slope in the experimental data from $0.5A/cm^2$ to $1A/cm^2$, corresponding to the ohmic region, than at 70%. The numerical model does not show the same change in slope with changing RH. The figure also shows that the performance trend with increasing cell pressure is better captured with the double trap model. At both relative humidities, the double trap model very slightly overpredicts the performance at low current densities. This slight overprediction is also seen at the higher pressure.

The Tafel model, in contrast, slightly underpredicts the performance at 1atm and slightly overpredicts at 2atm for both relative humidities. These trends indicate that the oxygen reaction order is better modeled with the double-trap kinetic model. The reaction order for the Tafel model is at a constant value of one and is based on the zero overpotential reaction order found by Parthasarathy et al.. The double-trap model reaction order will vary with changing overpotential depending on the relative dominance of the intermediate steps. In the low current density region discussed here, the reaction order will vary from 0.3 to 0.5 as shown in Figure 2.15. At higher

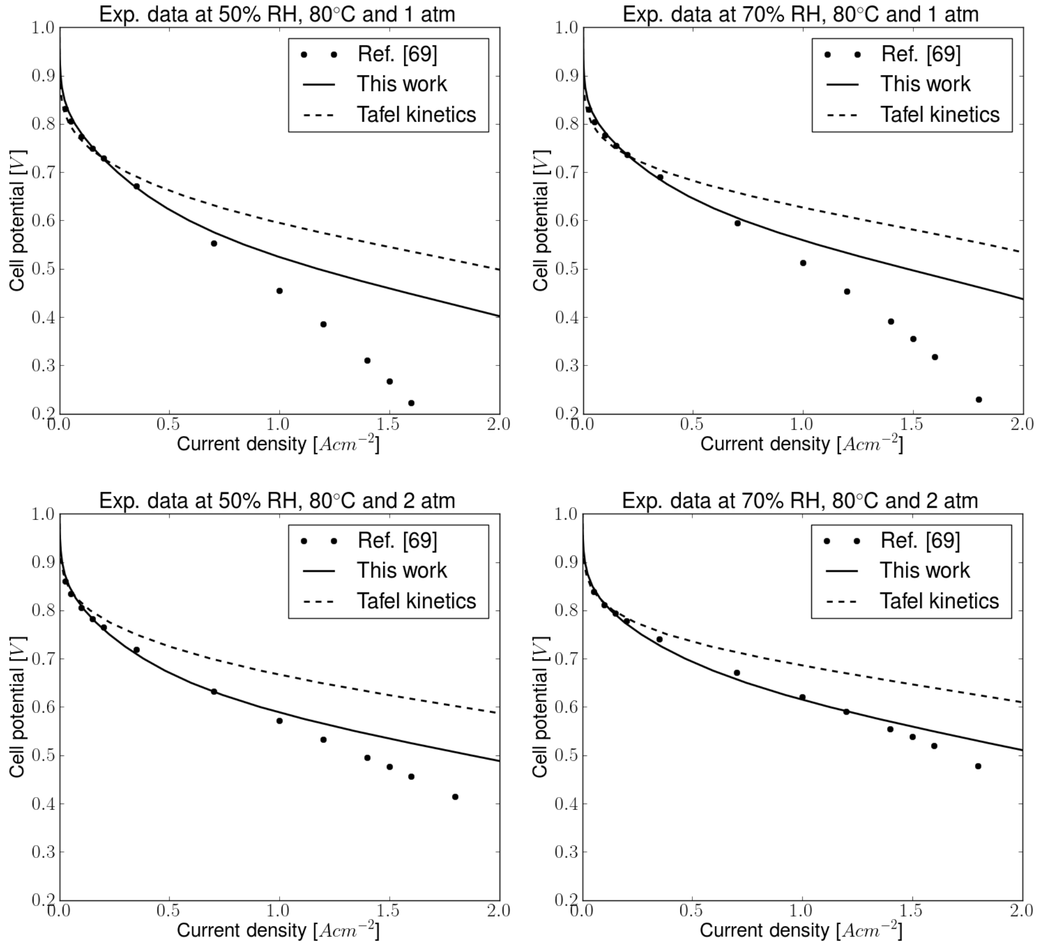
Exp. data at 50% RH, 80°C and 1 atm

Exp. data at 70% RH, 80°C and 1 atm

Exp. data at 50% RH, 80°C and 2 atm

Exp. data at 70% RH, 80°C and 2 atm

Figure 3.12: Polarization curves for cell pressure of 1atm and 2atm and relative humidities of 50% and 70%. The cell temperature is constant at 80°C.

pressures, the numerical data also better matches the experimental data over a greater range of current densities, as the higher cell pressure delays the onset of the condensation of liquid water.

Figure 3.13 shows the polarization curves at different cell pressures and relative humidities at a constant temperature of 95°C. The figure shows that over the four operating conditions there is a very slight, but consistent, increase in the difference between the experimental data and the double-trap model (i.e. the minor overprediction in performance is slightly greater at 95°C than it is at 80°C). This is not surprising, given that when fitting the double-trap model, there was no temperature dependence on the fitted experimental data. However, the double-trap model predicts cell performance remarkably well, especially when compared to the Tafel

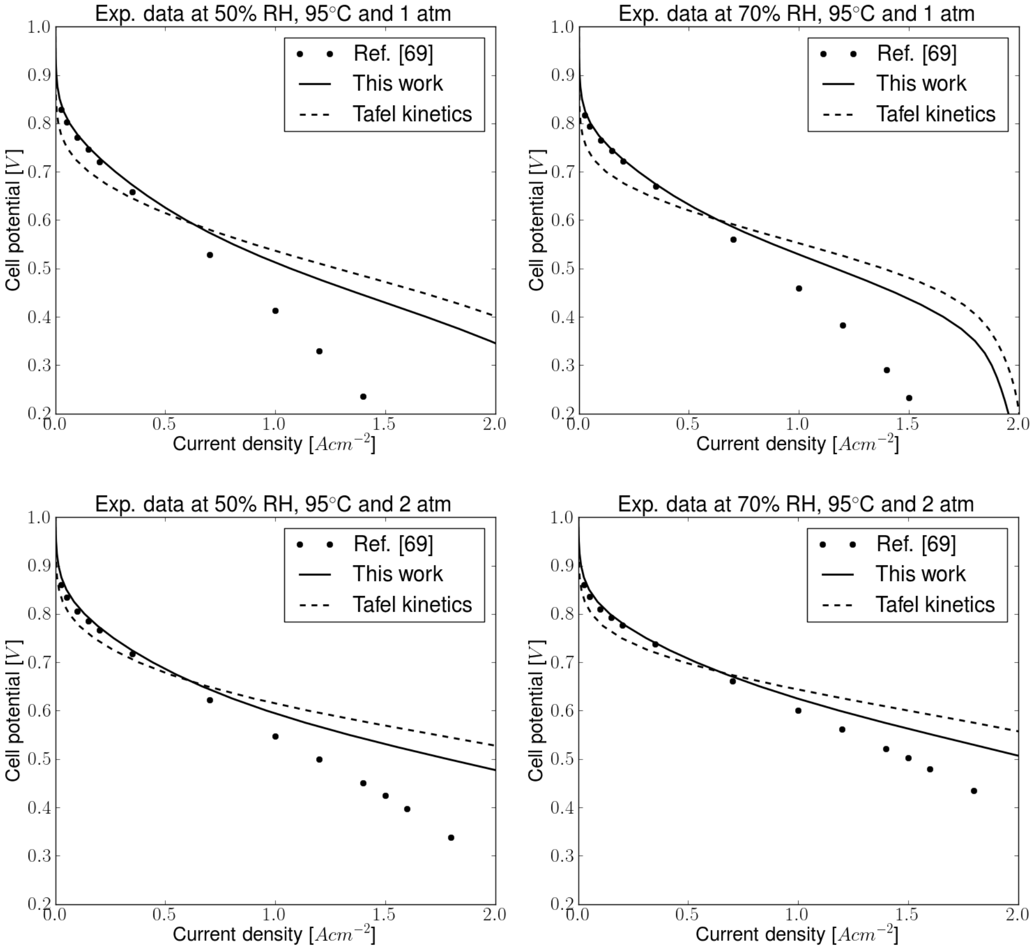

Figure 3.13: Polarization curves for cell pressure of 1atm and 2atm and relative humidities of 50% and 70%. The cell pressure is constant at 95°C.

model. At 80°C, the Tafel model is in reasonable agreement with the experimental data at low overpotentials. However, at 95°C, the model significantly under predicts the data, indicating that it cannot capture the temperature dependence of the ORR. The close agreement of the double-trap model to the experimental data at low current densities further validate the accuracy of the model, here under realistic fuel cell operation where many other physical phenomena are also occurring. The closeness of the match is remarkable considering that the experimental data is unrelated to the data that the kinetic model was fit to, and that the accuracy is maintained over a large number of operating conditions.

The accuracy of the model in the high current density region could be improved by taking into account that the micro-structure of the catalyst layer may increase the losses in the ohmic/mass transport region and therefore lead to better agreement of the experimental data with the MEA model. An example of modeling the agglomerate structure of the catalyst layer is given by Dobson [69], who assumed that the agglomerates take a spherical form and are wrapped in a thin film of ionomer. The structure of the agglomerates is difficult to characterize, so Dobson attempted to use parameter estimation to find the agglomerate radius and porosity, as well as the active area of the catalyst layer. The data used is the same as is presented in this work. In general, the fitted parameters were able to capture the greater losses in the ohmic region, however, this was achieved by fitting the agglomerate radius to a value of 250nm, which was the upper bound of the optimization formulation. Agglomerates of these sizes are not commonly found in microscopy studies of the catalyst layer structure. It was thought that the optimizer was trying to capture the experimental trends by reducing the pore volume fraction and therefore increase the mass transport losses. It was also found that while the ohmic region was well captured, the kinetic region was consistently overpredicted. The inclusion of the double-trap model into this agglomerate model would better capture the kinetic region and add additional losses throughout the ohmic region due to the doubling of the Tafel slope. The additional losses would likely allow the optimizer to set the agglomerate radius to a smaller value to capture the high ohmic region losses and therefore return an agglomerate radius more consistent with those seen the imaging of the catalyst layer. The implementation of the double-trap model into the agglomerate model is a very promising area for further research.

3.3.2.2 Platinum loading

Figure 3.9 showed the effectiveness of the platinum catalyst as predicted by the two kinetic models. The double-trap model shows lower effectiveness in the high current density region, so at the same ovepotential, the platinum cannot produce the same current as predicted by the kinetic model. To further investigate this effect, the ultra-thin CLs fabricated by Saha et al. [88] were simulated using the full MEA model with the two kinetic models and the model predictions were compared to their reported experimental data. The experimental data is presented as polarization curves found using catalyst layers of varying areal platinum loading. The areal platinum loading, in units of milligrams per centimeter squared of catalyst layer, describes how much of the platinum catalyst is present in the layer. The loading can be varied by reducing the thickness of the layer, as the volumetric platinum loading (i.e. milligrams per centimeter cubed of catalyst layer) is kept constant. Saha et al. investigated low platinum loadings in catalyst layer by preparing catalyst layers that were two to ten times smaller than those presented in the base case.

The polarization curves were obtained at 60°C and an anode and cathode pressure of 1.35atm, using a single $25cm^2$ cell with an MEA with varying cathode catalyst layers. Excess stoichiometries were used to at the anode and cathode to reduce mass transport losses. Using a constant Nafion loading, platinum/carbon ratio and near constant volumetric platinum loadings, the areal platinum loading is varied by varying the thickness of the layer. The catalyst is fabricated using a piezoelectric printer, where successive layers of $0.5\mu m$ are deposited onto a membrane. CCLs were made using 2, 5, 7 and 10 layers, corresponding to thicknesses of 1, 2.5, 3.5 and $5\mu m$ respectively. The loading for each layer is given as 0.02, 0.06, 0.08, $0.12 mg_{Pt}/cm^2$. respectively. The obtained experimental polarization curves are compared to the MEA model using double-trap kinetics in Figure 3.14(a) and using Tafel kinetics in Figure 3.14(b).

Neither model shows a good direct fit to the experimental data. This may be in part due to the fuel cell fixture used which does not guarantee uniform temperature and pressure. In addition to the ohmic region losses not accounted for using the MEA model, as were discussed in the previous section, the MEA model does not accurately characterize the homogeneous structure of the catalyst layer at the thicknesses used in the experimental data. In particular, the porosity of the layer as computed by the expressions from Wang et al. [77], was found to be at approximately 70%. This is significantly higher than the value of approximately 45% found in-house experimentally for a similar layer using intrusion porosimetry. However, the experimental data shows a wide spread between individual curves, showing significant variation in the performance of the different catalyst layers. This trend is not captured by the Tafel model, which shows little variation between the layers. Due to the reduced effectiveness of the double-trap kinetic model, as is shown in Figure 3.9, a much greater spread in the individual curves is predicted in comparison to the Tafel kinetic model.

Figure 3.15, shows the low current density region of Figure 3.14(a), where losses should be mainly due to the ORR kinetics. The figure shows closer agreement between the spread of the two data sets. Using the experimental data points close

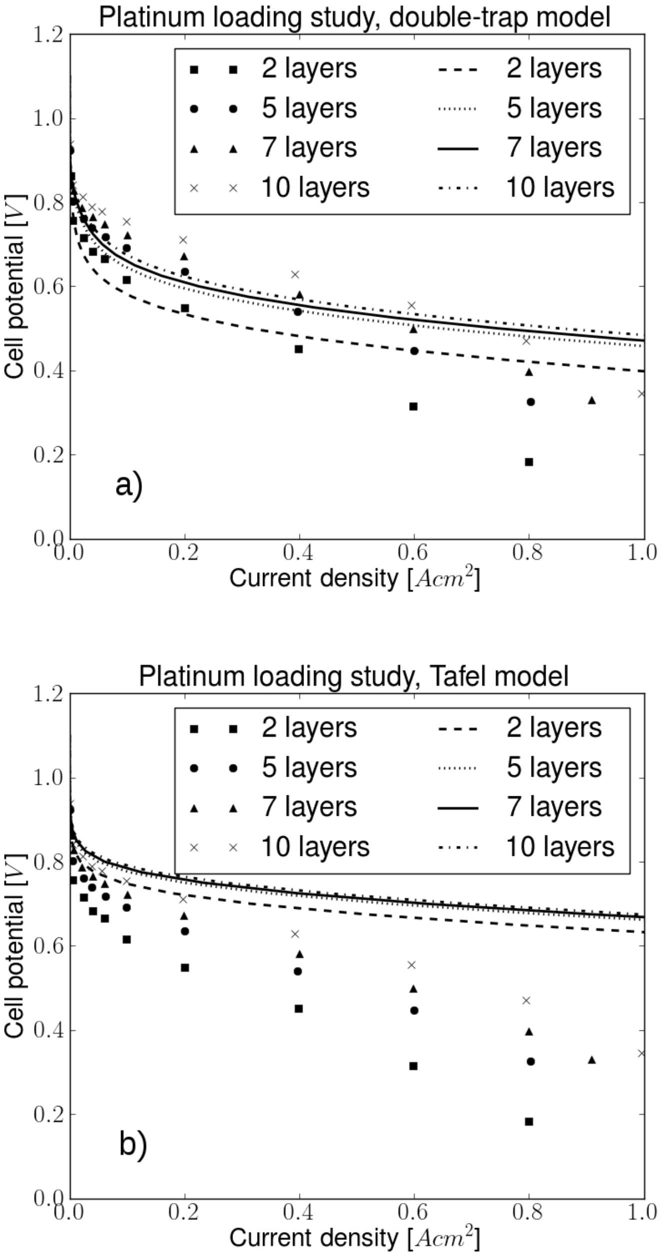

Figure 3.14: Comparison between experimental and simulated polarization curves for CCLs of varying areal platinum loadings. The points are the experimental data, while the lines represent the simulated data. The data was simulated using a) double-trap kinetics and b) Tafel kinetics.

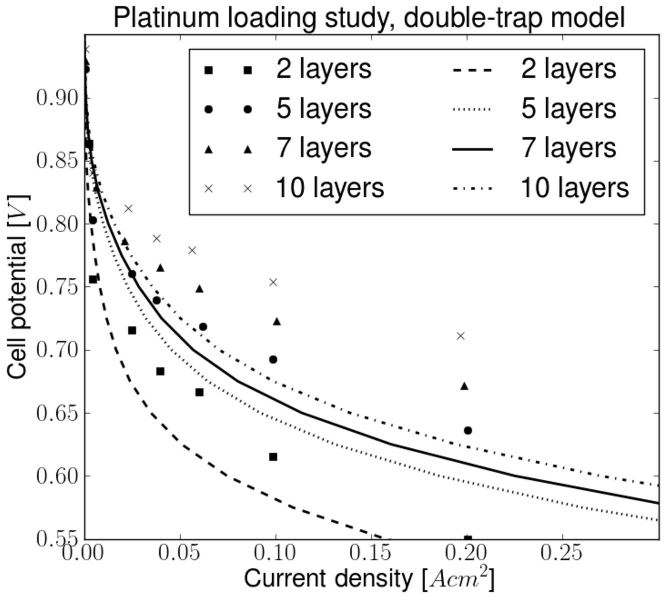

Figure 3.15: Kinetic region of Figure 3.14(a). The points are the experimental data, while the lines represent the simulated data using double-trap kinetics.

to current densities of $0.02A/cm^2$ and $0.06A/cm^2$, the difference between the 2 and 10 layer curves is a potential of 0.1V for both experimental and simulated data. The Tafel model predicts a difference of only 0.05V, for both points, so there is little difference in performance with changing loading. At the adjacent data points corresponding to a current density of $0.1A/cm^2$, the potential different is 0.14V compared to 0.1V for the double-trap model. Again, the Tafel model difference is at 0.05V. It is likely that other effects, such as ohmic losses, are impacting on the results at the higher current density so it is difficult to determine the agreement between the data sets. However, it is clear that the double-trap model better captures the loss in performance shown in the experimental data for varying areal platinum loadings when compared to the Tafel model.

The effect of reducing the layer thickness can be investigated further by plotting the profiles of the oxygen molar fraction, overpotential and current density. These plots are presented in Figures 3.16(a) and 3.16(b) for the ten layer CCL and Figures 3.17(a) and 3.17(b) for the two layer CCL. The profiles are shown at low, medium and high overpotentials, corresponding to the same current densities of $0.02A/cm^2$, $1A/cm^2$ and $3.85A/cm^2$, for both kinetic models in the kinetic, ohmic and mass transport limited regions respectively.

In Figures 3.16(a) and 3.16(b), both kinetic models show similar profiles at low current, with the double-trap model showing slightly higher overpotentials due to the higher Tafel slope. There is little variation in the profiles across the layer. For the medium current case, there is much greater variation across the layer. The oxygen profiles are the same for both, as the current produced is the same in both layers. The difference between the maximum and minimum overpotential is also the same. However, the actual values for the overpotentials are significantly higher for the double-trap model producing a major drop in performance compared to the Tafel model. At the highest current, both cases are in the mass transport limited region, as is clear from the shift in the current density to the right side of the layer (the CCL-MPL interface).

The current density profile shows major variations however. Due to the higher effectiveness of the Tafel model, all the current can be produced in a very thin region at the CCL-MPL interface, negating the need for much of catalyst layer. By contrast, the double trap model still shows some distribution across the layer. At the top of the layer, almost half of the layer is producing appreciable current, while approximately one fifth of the layer is producing current at the bottom of the layer. If this layer was reduced by over a half, then there would be a drop in the performance. In contrast, the Tafel model could lose over 90% of the layer without a noticeable decrease in performance. Note that in this case, two-phase flow would occur in the cell since the partial pressure of the water vapor is greater than the saturation pressure. However, this is neglected in the model.

The effect of lower Pt activity in the double trap model, compared to the Tafel model, can be seen in Figures 3.17(a) and 3.17(b). In this case, the catalyst layers are 80% thinner than used in Figures 3.16(a) and 3.16(b), i.e. $1\mu m$ and $5\mu m$. Due to the low effectiveness, the double-trap model predicts that almost all of the layer is used in the high current case. The model is only just about to produce the same current as the Tafel model, as evidenced in Figure 3.18, where the polarization curves show that the mass transport region is significantly smaller for the double-trap model. Any further reduction in the thickness and it will not be able to match the current density produced by the Tafel model. For the Tafel model, the current is again shifted almost towards the CCL-MPL interface, allowing further reduction in the thickness of the layer with a relatively small reduction in the produced current. This difference in the effectiveness as predicted by the two models accounts for the major loss in performance in Figure 3.14(a) for the double trap model with

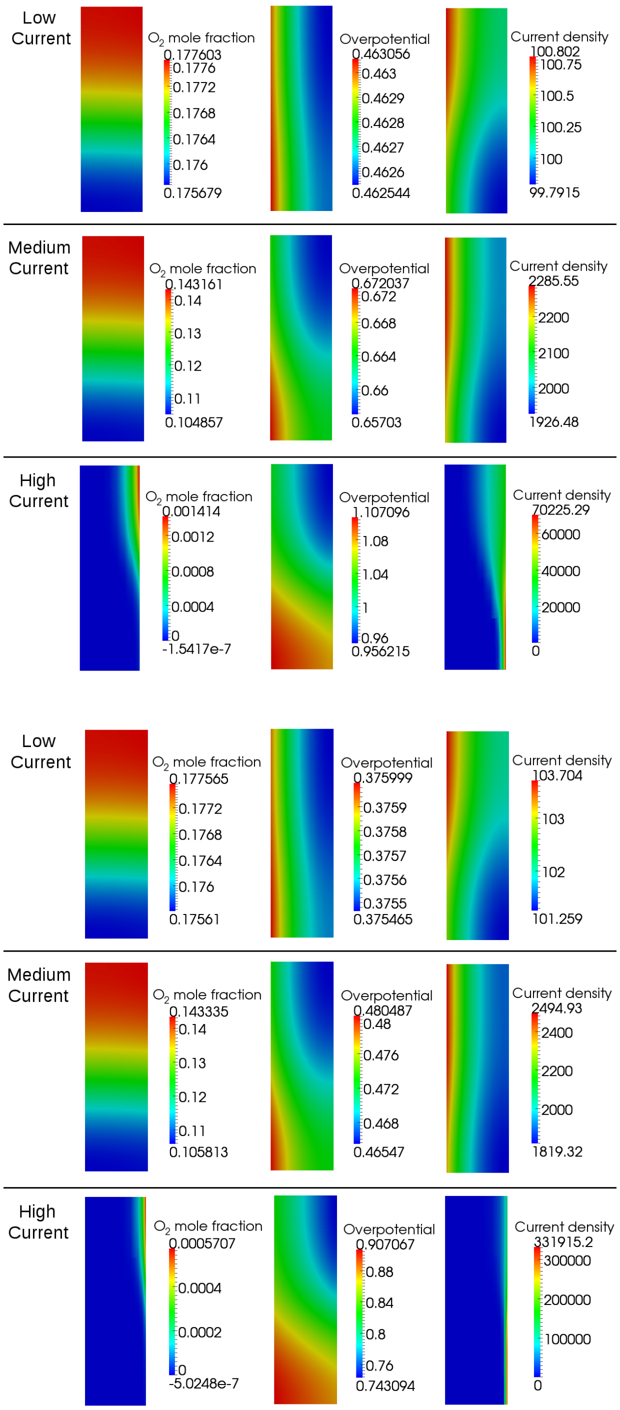

Figure 3.16: Comparison between solution profiles in the ten layer CCL as computed by a) double-trap kinetics (top) and b) Tafel kinetics. Profiles are plotted for current densities of 0.02 Acm^{-2}, 1.5Acm^{-2} and 3.85Acm^{-2} (bottom).

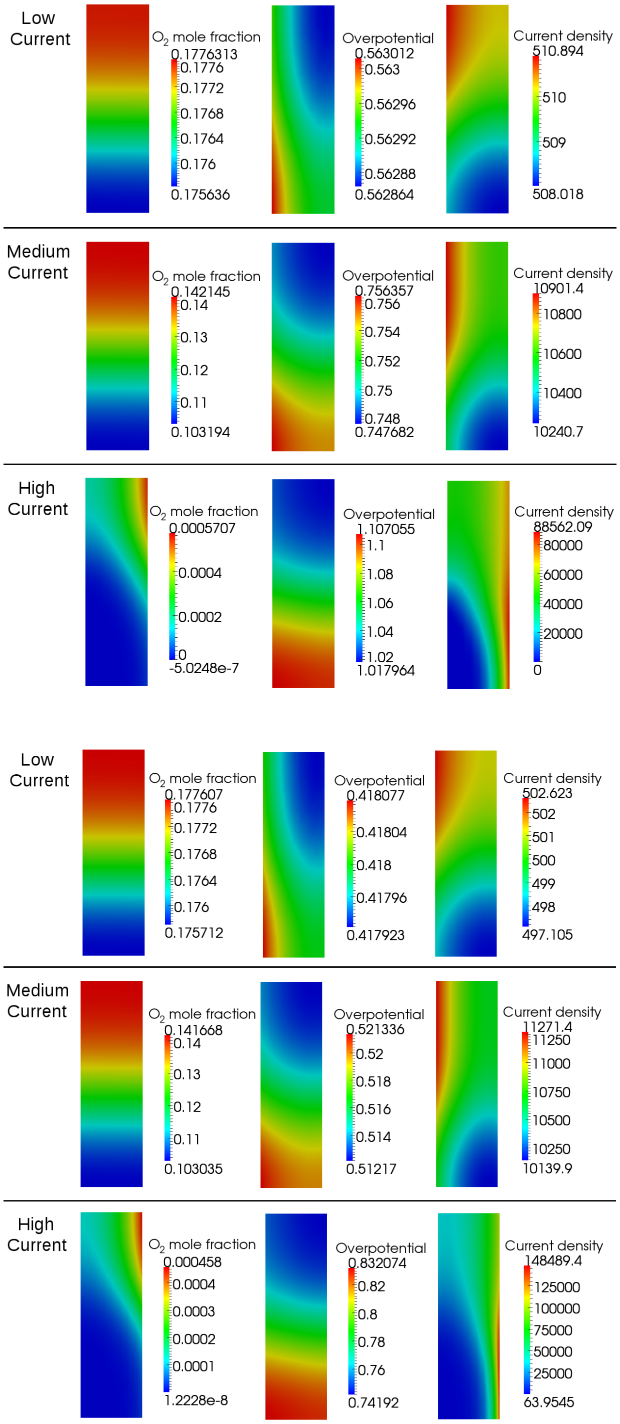

Figure 3.17: Comparison between solution profiles in the two layer CCL as computed by a) double-trap kinetics (top) and b) Tafel kinetics (bottom). Profiles are plotted for current densities of 0.02 Acm^{-2}, 1.5Acm^{-2} and 3.85Acm^{-2}.

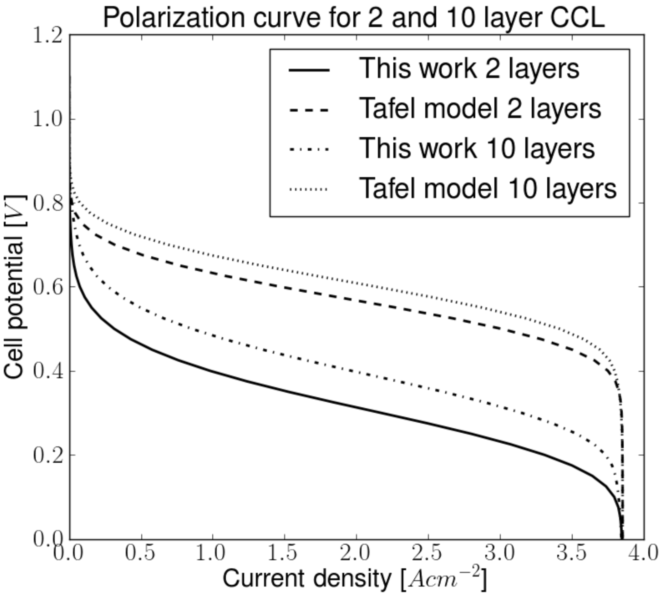

Figure 3.18: Full polarization curve for the two layer and ten layer CCL, as simulated by the double trap kinetic model from this work and the Tafel kinetic model.

the layer reduction, as compared to the minor drop in performance for the Tafel model as shown in Figure 3.14(b). A major drop in performance is predicted by the experimental data from Saha et al. [88], further validating the double-trap kinetic model.

Chapter 4

Conclusions and Future Work

4.1 Conclusions

This work was primarily focused on the investigation of one of the two half-cell reactions that occurs in a PEM fuel cell. In particular, the kinetics of the oxygen reduction reaction on a platinum catalyst was analyzed using an advanced kinetic model first proposed by Wang et al [48].

The literature review shows that the two Tafel slopes have been experimentally observed for several decades. Early experiments using relatively simple liquid electrolyte cells succeeded in determining the values of the slopes to be 60mV/dec in the low current density region and 120mV/dec in the high current density region. These values were further investigated and validated by later experiments using ring disk electrodes and solid-state micro-electrodes leading to general acceptance of the values of the Tafel slopes. It was also determined that the low Tafel slope occurs on a reaction surface that is covered by indeterminable absorbed intermediate species. At higher currents, these species are cleaned from the surface leading to the higher Tafel slope of 120mV/dec. The literature study also revealed that fuel cell modelers rarely account for the complexity of the ORR when performing high-fidelity simulations. It is commonly assumed that the change in Tafel slope was not significant due to losses stemming from proton transport through the membrane, oxygen depletion in the catalyst layer and the formation of liquid water. Hence, the ORR is commonly modeled using simple Butler-Volmer kinetics that cannot account for the change in Tafel slope. Kinetic parameters such as the apparent transfer coefficient and oxygen reaction order were taken from experimental data and generally characterized the low Tafel slope region only. This approach fails to account for the increased kinetic losses due to the doubling of the Tafel slope.

An advanced kinetic model was presented by Wang et al. [48], which assumed that the ORR could be broken into four intermediate reactions with two absorbed intermediate species, PtO and $PtOH$, resulting in two potential pathways. This model could capture the change in Tafel slope and predicted a high coverage of the intermediates at low current densities. However, it failed to predict very low coverage at high current densities. The model was based on determining the energy barriers of the intermediate reactions and how they changed with changing overpotential. The unknown parameters in the model were the height of the energy barriers at zero overpotential, which were found by fitting to experimental data. The accuracy of the model was investigated by comparison with kinetic data presented by Parthasarathy et al. [31, 32]. It was found that the model underestimated the Tafel slope at low current densities leading to an over-prediction in the overall kinetic performance. It was also found that the model did not correctly capture the dependence on oxygen partial pressure, as evidenced by the low oxygen reaction order.

In order to improve the accuracy of the model, the proposed kinetic model by Wang et al. [48] was re-formulated by including oxygen depletion effects and the backward reactions. The updated model was then fit to the kinetic data from Parthasarathy et al. [20], in order to find the unknown parameters, namely the height of the energy barriers and the absorption energy of the intermediates at low ovepotentials. The updated model was implemented into an in-house fuel cell simulation code (the FCST code) [68] that includes an interface to an open-source optimization library. Using a local, interior-point, gradient based optimization method (OPT++, [70]), the kinetic parameters were determined using multiple starting points to ensure that the global minimum was found. Using the new estimated parameters, the model was again compared to the kinetic data from Parthasarathy et al. A closer fit to the Tafel slopes was found, in particular in the low current density region. The coverage of the intermediate species was found to show remarkable agreement to experimental data, and given the general nature of the optimization formulation, this agreement adds to the validity of the improved kinetic model. The model predicts that at high current densities, the ORR is absorption limited, with the reductive absorption of oxygen being the rate determining step. At low current densities, it is shown that the assumption of a rate determining step is incorrect, as the two pathways are equally dominant.

The improved model was then implemented into a high-fidelity, two dimensional, macro-homogeneous PEM fuel cell model that accounted for the transport of the reactants as well as water vapor. Proton and electron transport as well as the uptake of water in the membrane were also accounted for. The advanced kinetic model was compared to the commonly used Tafel equation. By comparing to experimental data at varying relative humidities, cell temperatures and pressures, it was found that the double-trap model could closely match the low current density region over all operating conditions. The Tafel equation could not capture the dependence on the changing operating conditions and significantly overpredicted the cell performance. At higher current densities, both models were found to overpredict the cell performance which was attributed to simplifications in the formulation of the mass transport losses in the two dimensional fuel cell model. In particular, the assumption of a macro-homogeneous catalyst layer and neglecting liquid water accumulation are likely to hide significant mass transport losses. The implementation of the double-trap model into a more advanced fuel cell model that accounts for the agglomerate structure of the catalyst layer and two-phase flow will likely be able to capture both current density regions. In addition to investigating varying operating conditions, the performance of the MEA model with varying areal platinum loadings was investigated. Experimental data from Saha et al [88] show a major drop in performance incurred by reducing the platinum loading. Due to the lower predicted effectiveness of the double-trap model, the proposed model was able to reproduce the trends in the experimental data. By contrast, the Tafel equation showed little drop in performance as a result of reducing the loading, adding further validation to the double-trap kinetic model.

The double-trap model, using kinetic parameters fitted in this work, was found to be able to accurately capture the kinetics of the ORR, as evidenced in the close agreement in the predicted Tafel slope. The development of this model has resulted in the development of a general framework that can be used to investigate kinetic models of greater complexity that account for more intermediate steps and reactions than assumed in this work. The significance of the change in Tafel slope was demonstrated with the comparison of the kinetic model to experimental data which showed very close agreement in the region where kinetic losses dominate. The development of the updated kinetic model has added further understanding to the nature of the ORR and allows for greater predictive capability in the numerical study of PEM fuel cells

4.2 Future Work

The updated kinetic model presented in this work makes a number of assumptions regarding the nature of the ORR. It was assumed that the reaction is comprised of only four intermediate steps with two intermediate species produced. Many other species could be formed during the ORR, such as PtO_2 or PtO_2H. Further, it is thought that the formation of hydrogen peroxide at high overpotentials leads to the degradation of the membrane. The approach this work to estimate kinetic parameters, could be applied to more complicated models. For example, the fractional stoichiometric number used in the two absorption reactions in the current model could be removed by accounting for the absorption of molecular oxygen. Another example is the highly advanced ORR mechanism proposed by Ruvinskiy et al. [65, 66] that includes the two-electron transfer series pathway and therefore the formation of hydrogen peroxide, which could also be investigated using the approach used in this thesis. A framework has been developed whereby any complex reaction that can be broken into a series of individual single electron transfer reactions can be analyzed to find the resulting current density and coverage of intermediate species. The framework includes an optimization package allowing for the determination of unknown energy barriers and absorption energies. Increasing the complexity of the overall reaction adds to the difficulty in fitting the kinetic parameters, which may require more sophisticated optimization methods, such as genetic algorithms, which are provided by the optimization package used in this work. This framework is another possible tool that can be used in the investigation of the oxygen reduction reaction, and is a highly promising area for further study.

An additional area for future work lies in the further development of the in-house fuel cell simulation software that was used in this work. The predictive capability of the software can be improved by continually adding to the physical phenomena that are thought to occur during fuel cell operation. The additional complexity added by this work was a more advanced kinetic model that accounts for the change in the Tafel slope of the ORR. This was shown to improve the accuracy of the model in the low current density region and account for the losses incurred by reducing the areal platinum loading. The FCST code can also account for the micro-structure of the cathode catalyst layer which was shown in previous work [69] to better match the performance in the high current density region. In particular, additional losses due to the transport of oxygen and proton through the agglomerate structure of the layer were better accounted for. The combination of both of these models should result in a highly accurate model that may capture the entire current density region, for varying operating conditions and CCL compositions.

Other improvements to the mathematical fuel cell model include accounting for the formation of liquid water in the cell, which can impede the transport of oxygen to the reaction site, or accounting for the heat produced during the reaction, resulting in a non-isothermal model. This improved model will provide greater predictive power allowing for fuel cell design and optimization, which again can be provided by the included open-source optimization package. An example of the potential optimization of the catalyst layers is the design of functionally graded layers that minimize the platinum used in the layer. By predicting areas within the layer of high current density, the platinum loading can be reduced in other areas resulting in greater overall utilization of the platinum. This can help lower the cost of fuel cell production allowing for the more widespread application of the technology in the future.

Bibliography

[1] Scientific American, Looking at hydrogen to replace gasoline in our cars, Taken on August 11, 2012, 4.30 PM (2008).
URL `http://www.scientificamerican.com/article.cfm?id=can-hydrogen-replace-gas`

[2] D. Cheddie, N. Munroe, Review and comparison of approaches to proton exchange membrane fuel cell modeling, Journal of Power Sources 147 (1-2) (2005) 72–84.

[3] N. Djilali, Computational modelling of polymer electrolyte membrane (pem) fuel cells: Challenges and opportunities, Energy 32 (4) (2007) 269 – 280.

[4] J. Wang, J. Zhang, R. R. Adzic, Double-trap kinetic equation for the oxygen reduction reaction on pt(111) in acidic media, J. Phys. Chem. A 111 (2007) 12702–12710.

[5] A. Gewirth, M. Thorum, Electroreduction of dioxygen for fuel-cell applications: Material and challenges, Inorganic Chemistry 49 (2010) 3557–3566.

[6] R. O'Hayre, S. Cha, W. Colella, F. Prinz, Fuel Cell Fundamentals, 2nd Edition, John Wiley & sons, 2010.

[7] Compliled by A. D. McNaught, A. Wilkinson, Compendium of chemical terminology, 2nd Edition, Blackwell Scientific Publications, Oxford, 1997.

[8] A. Bard, L. Faulkner, Electrochemical Methods: Fundamentals and Applications, 2nd Edition, John Wiley & Sons, 2001.

[9] A. Appleby, Electrocatalysis of aqueous dioxygen reduction, Journal of Electroanalytical Chemistry 357 (12) (1993) 117 – 179.

[10] J. O'M. Bockris, A primer on electrocatalysis, Journal of the Serbian Chemical Society 70 (3) (2005) 475 – 487.

[11] N. P. Subramanian, T. A. Greszler, J. Zhang, W. Gu, R. Makharia, Pt-oxide coverage-dependent oxygen reduction reaction (ORR) kinetics, Journal of The Electrochemical Society 159 (5) (2012) B531–B540.

[12] J. O'M. Bockris, L. F. Oldfield, The oxidation-reduction reactions of hydrogen peroxide at inert metal electrodes and mercury cathodes, Trans. Faraday Soc. 51 (1955) 249–259.

[13] J. O'M. Bockris, A. K. M. Shamshul Huq, The mechanism of the electrolytic evolution of oxygen on platinum, Proceedings of the Royal Society of London. Series A. Mathematical and Physical Sciences 237 (1209) (1956) 277–296.

[14] A. Damjanovic, A. Dey, J. O'M. Bockris, Kinetics of oxygen evolution and dissolution on platinum electrodes, Electrochimica Acta 11 (7) (1966) 791 – 814.

[15] A. Damjanovic, V. Brusic, Electrode kinetics of oxygen reduction on oxide-free platinum electrodes, Electrochimica Acta 12 (6) (1967) 615 – 628.

[16] A. Damjanovic, M. Genshaw, Dependence of the kinetics of O_2 dissolution at pt on the conditions for adsorption of reaction intermediates, Electrochimica Acta 15 (7) (1970) 1281 – 1283.

[17] M. Paucirova, D. Drazic, A. Damjanovic, The effect of surface coverage by adsorbed oxygen on the kinetics of oxygen reduction at oxide free platinum, Electrochimica Acta 18 (12) (1973) 945 – 951.

[18] D. Sepa, M. Vojnovic, A. Damjanovic, Reaction intermediates as a controlling factor in the kinetics and mechanism of oxygen reduction at platinum electrodes, Electrochimica Acta 26 (6) (1981) 781 – 793.

[19] A. Damjanovic, On the kinetics and mechanism of oxygen reduction at oxide film-covered pt electrodes in acid solutions, Journal of The Electrochemical Society 138 (8) (1991) 2315–2320.

[20] A. Parthasarathy, C. R. Martin, S. Srinivasan, Investigations of the O_2 reduction reaction at the platinum/nafion® interface using a solid-state electrochemical cell, Journal of The Electrochemical Society 138 (4) (1991) 916–921.

[21] V. Basura, P. Beattie, S. Holdcroft, Solid-state electrochemical oxygen reduction at pt—nafion® 117 and pt—bam3g™ 407 interfaces, Journal of Electroanalytical Chemistry 458 (12) (1998) 1 – 5.

[22] P. D. Beattie, V. I. Basura, S. Holdcroft, Temperature and pressure dependence of O_2 reduction at pt—nafion® 117 and pt—bam® 407 interfaces, Journal of Electroanalytical Chemistry 468 (2) (1999) 180 – 192.

[23] U. Paulus, T. Schmidt, H. Gasteiger, R. Behm, Oxygen reduction on a high-surface area pt/vulcan carbon catalyst: a thin-film rotating ring-disk electrode study, Journal of Electroanalytical Chemistry 495 (2) (2001) 134 – 145.

[24] N. Wakabayashi, M. Takeichi, M. Itagaki, H. Uchida, M. Watanabe, Temperature-dependence of oxygen reduction activity at a platinum electrode in an acidic electrolyte solution investigated with a channel flow double electrode, Journal of Electroanalytical Chemistry 574 (2) (2005) 339 – 346.

[25] A. Dhanda, R. O'Hayre, H. Pitsch, ORR adsorbate dynamics on pt single crystal pem fuel cells, ECS Transactions 16 (2) (2008) 1131–1142.

[26] H. Wroblowa, Y. Pan, G. Razumney, Electroreduction of oxygen: A new mechanistic approach, Journal Electroanalytical Chemistry 69 (1976) 195–201.

[27] E. Yeager, Electrocatalysts for O_2 reduction, Electrochimica Acta 29 (1984) 1527–1537.

[28] S. Gottesfeld, Some observations on the oxygen reduction reaction (ORR) at platinum catalysts based on post year 2000 reports, ECS Transactions 6 (25) (2008) 51–67.

[29] J. Zhang, PEM Fuel Cell Electrocatalysts and Catalyst Layers Fundamentals and Applications, 1st Edition, Springer, 2008.

[30] S. Walch, A. Dhanda, M. Aryanpour, H. Pitsch, Mechanism of Molecular Oxygen Reduction at the Cathode of a PEM Fuel Cell: Non-Electrochemical Reactions on Catalytic Pt Particles, The Journal of Physical Chemistry C 112 (22) (2008) 8464–8475.

[31] A. Parthasarathy, S. Srinivasan, A. J. Appleby, C. R. Martin, Pressure dependence of the oxygen reduction reaction at the platinum microelectrode/nafion interface: Electrode kinetics and mass transport, Journal of the Electrochemical Society 139 (9) (1992) 2530–2537.

[32] A. Parthasarathy, S. Srinivasan, A. J. Appleby, C. R. Martin, Temperature dependence of the electrode kinetics of oxygen reduction at the platinum/nafion interface—a microelectrode investigation, Journal of the Electrochemical Society 139 (10) (1992) 2856–2862.

[33] A. Mani, S. Holdcroft, Highly temperature dependent mass-transport parameters for ORR in nafion® 211, Journal of Electroanalytical Chemistry 651 (2) (2011) 211 – 215.

[34] L. Zhang, C. Ma, S. Mukerjee, Oxygen reduction and transport characteristics at a platinum and alternative proton conducting membrane interface, Journal of Electroanalytical Chemistry 568 (0) (2004) 273 – 291.

[35] D. S. Strmcnik, P. Rebec, M. Gaberscek, D. Tripkovic, V. Stamenkovic, C. Lucas, N. M. Marković, Relationship between the Surface Coverage of Spectator Species and the Rate of Electrocatalytic Reactions, The Journal of Physical Chemistry C 111 (50) (2007) 18672–18678.

[36] A. Panchenko, M. T. M. Koper, T. E. Shubina, S. J. Mitchell, E. Roduner, Ab initio calculations of intermediates of oxygen reduction on low-index platinum surfaces, Journal of The Electrochemical Society 151 (12) (2004) A2016–A2027.

[37] V. Tripković, E. Skúlason, S. Siahrostami, J. K. Nørskov, J. Rossmeisl, The oxygen reduction reaction mechanism on pt(111) from density functional theory calculations, Electrochimica Acta 55 (27) (2010) 7975 – 7981.

[38] A. Shah, K. Luo, T. Ralph, F. Walsh, Recent trends and developments in polymer electrolyte membrane fuel cell modelling, Electrochimica Acta 56 (11) (2011) 3731 – 3757.

[39] I. E. L. Stephens, A. S. Bondarenko, U. Gronbjerg, J. Rossmeisl, I. Chorkendorff, Understanding the electrocatalysis of oxygen reduction on platinum and its alloys, Energy Environ. Sci. 5 (2012) 67446762.

[40] Y. Liu, M. Mathias, J. Zhang, Measurement of platinum oxide coverage in a proton exchange membrane fuel cell, Electrochemical and Solid-State Letters 13 (1) (2010) B1–B3.

[41] J. A. Keith, G. Jerkiewicz, T. Jacob, Theoretical Investigations of the Oxygen Reduction Reaction on Pt(111), ChemPhysChem 11 (13) (2010) 2779–2794.

[42] H. Xu, R. Kunz, J. M. Fenton, Investigation of platinum oxidation in pem fuel cells at various relative humidities, Electrochemical and Solid-State Letters 10 (1) (2007) B1–B5.

[43] D. Sepa, M. Vojnovic, L. Vracar, A. Damjanovic, A confirmation of the O_2 reduction mechanism at pt electrodes from temperature studies, Electrochimica Acta 29 (8) (1984) 1169 – 1170.

[44] Y. Fang, Z. Liu, Electrochemical reactions at the electrode/solution interface: Theory and applications to water electrolysis and oxygen reduction, Science China Chemistry 53 (2010) 543–552.

[45] R. A. Sidik, A. B. Anderson, Density functional theory study of O_2 electroreduction when bonded to a pt dual site, Journal of Electroanalytical Chemistry 528 (12) (2002) 69 – 76.

[46] J. K. Nørskov, J. Rossmeisl, A. Logadottir, L. Lindqvist, J. R. Kitchin, T. Bligaard, H. Jónsson, Origin of the Overpotential for Oxygen Reduction at a Fuel-Cell Cathode, The Journal of Physical Chemistry B 108 (46) (2004) 17886–17892.

[47] N. Marković, H. Gasteiger, B. Grgur, P. Ross, Oxygen reduction reaction on pt(111): effects of bromide, Journal of Electroanalytical Chemistry 467 (12) (1999) 157 – 163.

[48] J. Wang, F. Uribe, T. E. Springer, J. Zhang, R. R. Adzica, Intrinsic kinetic equation for oxygen reduction reaction in acidic media: the double tafel slope and fuel cell applications, Faraday Discuss. 140 (2008) 347–362.

[49] R. Iczkowski, M. Cutlip, Voltage losses in fuel cell cathodes, Journal of The Electrochemical Society 127 (1980) 1433–1440.

[50] T. Springer, T. Zawodzinski, S. Gottesfeld, Polymer electrolyte fuel cell model, Journal of the Electrochemical Society 138 (8) (1991) 2334–2342.

[51] K. Broka, P. Ekdunge, Modelling the PEM fuel cell cathode, Journal of Applied Electrochemistry 27 (3) (1997) 281–289.

[52] M. Eikerling, A. Kornyshev, Modelling the performance of the cathode catalyst layer of polymer electrolyte fuel cells, Journal of Electroanalytical Chemistry 453 (1-2) (1998) 89–106.

[53] A. Kulikovsky, J. Divisek, A. Kornyshev, Modeling the cathode compartment of polymer electrolyte fuel cells: Dead and active reaction zones, Journal of the Electrochemical Society 146 (11) (1999) 3981–3991.

[54] V. Gurau, F. Barbir, H. Liub, An analytical solution of a half-cell model for PEM fuel cells, Journal of The Electrochemical Society 147 (7) 2468–2477.

[55] S. Um, C. . Wang, K. S. Chen, Computational fluid dynamics modeling of proton exchange membrane fuel cells, Journal of The Electrochemical Society 147 (12) (2000) 4485–4493.

[56] L. You, H. Liu, A parametric study of the cathode catalyst layer of PEM fuel cells using a pseudo-homogeneous model, International Journal of Hydrogen Energy 26 (9) (2001) 991–999.

[57] D. Song, Q. Wang, Z. Liu, T. Navessin, M. Eikerling, S. Holdcroft, Numerical optimization study of the catalyst layer of pem fuel cell cathode, Journal of Power Sources 126 (1-2) (2004) 104–111.

[58] W. Sun, B. A. Peppley, K. Karan, An improved two-dimensional agglomerate cathode model to study the influence of catalyst layer structural parameters, Electrochimica Acta 50 (16-17) (2005) 3347–3358.

[59] P. Berg, A. Novruzi, K. Promislow, Analysis of a cathode catalyst layer model for a polymer electrolyte fuel cell, Chemical Engineering Science 61 (2006) 4316–4331.

[60] M. Secanell, B. Carnes, A. Suleman, N. Djilali, Numerical optimization of proton exchange membrane fuel cell cathodes, Electrochimica Acta 52 (7) (2007) 2668–2682.

[61] P. Dobson, C. Lei, T. Navessin, M. Secanell, Characterization of the PEM fuel cell catalyst layer microstructure by nonlinear least-squares parameter estimation, Journal of the Electrochemical Society 159 (5) (2012) B514–B523.

[62] P. Gode, F. Jaouen, G. Lindbergh, A. Lundblad, G. Sundholm, Influence of the compositon on the structure and electrochemical characteristics of the pemfc cathode, Electochimica Acta 48 (2003) 4175–4187.

[63] K. C. Neyerlin, W. Gu, J. Jorne, H. A. Gasteiger, Determination of catalyst unique parameters for the oxygen reduction reaction in a PEMFC, Journal of the Electrochemical Society 154 (10) (2006) A1955–A1963.

[64] Y. Suzuki, S. Sugawara, N. Horibe, S. S. Kocha, K. Shinohara, Mea performance modeling for breakdown of catalyst layer polarization components, ECS Meeting Abstracts 802 (11) (2008) 919–919.

[65] P. S. Ruvinskiy, A. Bonnefont, C. Pham-Huu, E. R. Savinova, Using ordered carbon nanomaterials for shedding light on the mechanism of the cathodic oxygen reduction reaction, Langmuir 27 (14) (2011) 9018–9027.

[66] P. Ruvinskiy, A. Bonnefont, E. Savinova, 3d-ordered layers of vertically aligned carbon nanofilaments as a model approach to study electrocatalysis on nanomaterials, Electrochimica Acta (0) (2012) –.

[67] M. Eldred, et al., Dakota, a multilevel parallel object-oriented framework for design optimization, parameter estimation, uncertainty quantification, and sensitivity analysis. version 5.0 users manual., Tech. Rep. SAND2010-2183, Sandia National Laboratory (2010).

[68] M. Secanell, Computational modeling and optimization of proton exchange membrane fuel cells, Ph.D. thesis, University of Victoria (November 2007).

[69] P. Dobson, Investigation of the polymer electrolyte membrane fuel cell catalyst layer microstructure, Master's thesis, University of Alberta (September 2011).

[70] J. Meza, R. Oliva, P. Hough, P. Williams, OPT++: An object-oriented toolkit for nonlinear optimization, ACM Transactions on Mathematical Software 33 (2) (2007) 1–27.

[71] V. S. Murthi, R. C. Urian, S. Mukerjee, Oxygen reduction kinetics in low and medium temperature acid environment: correlation of water activation and surface properties in supported pt and pt alloy electrocatalysts, The Journal of Physical Chemistry B 108 (30) (2004) 11011–11023.

[72] J. X. Wang, T. E. Springer, R. R. Adzic, Dual-pathway kinetic equation for the hydrogen oxidation reaction on pt electrodes, Journal of the Electrochemical Society 153 (9) (2006) A1732–A1740.

[73] E-TEK, Specifications for c-1: Hp platinum on Vulcan XC-72, www.etek-inc.com.

[74] Y. Liu, M. W. Murphy, D. R. Baker, W. Gu, C. Ji, J. Jorne, H. A. Gasteiger, Proton conduction and oxygen reduction kinetics in pem fuel cell cathodes: Effects of ionomer-to-carbon ratio and relative humidity, Journal of The Electrochemical Society 156 (8) (2009) B970–B980.

[75] M. Secanell, K. Karan, A. Suleman, N. Djilali, Multi-variable optimization of PEMFC cathodes using an agglomerate model, Electrochimica Acta 52 (22) (2007) 6318–6337.

[76] S. Kamarajugadda, S. Mazumder, Generalized flooded agglomerate model for the cathode catalyst layer of a polymer electrolyte membrane fuel cell, Journal of Power Sources 208 (0) (2012) 328 – 339.

[77] Q. Wang, M. Eikerling, D. Song, Z. Liu, T. Navessin, Z. Xie, S. Holdcroft, Functionally graded cathode catalyst layers for polymer electrolyte fuel cells. I. theoretical modeling, Journal of the Electrochemical Society 151 (7) (2004) A950–A957.

[78] M. M. Tomadakis, S. V. Sotirchos, Ordinary and transition regime diffusion in random fiber structures, AIChE Journal 39 (3) (1993) 397–412.

[79] Z. Yu, R. N. Carter, Measurement of effective oxygen diffusivity in electrodes for proton exchange membrane fuel cells, Journal of Power Sources 195 (4) (2010) 1079 – 1084.

[80] H. Iden, A. Ohma, K. Shinohara, Analysis of proton transport in pseudo catalyst layers, Journal of The Electrochemical Society 156 (9) (2009) B1078–B1084.

[81] H. Iden, K. Sato, A. Ohma, K. Shinohara, Relationship among microstructure, ionomer property and proton transport in pseudo catalyst layers, Journal of The Electrochemical Society 158 (8) (2011) B987–B994.

[82] L. BekkTech, In-plane conductivity testing procedures & results, Accessed: August 10, 2010 (2007).
URL `http://www1.eere.energy.gov/hydrogenandfuelcells/pdfs/htmwg_bekktech.pdf`

[83] S. Motupally, A. J. Becker, john W. Weidner, Diffusion of water in Nafion 115 membranes, Journal of the Electrochemical Society 147 (9) (2000) 3171–3177.

[84] D. W. Kelly, J. P. de S. R. Gago, O. C. Zienkiewicz, I. Babuska, A posteriori error analysis and adaptive processes in the finite element method: Part i - error analysis, International Journal for Numerical Methods in Engineering 19 (11) (1983) 1593–1619.

[85] T. A. Davis, Algorithm 832: Umfpack, an unsymmetric-pattern multifrontal method, ACM Transactions on Mathematical Software 30 (2) (2004) 196–199.

[86] W. Bangerth, R. Hartmann, G. Kanschat, `deal.II` Differential Equations Analysis Library, Technical Reference.
URL `http://www.dealii.org`

[87] W. Bangerth, R. Hartmann, G. Kanschat, deal.II – a general purpose object oriented finite element library, ACM Trans. Math. Softw. 33 (4) (2007) 24/1–24/27.

[88] M. S. Saha, D. Malevich, E. Halliop, J. G. Pharoah, B. A. Peppley, K. Karan, Electrochemical activity and catalyst utilization of low pt and thickness controlled membrane electrode assemblies, Journal of The Electrochemical Society 158 (5) (2011) B562–B567.